Fakultät für
Mathematik, Informatik
und Naturwissenschaften

RWTH AACHEN UNIVERSITY

Scaffold-Free models for Tissue Engineering

Von der Fakultät für Mathematik, Informatik und Naturwissenschaften der RWTH Aachen University zur Erlangung des akademischen Grades eines Doktors der Naturwissenschaften genehmigte Dissertation

vorgelegt von

Rahul Rimal, M.Sc.

aus

Kathmandu, Nepal

Berichter: Universitätsprofessor Dr. rer. nat. Martin Möller

Universitätsprofessor Dr. rer. nat. Andreas Ludwig

Tag der mündlichen Prüfung: 20.03.2024

To my family

Declaration of Authorship

I, Rahul Rimal

declare that this thesis and the work presented in it are my own and has been generated by me as the result of my own original research.

Hiermit erkläre ich an Eides statt / I do solemnely swear that:

1. This work was done wholly or mainly while in candidature for the doctoral degree at this faculty and university;

2. Where any part of this thesis has previously been submitted for a degree or any other qualification at this university or any other institution, this has been clearly stated;

3. Where I have consulted the published work of others or myself, this is always clearly attributed;

4. Where I have quoted from the work of others or myself, the source is always given. This thesis is entirely my own work, with the exception of such quotations;

5. I have acknowledged all major sources of assistance;

6. Where the thesis is based on work done by myself jointly with others, I have made clear exactly what was done by others and what I have contributed myself;

7. Part of this work has not been published before submission, and parts of this work have been published before as:

   - Singh S, Marquardt Y, ***Rimal R,*** Nishiguchi A, Huth S, Akashi M, Moeller M, Baron JM. Long-term and clinically relevant full-thickness human skin equivalent for psoriasis. ACS Applied Bio Materials. 2020 Sep 3;3(10):6639-47.
   - ***Rimal R***, Desai P, Marquez AB, Sieg K, Marquardt Y, Singh S. 3D vascularized breast cancer model to study the role of osteoblast in formation of a pre-metastatic niche. Scientific Reports. 2021 Nov 9;11(1):21966.
   - ***Rimal R,*** Marquardt Y, Nevolianis T, Djeljadini S, Marquez AB, Huth S, Chigrin DN, Wessling M, Baron JM, Möller M, Singh S. Dynamic flow enables long-term maintenance of 3-D vascularized human skin models. Applied Materials Today. 2021 Dec 1;25:101213.

- ***Rimal, R***., Muduli, S., Desai, P., Marquez, A. B., Möller, M., Platzman, I., Spatz J, Singh, S. (2024). Vascularized Three-Dimensional Human Skin Models in The Forefront of Dermatological Research. **Advanced Healthcare Materials**, 2303351.

Date: 20.03.2024

Rahul Rimal

Author's contributions

- Publication (incorporated in chapter 2): I performed the literature review and wrote the manuscript, which was revised and corrected by Dr. S. Singh, Dr. Ilia Platzman, and Prof-Joachim Spatz. Muduli S, Marquez A.B and Desai. P supported in the writing of the article. All authors finalized the manuscript.

- Publication (incorporated in chapter 3): I optimized and fabricated the skin models. I supported in writing the manuscript and supported the data analysis. Marquardt Y performed the PCR and assisted in optimizing the skin models. Nishiguchi A and Huth S, and JM Baron proofread and reviewed the manuscript. Dr. S. Singh supervised the project and wrote the manuscript. All the authors finalized the manuscript.

- Publication (incorporated in chapter 4): I optimized and fabricated the skin models, and performed in-vitro experiments including staining, cellular assays, microscopy, and analysis. I wrote the manuscript, planned, and analyzed the data. Marquardt Y performed the PCR. Nevolianis T and Chigrin DN performed the simulations. Djeljadini S and Wessling M designed CAD and printed the bioreactor used for skin models. IZKF performed the gene chip experiments and I analyzed the data. Marquez A.B. and Huth S assisted in manuscript proof-reading. Dr. S. Singh and I conceptualized the bioreactor. Dr. S. Singh supervised the project. All the authors finalized the manuscript.

- Publication (incorporated in chapter 5): I optimized and fabricated the cancer model, and performed in-vitro experiments including staining, cellular assays, microscopy, and analysis. I wrote the manuscript, planned, and analyzed the data of this chapter. Desai P, Marquez A.B, and Sieg K assisted in performing in-vitro assays. Marquardt Y assisted in performing gene chip experiments. IZKF performed the gene chip experiments and I analyzed the data. Dr. S. Singh supervised the project. All the authors finalized the manuscript.

Scientific Publications

- Singh S, Marquardt Y, ***Rimal R,*** Nishiguchi A, Huth S, Akashi M, Moeller M, Baron JM. Long-term and clinically relevant full-thickness human skin equivalent for psoriasis. **ACS Applied Bio Materials**. 2020 Sep 3;3(10):6639-47.

- ***Rimal R***, Desai P, Marquez AB, Sieg K, Marquardt Y, Singh S. 3D vascularized breast cancer model to study the role of osteoblast in formation of a pre-metastatic niche. **Scientific Reports**. 2021 Nov 9;11(1):21966.

- ***Rimal R,*** Marquardt Y, Nevolianis T, Djeljadini S, Marquez AB, Huth S, Chigrin DN, Wessling M, Baron JM, Möller M, Singh S. Dynamic flow enables long-term maintenance of 3-D vascularized human skin models. **Applied Materials Today**. 2021 Dec 1; 25:101213.

- ***Rimal, R***., Muduli, S., Desai, P., Marquez, A. B., Möller, M., Platzman, I, Spatz J, Singh, S. (2024). Vascularized Three-Dimensional Human Skin Models in The Forefront of Dermatological Research. **Advanced Healthcare Materials**, 2303351.

- Jain P*, ***Rimal R****, Möller M, Singh S. Topographical influence of electrospun basement membrane mimics on formation of cellular monolayer, **accepted, Scientific reports** ***(*equal contribution)***

- Staufer O, Dietrich F, ***Rimal R***, Schröter M, Fabritz S, Boehm H, Singh S, Möller M, Platzman I, Spatz JP. Bottom-up assembly of biomedical relevant fully synthetic extracellular vesicles. **Science Advances**. 2021 Sep 3;7(36): eabg6666.

- Desai P, ***Rimal R***, Florea A, Gumerov RA, Santi M, Sorokina AS, Sahnoun SE, Fischer T, Mottaghy FM, Morgenroth A, Mourran A. Tuning the elasticity of nanogels improves their circulation time by evading immune cells. **Angewandte Chemie International Edition**. 2022 May 9;61(20): e202116653.

- Hosseinnejad A, Ludwig N, Wienkamp AK, ***Rimal R***, Bleilevens C, Rossaint R, Rossaint J, Singh S. DNase I functional microgels for neutrophil extracellular trap disruption. **Biomaterials science**. 2022;10(1):85-99.

- Desai P, ***Rimal R***, Sahnoun SE, Mottaghy FM, Möller M, Morgenroth A, Singh S. Radiolabeled Nanocarriers as Theranostics—Advancement from Peptides to Nanocarriers. **Small.** 2022 Jun;18(25):2200673.

Scientific conference presentations

- Rapid oral presentation and Poster Presentation on a new approach towards the development of 3D skin models for Psoriasis at **Helmholtz Symposium Aachen**, 2019.
- Oral Presentation in-vitro human skin models at **HairS 2019**, Schlussee, Germany.
- Virtual oral poster presentation long-term skin models for psoriasis, 2020 **Carnegie Mellon Forum** on Biomedical Engineering.
- Virtual oral presentation on Scaffold-free approaches in Tissue Engineering, **6th TERMIS congress 2021.**

TABLE OF CONTENTS

List of Abbreviations

2D	Two-dimensional
3D	Three-dimensional
AB-EC	Adult blood endothelial cells
AD	Atopic dermatitis
ALI	Air-liquid interface
ANG	Angiogenin
BCC	Breast cancer cells
BMD	Bone mineral density
BSA	Bovine serum albumin
BV	Blood vessels
CB-EC	Umbilical cord endothelial cells
CCL	Chemokine ligand
CD	Cluster of Differentiation
COL	Collagen
CS	Cell-sheets
CTX	C-terminal telo peptide
CXCL	Chemokine ligand
DCP	Deeper cutaneous plexus
DEG	Differentially expressed genes
DEJ	Dermal-epidermal junction
DFS	Disease free survival
ECM	Extracellular matrix
ELISA	Enzyme-Linked Immunosorbent Assay
EPC	Endothelial progenitor cells
ESAF	Endothelial stimulating angiogenesis factor
FAK	Focal adhesion kinase
FBS	Fetal bovine serum
FCS	Fetal calf serum
FGF	Fibroblast growth factor
FLG	Filaggrin
FN	Fibronectin
GFP	Green fluorescence protein
GM-CSF	Granulocyte-macrophage colony-stimulating factor
GO	Gene ontology
hAMECs	Human adipose microvascular endothelial cells
hASCs	Human adipose stem cells
HDMEC	Human dermal endothelial cells
HIF	Hypoxia inducible factor
hLECs	Lymphatic endothelial cells
HSE	Human skin equivalent
HSP	Heat shock protein
HUVECs	Human umbilical vein endothelial cells
IFN	Interferon
IL	Interleukins
iPSC	Induced pluripotent stem cells

ITG	Integrin
K	Keratin
KC	Keratinocytes
KGM	Keratinocyte growth medium
MCP	Monocyte chemoattractant protein
MMP	Matrix metalloproteases
NHDF	Normal human dermal fibroblasts
NHEK	Normal human epithelial keratinocytes
NHFB	Normal human fibroblasts
NIK	Near-diploid human keratinocyte cell line
OBs	Osteoblasts
OPG	Osteoprotegerin
PASI	Psoriasis area and severity index
PCR	Polymerase chain reaction
PDAC	Pancreatic ductal carcinoma cell
PDGF	Platelet derived growth factor
PECAM	Endothelial adhesion protein
PFA	Paraformaldehyde
PPI	Protein-protein interaction
QCM-D	Quartz crystal microbalance with dissipation
RBC	Red blood cells
RHE	Reconstructed human epidermis
RNA	Ribonucleic acid
SC	Steartrimonium chloride
SLS	Sodium lauryl sulfate
SSP	Sub-papillary plexus
TEER	Trans-epithelial electrical resistance
TEM	Transmission electron microscopy
TGF	Transformin growth factor
TIMPs	Tissue inhibitor of metalloproteinase
TME	Tumor microenvironment
TNBC	Triple negative breast cancer
TNF	Tumor necrosis factor
UV	Ultraviolet
VBCT	Vascularized breast cancer tissue
VEGF	Vascular endothelial growth factor
vHSM	Vascularized human skin models
ZO	Zonula occludens

Abstract

The advancement of tissue engineering techniques has provided an alternate strategy for accessing and predicting the efficacy of novel pharmaceuticals and cosmetics. The urgent need for three-dimensional (3D) organotypic models stems from the limitations of the conventional testing platforms, including two-dimensional (2D) cell monolayers that fail to replicate the intricate architecture of the human tissue and animal models that raise ethical concerns. To compete with these existing pre-clinical platforms, organotypic 3D models need to exhibit longevity and stability. However, most in-vitro studies are conducted for short durations, thereby impeding the understanding of disease progression, long-term influence of the administered drugs/cosmetics, and the consequences of treatment discontinuation.

In this thesis, to fabricate 3D human skin tissue models, we employed ECM cell-coating and accumulation technique where individual dermal fibroblast was coated layer-by-layer with fibronectin (FN) and gelatin (G). The coated cells, once accumulated in a confined space, interact with each other to form a scaffold-free 3D tissue. Human keratinocytes were seeded on top of the formed dermis and the models were subsequently cultured in air-liquid interface (ALI) to mimic native skin architecture. The scaffold-free skin models showed long-term durability (49 days) where the epidermal compartment sustained its differentiated phenotype without infiltration of keratinocytes into the dermal compartment. Given this robustness, the skin models were utilized to simulate psoriasis, an incurable, immune-mediated inflammatory disease and a clinically approved drug was tested on the skin models. To induce a psoriasis-like phenotype, the skin models were stimulated with recombinant human interleukin 17A (rhIL-17A). Following stimulation, the skin models were systemically treated with the anti-IL-17A antibody Secukinumab in the presence of rhIL-17A. Microarray and RT-PCR analysis revealed that skin models treated with rhIL-17A showed downregulation of differentiation markers and upregulation of chemokines and cytokines, while treatment with anti-IL-17A antibody reversed these gene regulations. These findings demonstrated, at the molecular level, the effects of anti-IL-17A antibody on rhIL-17A-induced gene regulations, highlighting the physiological relevance of the developed skin model as an alternative to animal experiments. Therefore, the entire course of the disease, from the onset of the disease phenotype to the drug administration and the subsequent drug efficacy, was recapitulated in-vitro.

Similarly, in another study, long-term models of atopic dermatitis were established by exposing the skin models to Interleukin 4 (IL-4) and Interleukin 13 (IL-13). Atopic dermatitis is a common skin disease characterized by immune infiltration and activation, resulting in inflammation, vascular changes, and disruption of the skin barrier. Upon successful fabrication of the dermatitis models, a standard topical spheroid was applied and the histological changes were observed on the scaffold-free disease models.

Another approach to enhance the longevity of laboratory-cultured tissues involves providing nutrients to the tissue through a network of blood vessels (BV). Vascularization is a prevailing challenge in the field of tissue engineering. Although vascularization is known to improve the longevity of skin models by transporting nutrients, growth factors and oxygen, BV in in-long-term vitro models tend to be inherently unstable. The interplay of different cell types in within the models leads to alterations in the vascular system, which can be detrimental for the long-term stability of the functional BV. Skin models consists of human fibroblasts and keratinocytes that uniquely stimulate the BV. In ECM-coated scaffold-free models, the addition of keratinocytes led to uncontrolled angiogenesis and the formation of abnormal BV. Enhanced vascular growth factor (VEGF) and proteinases activity was observed after the addition of keratinocytes. To prevent this instability, the skin models were cultured within a 3D-printed bioreactor that provided continuous media perfusion to the vascularized skin tissues. Dynamic flow culture restored tissue homeostasis by balancing the expression of proteinase and their inhibitors, and regulating angiogenesis. This led to improvements in skin barrier properties, facilitated the fabrication of thicker tissues, and enhanced wound closure. Furthermore, the vascularized skin in flow culture promoted vascular openings as perfusable sites. In summary, the use of scaffold-free models and the bioreactor enabled the cultivation of the vascularized models with intact BV for a duration of 28-day.

ECM-coated scaffold-free methods were also utilized to form vascularized breast cancer models where the ECM-coated fibroblasts were mixed together with endothelial cells and cancer cells. Specifically, triple-negative breast cancer cells (MDA-MB231) were utilized to create the vascularized tumor model. The breast cancer cells exhibited highly elongated morphology within the in-vitro tissue compared to the 2D culture. Within the 3D microenvironment, breast cancer cells led to vascular abnormality, a hallmark of cancer. Furthermore, the breast cancer models were co-cultured with osteoblasts (bone-forming cells) to understand the paracrine effect of osteoblasts on the cancerous tissue, thereby constituting a complex four-cellular tumor progression model. Co-culture with osteoblasts in the presence of cancer cells, led to increased BV tortuosity and impairment.

Overall, this doctoral thesis focuses on the utilization of human 3D scaffold-free models to replicate various pathologies, ranging from skin diseases to cancer. These models demonstrate a long-term stability in culture, enabling extended drug treatment and analysis. Furthermore, the thesis investigates the alterations in vasculature in static culture condition and emphasizes on the necessity of dynamic flow culture conditions.

Zusammenfassung

Das Voranschreiten von Tissue-Engineering Verfahren hat eine alternative Strategie zur Prüfung und Vorhersage der Wirksamkeit und Sicherheit neuer Arzneimittel und Kosmetika ermöglicht. Der Bedarf an dreidimensionalen (3D) organotypischen Modellen ist auf die Limitierungen der herkömmlichen Testplattformen zurückzuführen. Zu diesen Plattformen gehören 2D-Modelle, die die komplexe Architektur des menschlichen Gewebes nicht nachbilden können, und Tiermodelle, die mit ethischen Problemen behaftet sind. Um mit diesen bestehenden Plattformen konkurrieren zu können, sollten organotypische 3D-Modelle dilanglebig und stabil sein. Die meisten In-vitro-Studien werden jedoch nur über einen kurzen Zeitraum durchgeführt, dies verhindert ein genaueres Verständnis des fortwährenden Krankheitsverlaufs, des Langzeiteffekts angewandter Medikamente und der Folgen eines Absetzens der Behandlung.

In dieser Arbeit wurde zur Herstellung von 3D-Hautgewebemodellen die ECM-Zellbeschichtung und -Akkumulationstechnik verwendet, bei der einzelne dermale Fibroblasten schichtweise mit Fibronectin (FN) und Gelatine (G) beschichtet wurden. Nachdem sich die beschichteten Zellen in einem begrenzten Raum angesammelt haben, interagieren sie miteinander und bilden ein Scaffold freies 3D-Gewebe. Auf die gebildete dermis wurden menschliche Keratinozyten aufgebracht und die Modelle wurden anschließend in einer air-liquid Grenzfläche kultiviert, um die Umgebung der natürlichen Haut zu imitieren. Die scaffold freien Hautmodelle zeigten eine lange Beständigkeit (49 Tage), wobei das epidermale Kompartiment seinen differenzierten Phänotyp ohne Infiltration in das dermale Kompartiment beibehielt. Aufgrund dieser Robustheit wurden die Hautmodelle zur Nachahmung der Psoriasis (einer unheilbaren, immunvermittelten Entzündungskrankheit) verwendet und klinisch zugelassene Arzneimittel an den Modellen erprobt. Um einen Psoriasis-Phänotyp zu erzeugen, wurden die Hautmodelle mit rekombinantem humanem Interleukin 17A (rhIL-17A) stimuliert. Anschließend wurden die Hautmodelle systematisch mit dem Anti-IL-17A-Antikörper Secukinumab in Gegenwart von rhIL-17A behandelt. Microarray- und RT-PCR-Analysen zeigten, dass die mit rhIL-17A behandelten Hautmodelle eine Herunterregulierung von Differenzierungsmarkern und eine Hochregulierung von Chemokinen und Zytokinen aufwiesen, während die Behandlung mit dem Anti-IL-17A-Antikörper diese Genregulationen umkehrte. Diese Daten bewiesen auf molekularer Ebene die Auswirkungen des Anti-IL-17A-Antikörpers auf die durch rhIL-17A hervorgerufenen Genregulationen. Dies zeigt die physiologische Relevanz des entwickelten Hautmodells und eröffnet Möglichkeiten für seinen Einsatz als Alternative zu Ex-vivo-Hautexplantaten und Tierversuchen. So konnte der gesamte Krankheitsverlauf, vom Auftreten des Krankheitsphänotyps, über die Zugabe des Medikaments bis hin zur anschließenden Wirksamkeit des Medikaments, in vitro nachgeahmt werden.

In ähnlicher Weise wurden Langzeitmodelle der Atopischen Dermatitis hergestellt, indem die Hautmodelle mit Interleukin 4 (IL-4) und Interleukin 13 (IL-13) exponiert wurden. Atopische Dermatitis ist eine verbreitete Hauterkrankung, bei der Immuninfiltration und -aktivierung zu Entzündungen, Gefäßveränderungen und einer Störung der Hautbarriere führen. Nach erfolgreicher Herstellung der Dermatitis-Modelle wurde ein gängiges topisches Steroide aufgebracht und die histologischen Veränderungen an den Scaffold freien Krankheitsmodellen beobachtet.

Ein weiterer Ansatz zur Verbesserung der Langlebigkeit von im Labor gezüchteten Geweben ist die Versorgung des Gewebes mit Nährstoffen über ein Netzwerk von Blutgefäßen. Die Vaskularisierung ist eine der größten Herausforderungen auf dem Gebiet des Tissue Engineering. Obwohl man annimmt, dass die Vaskularisierung die Langlebigkeit von Hautmodellen durch den Transport von Nährstoffen, Wachstumsfaktoren und Sauerstoff verbessert, sind die Gefäße in In-vitro-Modellen selbst instabil. Das Zusammenwirken verschiedener Zelltypen führt zu Veränderungen im Gefäßsystem, was für die Stabilität der funktionellen Blutgefäße nachteilig sein kann. Hautmodelle bestehen aus menschlichen Fibroblasten und Keratinozyten, die die Blutgefäße in besonderer Weise stimulieren. In ECM-beschichteten Scaffold freien Modellen führte die Zugabe von Keratinozyten zu einer unkontrollierten Angiogenese und der Bildung anormaler Blutgefäße. Nach der Zugabe von Keratinozyten wurde eine gesteigerte Aktivität des vaskulären Wachstumsfaktors (VEGF) und Proteasen beobachtet. Um dies zu verhindern, wurden die Hautmodelle in einem 3D-gedruckten Bioreaktor kultiviert, der das vaskularisierte Hautgewebe kontinuierlich mit Durchfluss versorgt. Die dynamische Flow-Kultur stellte die Gewebehomöostase wieder her, indem sie die Expression von Proteasen und deren Inhibitoren ausglich und die Angiogenese regulierte. Dies führte zu einer Verbesserung der Barriereeigenschaften der Haut, erleichterte die Herstellung von dickerem Gewebe und verbesserte den Wundverschluss. Darüber hinaus begünstigte die vaskularisierte Haut in der Strömungskultur Gefäßöffnungen als durchströmbare Stellen. Zusammenfassend ermöglichte der Bioreaktor, die vaskularisierten Modelle 28 Tage lang mit intakten Blutgefäßen zu kultivieren.

ECM-beschichtete Scaffold freie Methoden wurden auch zur Bildung von Krebs-Modellen verwendet, bei denen beschichtete Fibroblasten mit Endothelzellen und Krebszellen gemischt wurden. Hier wurden dreifach negative Brustkrebszellen (MDA-MB231) zur Bildung eines vaskularisierten Tumormodells verwendet. Die Brustkrebs-Zellen zeigten im In-vitro-Gewebe eine stark elongierte Morphologie und führten zu Gefäßanomalien. Die Brustkrebs-Modelle wurden außerdem mit Osteoblasten (knochenbildenden Zellen) ko-kultiviert, um die parakrine Wirkung der Osteoblasten auf das Krebsgewebe zu verstehen, wodurch ein komplexes vierzelliges Tumorprogressionsmodell entstand. Die indirekte Co-Kultur des Gewebes mit Osteoblasten führte zu einer erhöhten Tortuosität der Blutgefäße und zu einer stärkeren Beeinträchtigung der vaskularität des Brustkrebsgewebes.

Allgemein konzentriert sich diese Doktorarbeit auf die Verwendung eines menschlichen Scaffold freien 3D-Modells zur Nachbildung verschiedener Pathologien, von Hautkrankheiten bis hin zu Krebs. Diese Modelle sind in der Lage, langfristig in der Kultur stabil zu bleiben, was eine erweiterte medikamentöse Behandlung und Analyse ermöglichten. In dieser Arbeit werden auch die Veränderungen des Gefäßsystems unter statischen Kulturbedingungen untersucht und die Notwendigkeit dynamischer Flusskulturbedingungen hervorgehoben.

Chapter 1

Summary

The ban of cosmetic testing on animals by the European Union and several other nations has ignited the need to develop alternate platforms for future drug/cosmetic testing. The debate to completely reduce and replace animal models for preclinical drug testing is underway. Therefore, the requisite of a fully human, three-dimensional, mechanically stable lab-grown tissue is in demand. Several alternate 3D models that has the potential to reduce and replace conventional 2D monolayer and animal models are shown in **Schematic 1**.

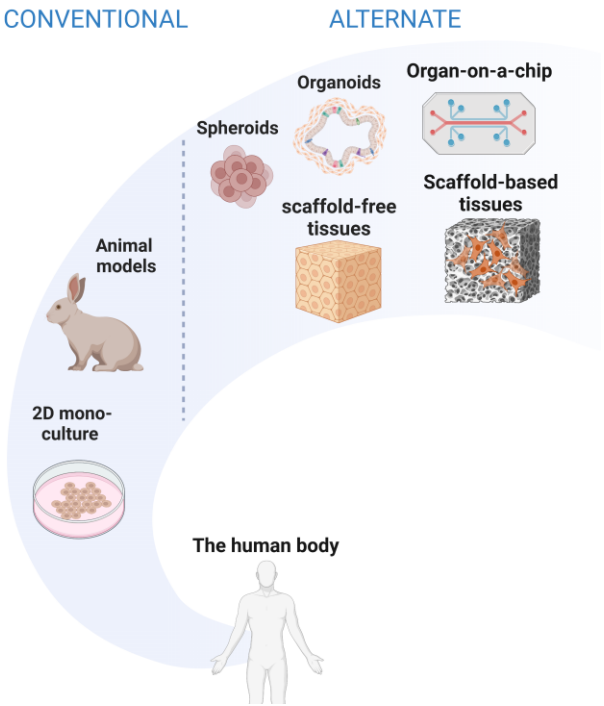

Schematic 1. *Depicts conventional and alternative pre-clinical drug and cosmetic testing platforms. Scaffold-based and scaffold-free tissues are the most relevant 3D in-vitro platforms for skin tissue engineering.*

Typically, 3D in-vitro models can be categorized into two main subgroups: 1) Scaffold-based and 2) Scaffold-free models. These models have distinct advantages and limitations. Scaffold-based models employ either natural or synthetic extracellular matrix (ECM) (in the form of hydrogels, porous substrates, and fibers) as the structural framework for the cells to attach and proliferate. These models allow for the precise control of the mechanical and biochemical properties of the formed matrix. However, these models do not accurately replicate the intricate diversity of ECM components found in native tissues. Additionally, longevity and stability are major issues in scaffold-based models as they

are susceptible to rapid tissue constriction and degradation. Conversely, scaffold-free models utilize the cell-derived ECM and rely primarily on cell-cell interactions to form the tissue. Limitations of scaffold-free models are the requirement of large quantities of cells, longer assembly times, and deposition of surrounding ECM. Despite these limitations, scaffold-free models better recapitulate the native tissue characteristics and could be utilized for long-term studies. This doctoral thesis focuses on the development of scaffold-free models of the healthy and diseased human skin and breast cancer, with a specific emphasis on vascularization and enhancement of longevity of these models.

There are several categories of scaffold-free models. These include 1) Spheroids (spherical 3D mass of cells), 2) Organoids (self-organized mass derived from stem cells that mimic specific organ), 3) Self-assembly of cell-sheets after long-term culture, 4) Cell-coating and accumulation models. In terms of scaffold-free skin tissue fabrication, self-assembly and cell-coating-accumulation technique are more advantageous compared to spheroids and organoids due to the ability to form larger tissue constructs, capability of the models to be cultured in air-liquid interface, ease of drug testing on both apical and basal side, and ease of handling. In self-assembly technique, highly confluent fibroblasts are treated with ascorbic acid, forcing the cells to produce and deposit ECM. After several weeks of culture, cells sheets are formed. These cell sheets are then assembled together to form a thick dermal tissue. Keratinocytes are then added on top of the assembled tissue and cultured in air-liquid interface. The disadvantage of cell sheets is the amount of time required for the cells to form the sheets. Cell-coating and accumulation technique, on the other hand, rapidly forms cellular interactions and allows for thick dermal tissue formation. In this technique, an artificial ECM nanolayer (fibronectin and gelatin) is coated around single cells. Fibronectin has a binding site with cell surface integrins and gelatin has a binding site to fibronectin. Therefore, an alternative layer-by-layer deposition of fibronectin and gelatin forms a fibrous Nano-ECM glue around single cells.

Using the ECM-coating and accumulation technique, models of skin diseases psoriasis and atopic dermatitis were mimicked. Keratinocytes added on top of a thick scaffold-free dermal tissue differentiate into different epidermal layers once exposed to air. A long-term air-liquid interface culture of the skin shows the relevancy of scaffold-free models in disease modelling and drug testing. An in-depth gene-level analysis of the influence of clinical drug Secukinumab was done on the psoriasis models.

Scaffold-free approach allowed the cultivation of long-term skin models. Next, similar technique was utilized to fabricate vascularized skin models. However, the longevity of vascularized models was compromised after the addition of keratinocytes. Post-addition of the keratinocytes, there was a drastic and uncontrolled increase in angiogenesis, which led to degradation of the dermis. Enhanced angiogenic and proteinase genes were observed post addition of keratinocytes. In order to circumvent these challenges, vascularized skin models were nourished with continuous media flow. Flow-treated

vascularized skin models showed controlled angiogenesis and minimal dermal degradation. Downregulation of angiogenic and proteinase genes were observed. Dynamic flow culture, therefore allowed for the formation of long-term stable vascularized skin models.

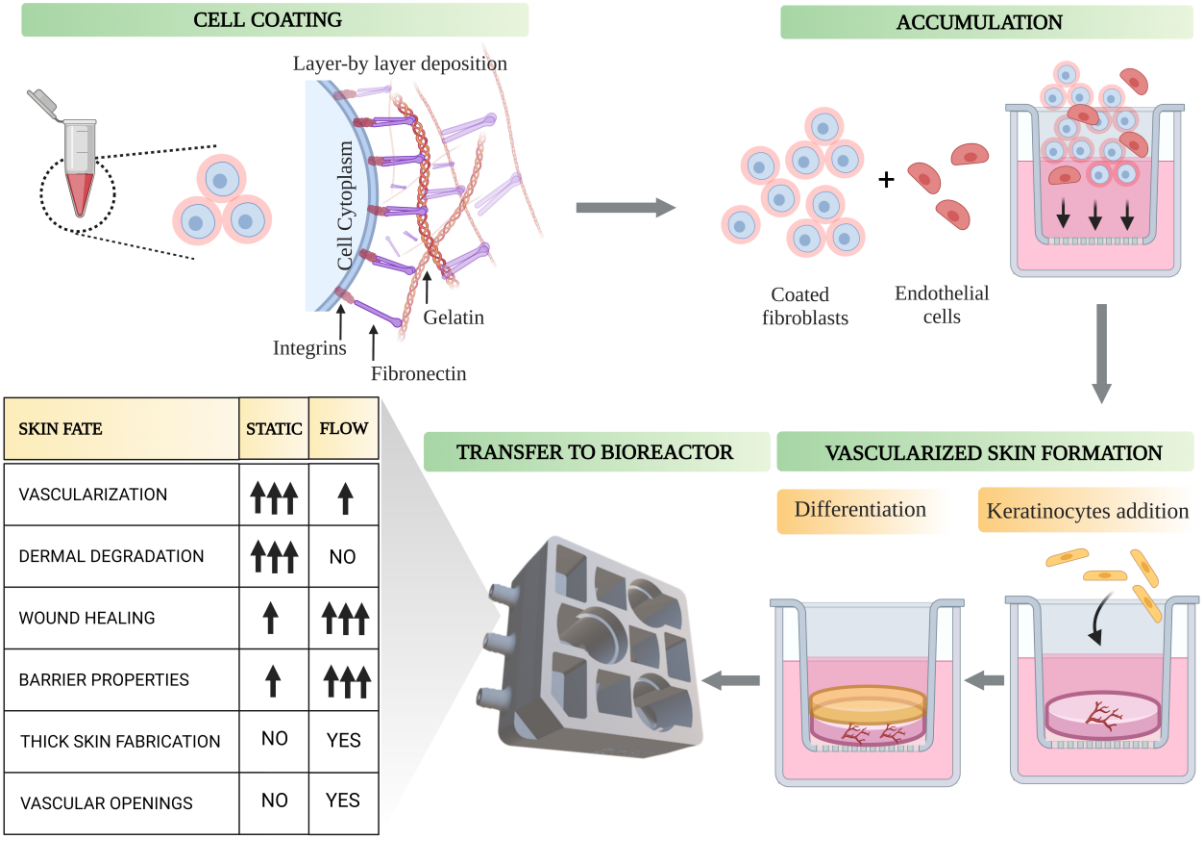

SKIN FATE	STATIC	FLOW
VASCULARIZATION	↑↑↑	↑
DERMAL DEGRADATION	↑↑↑	NO
WOUND HEALING	↑	↑↑↑
BARRIER PROPERTIES	↑	↑↑↑
THICK SKIN FABRICATION	NO	YES
VASCULAR OPENINGS	NO	YES

Schematic 2. *Shows the effect of continuous perfusion culture on the vascularized skin phenotype. Flow culture controls angiogenesis, reduces dermal degradation, and enhances skin barrier properties. Vascularized dermis was fabricated using layer-by-layer ECM coating on fibroblast and accumulated together with endothelial cells. Keratinocytes were seeded on top of the dermis and exposed to air to form the epidermis.*[1]

This was attributed to 1) better diffusion of media throughout the skin tissue, thereby improvement in cellular viability, and 2) direct mechanical influence on the tissue that led to gene-level changes in the cells. Apart from improvement in vascularization and prevention of dermal degradation, the improvement of barrier properties in the epidermis was also observed. This makes flow-treated models suitable for pre-clinical drug penetration and absorption tests. Several other aspects of the skin models were improved **(Schematic 2).** Abnormal vasculature is a hallmark of cancer. Vascularized scaffold-free models that have a high cell density and cell-derived ECM forms an optimal microenvironment for cancer migration and propagation. Breast cancer shows high tropism towards bone and is known to preferentially form secondary metastasis sites on bones. In order to understand the crosstalk between a primary tumor microenvironment and bone cells, a coculture system was developed. Scaffold-free

vascularized fibroblastic tissues were seeded together with triple-negative breast cancer cells to form a 3D tumor tissue. This tissue was indirectly co-cultured with bone forming cells, the osteoblasts in order to deliberate the impact of osteoblasts on the primary tumor microenvironment. Tortuous, open-ended and abnormal blood vessels were observed in the tissues incorporating breast cancer cells and the vascular deformations were significantly increased in the presence of osteoblasts.

1.1. Contents of this thesis

This thesis is divided into five chapters.

Chapter 2 discusses the longevity of ECM-coated scaffold-free skin models and their utilization in mimicking psoriasis, a common skin ailment. Psoriasis was induced by the addition of inflammatory cytokine IL-17. The chapter then focuses on the testing Secukinumab (an anti-IL17 antibody) to show the influence of the drug on psoriasis.

Chapter 3 gives a literature overview of skin models, focusing on vascularization. Vascularization of tissue engineered models is one of the biggest prevailing challenge in the field. Blood vessels not only functions as biological pipelines to deliver nutrient, growth factors and oxygen but also interacts with different cell types in the skin to spearhead disease progression and inception. Therefore, the inclusion of vessels within skin models is an important step in order to fabricate an alternate to animal models. This chapter discusses the need of vascularization and several techniques of fabricating vascularized skin models.

Chapter 4 focuses on the fabrication of long-term vascularized scaffold-free skin models. This chapter first points out the changes in angiogenesis due to the presence of multiple cell types in the skin model. Keratinocytes-derived factors lead to enhanced angiogenesis and dermal degradation due to uncontrolled vessel proliferation. The chapter then focuses on the means to control the vascular fate by using 3D printed bioreactor that continuously provides perfusion to the skin models. The chapter shows how perfusion culture can control angiogenesis, lead modulation in angiogenic genes, give the ability to form thick vascularized tissue, and lead to faster wound closure.

Chapter 5 focuses on the formation of scaffold-free breast cancer models. This chapter shows the change in the morphology of breast cancer cells within scaffold-free models. To mimic bone-breast cancer interaction, a system was developed where vascularized breast cancer model was indirectly co-cultured with bone-forming cells, osteoblasts. This chapter discusses the change in angiogenesis in the presence of breast cancer cells and osteoblasts.

Appendix shows the development of vascularized atopic dermatitis models. This chapter then focuses on the application of clinically available steroid and preliminary effect of the steroid on atopic dermatitis reduction.

Chapter 2

Vascularized three-dimensional human skin models

This chapter was adapted with permission from the publication "Vascularized 3D human skin models in the forefront of dermatological research" in *Advanced healthcare materials.* 2024 Jan 26; :2303351.

Direct link: https://doi.org/10.1002/adhm.202303351

All schematics were created using Biorender.

2.1. Introduction

Skin-related ailments are globally prevalent and have a detrimental impact on patients' well-being.[2-4] To combat skin disorders, patients rely on a limited number of drugs available in the market. Some of the challenges associated with the availability of novel drugs include their slow upgrade from pre-clinical laboratory settings to clinical trials, failed clinical trial outcomes, and unexpected side effects. Advancements in pre-screening are vital to resolve these issues and facilitate the turnover of novel therapeutical agents to clinical products. Beyond the extensive use of conventional two-dimensional (2D) monolayers and animals as tools for pre-clinical drug testing, a rapidly emerging alternative involves the utilization of *in-vitro* three-dimensional (3D) human skin models. The prevailing tissue-engineered skin models recapitulate the elementary anatomy and physiology of native healthy and disease-like skin tissue and can provide valuable readings about drug penetration, absorption, and toxicity. Nevertheless, more realistic skin models that can accurately mimic the native skin cell organization and functionality, and has the potential to fully replace conventional pre-clinical models are in high demand.

To evolve *in-vitro* skin models from an alternative method to a mainstream platform, researchers have attempted to develop novel skin models with a) enhanced barrier properties, b) multiple cell types comparable to the cellular diversity of native skin tissue, c) optimal media composition to facilitate the survival of the skin models and d) technologies that enable long-term durability and maintenance of skin models such as the utilization of microfluidics and bioreactors.

The inclusion of different cell types has a paramount influence on skin physiology. It is recognized that skin models require a certain level of complexity to recapitulate the physiology of human tissues. For instance, the reconstructed human epidermis (RHE) models that comprise only the epidermis compartment of the skin are the simplest representation of skin tissue. However, the need for an underlying fibroblast compartment to facilitate optimal epidermal differentiation is widely accepted.[5,

[6] Similarly, the inclusion of the other cell types namely the endothelial cells, immune cells, neuronal cells, lymphatic cells, and skin appendages could have distinct responses to the application of novel drugs and cosmetics. One important cell type that has a significant impact on skin homeostasis is the endothelial cells (ECs) that form the network of blood vessels. Tissues that are thicker than 100-200 μm necessitate sufficient vascularization for the proper transport of essential nutrients, growth factors, and oxygen to the cells as well as the removal of metabolic waste from the tissue.[7] Apart from their role as biological pipelines, ECs are also involved in innumerable cellular cross-talks with diverse cell types, together maintaining homeostasis. Blood vessels also have a vast implication in several skin-related ailments. For instance, in inflammatory skin diseases such as psoriasis and atopic dermatitis, blood vessels act as cofactors and spearhead disease progression. Additionally, in skin grafts for burn injuries, pre-vascularization has been shown to facilitate better integration with the host tissue, enabling long-term survival of the implanted grafts. Therefore, there is a need for the development of fully-vascularized in-vitro human skin models to mirror disease progression, to be utilized as skin grafts, and as a platform for pre-clinical assays.

There has been a variety of novel approaches to tackle the increasing need for vascularized human skin models (vHSMs). The advent of bio-printing and microfluidic techniques, the introduction of novel biomaterials, and increased industrial and clinical demands have helped shape the progress of the current skin tissue engineering landscape. This chapter summarizes the past and current techniques used for the fabrication of vHSMs, emphasizes the necessity of vascularization, and highlights some of the current challenges in the fabrication of reliable skin models.

The need for alternate to animal models

Conventionally, the screening of drugs and cosmetics has been carried out using 2D cultures and animals. 2D cultures comprise cells seeded as a monolayer and offer the simplest representation of human tissues. Irrespective of their simplicity and high-throughput, monolayers are inept in mirroring the intricate native tissue architecture. Cell morphology, motility, and differentiability are directly associated with the culture environment. The homogenous distribution of culture medium on a 2D monolayer supplies essential growth factors, nutrients, and gases to individual cells uniformly, which does not mirror the reality of nutrient distribution within a thick native tissue. Monolayer culture conditions do not favour optimum cell-cell and cell-ECM interactions because cells on a flat surface physically communicate only with their adjacent cells. Conversely, animal models possess the complexity of human tissues and can provide better predictions on drugs and cosmetics efficacy. However, animal models have been continually questioned for their anatomical, physiological and molecular resemblance with the human tissues.[8]

In order to understand the need to replace animal models for skin research, the dissimilarity of animal skin to human skin, and the limitations of animal models beyond ethical issues has to be explored. Out

of all the animal models, porcine skin is highly similar both anatomically and immunologically with the human skin. There are however differences pertaining to the modulus between porcine and human skin, possibly due to the differences in the elastic fibers and lipid content[9, 10] Gallagher et al. recently studied the mechanical properties of porcine and human burned skin tissues and reported significant differences in the values. This was attributed to the differences in elastic fibers and lipid content, and the ability to retain moisture at higher temperatures.[9]

Another common animal model used as a substitute to mimic for skin diseases and wounds are the murine models. Although murine models have been employed in the past for dermatological studies, there are noticeable anatomical and functional differences compared to human skin tissue. Firstly, there is an obvious difference in thickness of the skin (approximately 100 μm in human skin as compared to <25 μm in murine skin).[11] Human skin also comprise more cellular layers in the epidermis as compared to that of the murine skin. Furthermore, the renewal of epidermis in the murine skin is <10 days, whereas human skin takes a longer time (approximately 28 days) to renew completely. These differences in skin architecture can have a major implication in the accurate modelling of skin diseases and the testing of novel therapeutics, especially questioning the outcomes of drug absorption tests. Murine and human skin also differ in cutaneous wound healing mechanism. Murine skin heals wound primarily by the mechanism of contraction, whereas human skin mostly develops granulation tissue and undergoes re-epithelialisation.[12] Murine skin comprises panniculus carnosus, a layer of thin striated muscle, directly beneath the skin, which is mostly absent in the humans that facilitate the contraction.

Apart from morphological differences, the gene-level differences between animal and human skin cells are important. Using global transcriptomic profiling, it was shown that murine models were not able to recapitulate accurately two main clinical features of Atopic Dermatitis (AD) namely a) epidermal barrier disruption, and b) immune response.[13] Six common murine models were tested and the transcriptomic analysis showed differential profiles as compared to human AD samples.[13] In a more optimistic study, gene expression in five selected mouse models of psoriasis was found to exhibit significant similarities with that of clinical psoriasis.[14] However, the study also highlighted that there were significant differences in immune-associated gene expression between the mouse models and human psoriasis. In conclusion, a consensus on the pre-selection of distinct murine models for skin disease modelling has yet to be reached and the selection of incorrect murine models could result in failed clinical trials and skewed outcomes.

Anatomy of the vascularized human skin

Skin is a 3D hierarchical tissue that comprise three distinct layers namely epidermis, dermis, and hypodermis.[15] The outermost layer of the skin, the epidermis endures the physical, chemical, and microbial traumas in order to guard the body against infections, functions to prevent dehydration, and eradicate toxins.[16, 17] The epidermis houses several cell populations, namely the keratinocytes,

pigment-producing Melanocytes, antigen-presenting Langerhans cells, and Merkel cells, with keratinocytes occupying 90% of the epidermal cell population.[15, 18] The epidermis is composed of distinct sub-layers with dedicated functionalities **(Figure 2.1B)**. Keratinocytes in the epidermal layers interact with each other via desmosomes and tight junctions **(Figure 2.1C)**. Stratum Basale, the deepest cell layer of the epidermis, firmly adhere to the underlying dermal compartment via the dermal-epidermal junction (DEJs). Some cells from the stratum basal detach, proliferate and migrate upwards forming the other upper layers namely Stratum spinosum, Stratum granulosum, Stratum lucidum, and finally the Stratum corneum (the exterior layer of the epidermis). The granular layer comprises squamous keratinocytes that expresses filaggrin (FLG) and loricrin, and are essential in skin permeability. The differentiated cells that form the stratum cornea are anucleated, flattened, and are continuously replaced by the inner keratinocytes that travels towards the skin surface.[16, 19, 20] This migration and upwards proliferation of keratinocytes gives the epidermal layer self-healing property and is accelerated when the skin is injured and prompts wound healing.[16]

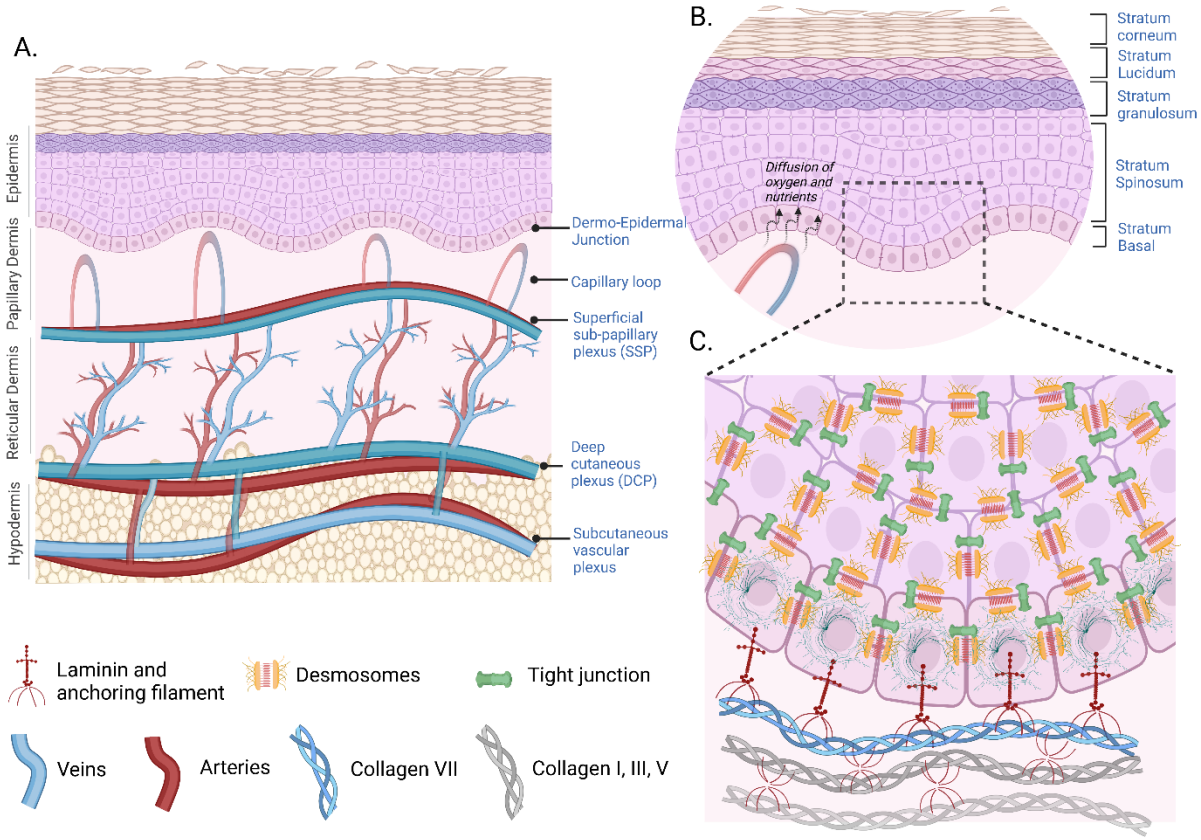

Figure 2.1. *Anatomy of vascularized skin A) distribution of blood vessels in the skin shows two primary horizontal arterial and venous plexuses that ascend to the superficial plexuses. Capillary loops from the superficial plexuses distribute and diffuse nutrients and oxygen to the epidermal compartment. B, C) A magnified view of the dermo-epidermal junction and the epidermal compartment shows interaction of basal keratinocytes with the underlying basement membrane via anchoring filaments. Keratinocytes interact with each other via tight junctions and desmosomes.*

The dermis lies between the epidermis and the hypodermis; it encompasses the bulk of the skin and is known to provide structure and strength. The dermis is split into two sub-layers, the superficial papillary and the deeper reticular dermal layers. Fibroblasts are the main cellular population in the papillary dermal layer and play a role in maintaining the skin's elasticity, and tensile strength by releasing collagen and elastin.[21] The reticular dermal layer mainly consists of dense connective tissue containing bundles of collagen fibers and elastic fibers, which gives the skin its flexibility.[22] The deepest layer of the skin is the adipose tissue hypodermis layer, which mainly contains cells that store fats. The presence of adipose tissues offers cushioning between the skin layers, muscles, and bones. Furthermore, the presence of proteoglycans and glycosaminoglycans serves as a nutrient reservoir by absorbing fluid into the tissue and giving it mucous-like properties.[23, 24] In addition to fibroblasts and keratinocytes, the skin contains large numbers of hair follicles, immune cells, melanocytes, merkel cells, nerve fibers and blood vessels.

The dermal and hypodermal compartment comprises an intricate network of blood vessels that supply nutrients, growth factors, and oxygen to the avascular epidermal compartment **(Figure 2.1B)**. There are two primary horizontal plexuses composed of arteries and veins in the dermal compartment namely the superficial sub-papillary plexus (SSP) and the deeper cutaneous plexus (DCP). Arterioles that supply blood to the muscles and the hypodermal layer form the DCP, which reside between the subcutaneous and the cutaneous compartment. The arteries and veins then arrange in a vertical vascular pattern to connect to the SSP, which reside between the epidermis and the papillary dermal compartment. The vessels in the DCP differ in morphology to the SSP. The DCP have wider diameter (10-35 μm in SSP and 40-50 μm in DCP) and thicker walls.[25] In the dermal papilla, individual arterioles form separate capillary loops which has an ascending limb, an intra-papillary loop and a descending limb which fuses with the post-capillary venules.[26, 27] **Figure 2.1A** depicts the schematic of vessel distrubution in skin. The capillary loop supply blood to 0.04 to 0.27 mm^2 of the skin.[25, 28] There are numerous anastomoses sites in the skin vasculature through which the blood flows and functions as temperature regulating units.[29]

Historical development of in-vitro skin models

Although it was known that basal keratinocytes in the human epidermis divide once every 14 days, the *in-vitro* expansibility of primary human keratinocytes was a challenge.[30] Rheinwald and Green in 1975, serially cultivated epidermal cells line (cell line XB) from mouse teratoma.[31] However, the cells couldn´t proliferate from low density plating in normal culture media. Researchers were then able to propagate epidermal cells (XB) into epidermal colonies when cultured together with lethally irradiated 3T3 fibroblast cells indefinitely.[32] This indicated the importance of a fibroblast-keratinocyte interaction in epidermal formation and differentiation. The in-vitro serial cultivation of human keratinocytes into stratified squamous epithelial layers from single human keratinocytes was an important milestone in the development of future skin models.[33, 34] Following this, Green et al.

fabricated keratinocyte sheets that could be harvested as skin grafts and used in clinical applications. Sheets were produced by seeding human keratinocytes on top of a supporting 3T3 feeder cell layer.[35] Such epidermal sheets were used for various applications such as allografts for skin ulcers[36], vitiligo[37], Epidermodysplasia verruciformis (EV),[38] and burn injuries.[39]

In 1981, Bell et al. fabricated a full thickness human skin models (HSMs) by seeding keratinocytes on top of collagen gel comprised of fibroblasts.[40] The contraction of the collagen matrix by the fibroblasts facilitated the formation of a dermal framework. The keratinocytes cultured on the collagenous dermis differentiated to generate the epidermal layers. The presence of fibroblast in the HSM significantly enhanced keratinocyte outgrowth, which was attributed to the release of fibroblast diffusible factors.[40] Bell's HSM was the first commercialized organ-mimicking model system. These models were vigorously tested for their morphological, biochemical and functional properties. Various substances such as Toluene, Formaldehyde and Resorcinol were tested on these bi-layered HSM and native human skin to compare their response to chemical irritants.[41] As time progressed, several derivations of the collagen-based models were established and various novel scaffold-based and scaffold-free techniques were developed, several of which (focused on vascularized models) will be discussed in the later section of this chapter.

2.2. The need for vascularization in skin models

Vasculature plays a critical role in skin homeostasis as well as in pathogenesis. Vascular remodelling and activation are often observed in the progression of numerous skin diseases. In a normal healthy skin tissue, angiogenesis is a conserved process where a delicate balance of the production of pro-angiogenic and anti-angiogenic factors leads to stable vasculature. However, in the case of diseases, this balance is affected, thereby leading to excess angiogenesis or regression of blood vessels. Since one of the end-goals of fabricating physiological HSMs is to model skin diseases, the presence of vascular elements is therefore a prerequisite.

Vascularization for skin grafts

The conception of a full-thickness skin model and its commercialization thereafter brought on a decade of revised skin models and grafts. However, it was quickly understood that the successful integration of these skin replacements necessitates adequate graft vascularization. One of the limiting factors in the fabrication of viable thick tissue *in vitro* is the transport of oxygen and nutrient to individual cells. Thin tissues can be nourished via diffusion but thicker (>1 cm) tissues demand vascular networks to prevent cell apoptosis and tissue necrosis.[42] Young et al. brought into question the significance of vascularization for artificial skin graft survival.[43] Young and his colleagues reported that skin grafts would survive by 1) imbibition; diffusion of essential nutrients from host 2) vascularization due to inosculation on day 2-5 followed by 3) neovascularization. Inosculation is the process where the host vasculature anastomoses with the pre-existing graft vasculature. Neovascularization, on the other hand

is the formation of new vascular sprouting from the host vasculature to the graft. Neovascularization was observed in the grafted skin replacements only after two weeks which hinted at the lengthy amount of time it would take to vascularise an avascular tissue. Neovascularization appeared as delayed process during which imbibition would not be sufficient to keep avascular skin substitute alive. Therefore, a pre-existing vasculature would favour inosculation and prevent graft failure.[43]

Vasculature in inflammatory skin diseases

Inflammation is one of immune system's biological responses that are triggered by various stimuli. The body's inflammatory reactions share a similar mechanism of action, a cascade of event that give rise to inflammation. These events are recognition of harmful stimuli by cell receptors, activation of inflammatory pathways, release of inflammatory cytokines and attraction of immune cells to the tissue.[44] Traditionally, the response of the body to inflammation is characterized by *rubor*, *tumor*, *calor*, and *dolor* which mean redness, swelling, heat, and pain, respectively. These responses are related to the local vasculature and are characteristic to inflammation. Increased blood flow enhances the redness and temperature to the affected area. As the metabolic activity is increased, vessels become leaky or more permeable resulting in swelling, which is followed by pain.[45] There is ample evidence that suggests that blood vessels act as a primary contributor in the inception and progression of inflammatory skin disease.

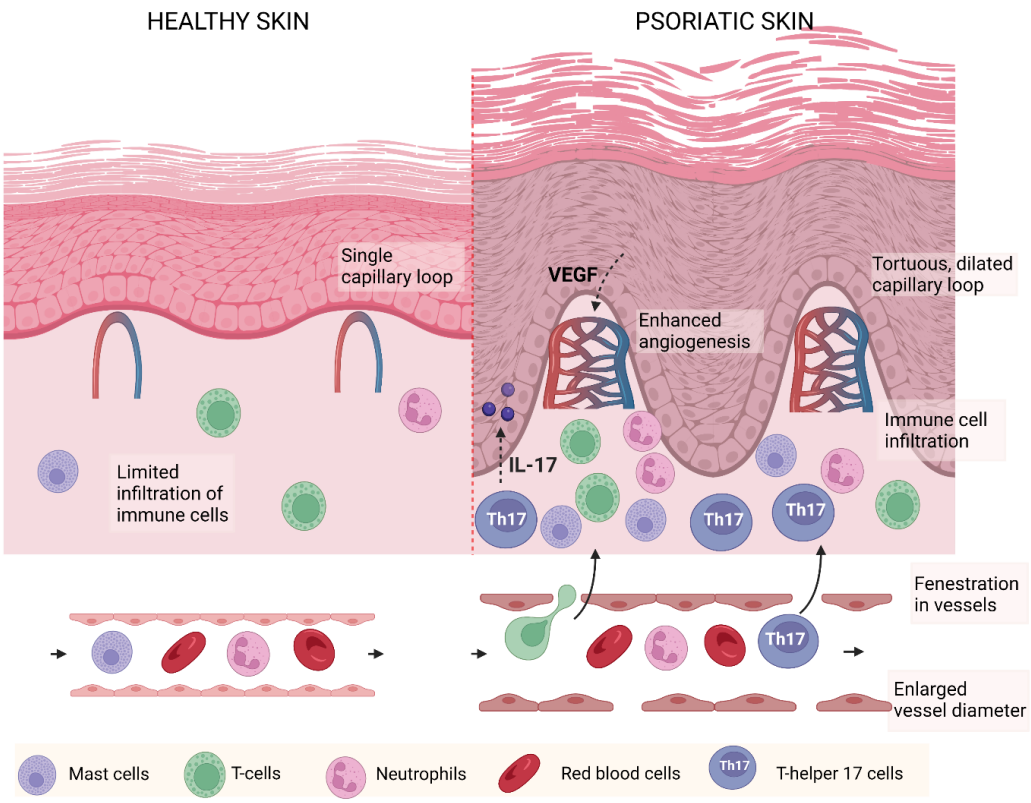

Figure 2.2. Role of blood vessels in Psoriasis *Inflammatory skin diseases such as psoriasis has a direct impact on vascularization. Upregulation of VEGF and other angiogenic factors from psoriatic*

keratinocytes and infiltrating immune cells lead to enhanced angiogenesis. In-turn, vascular enlargement and fenestrations lead to accumulation of immune cells in the inflamed area of the skin leading to a vicious circle of disease progression.

Psoriasis is an immune-mediated inflammatory skin ailment characterized by hyper-proliferation of epidermal keratinocytes. It is also related with the onset of other serious diseases such as psoriatic arthritis and cardiovascular complications.[46] It is observed that the vessels in psoriasis lesions dilate and are leaky, which lead to enhanced accumulation of immune cells in the lesion site.[47] In 1961, Telner et al. observed microvascular abnormalities in patient biopsies even before the appearance of the histological psoriatic lesions.[48] Structural abnormalities of the vasculature in early stages of psoriasis was a result of angiogenic inflammatory growth factors derived from infiltrating immune cells.[49]

Most of the alteration in vascular homeostasis occurs in psoriasis due to the presence of enhanced angiogenic factors and decreased anti-angiogenic factors. For instance, Nickoloff et al. showed that psoriatic keratinocytes promoted angiogenesis by a significant reduction in angiogenesis inhibitor thrombospondin-1 and increased production of pro-angiogenic interleukin IL-8.[50] Similarly, Bhushan et al. showed that the tissue levels of endothelial stimulating angiogenesis factor (ESAF) and VEGF were significantly upregulated in psoriatic plaques and correlate with the severity of the disease.[51] Previous observations have indicated the enhanced migration and proliferation of blood vessels in psoriasis via the increase in $\alpha_v\beta3$ integrin levels.[47, 52] These studies therefore indicate that vasculature plays a major role in psoriasis disease progression and fortifies the requisite of blood vessels in in-vitro skin models of psoriasis. **Figure 2.2** summarizes key changes in the psoriatic vasculature as compared to the healthy skin. Apart from the influence of vasculature in psoriasis, it has to also be considered that drugs applied to tackle psoriasis can have a direct and indirect impact on the blood vessels. For instance, Markham et al. tested infliximab, a tumor necrosis factor (TNF)-α blocker on psoriatic patients.[53] The anti-TNFα therapy showed to significantly downregulate angiogenic factors such as VEGF, ANG1, ANG2 and Tie2 receptor. Furthermore, decrease in endothelial adhesion protein PECAM and vascularity was observed. The inhibition of inflammation and EC deactivation by low-dose infliximab treatment led to a promising clinical response.[53] In a more direct approach, Neovastat (Æ-941), an angiogenesis inhibitor was used in a randomized phase I/II clinical trial and showed positive effects in the treatment of psoriatic plaques.[54] The requirement of vasculature is therefore not only limited to mimicking the actual psoriatic disease progression but to also to serve as a platform for anti-angiogenic drug testing.

Similar trends have been observed in other inflammatory skin diseases such as Atopic dermatitis (AD). **Table 2.1** lists the involvement of blood vessels in skin disease progression. AD is the most prevalent chronic inflammatory disease of the skin. A distinguishing characteristic of AD is chronic cutaneous inflammation which is accompanied by dry skin and dysfunction of the epidermal barrier. AD

previously has been linked to the presence of increased number of blood vessels as compared to normal skin tissues.[55] Angiogenesis in AD has been correlated to elevated levels of angiogenic growth factors where significant upregulation of VEGF in AD lesions has been observed as compared to normal skin samples.[56] Infiltration of immune cells is the hallmark of AD and several immune cells have shown to trigger angiogenesis during AD progression.

Table 2.1. *Vascular involvement in several inflammatory skin diseases*

Skin disorder	Angiogenic factors	Observation	References
Psoriasis	VEGF, HIF, TNF-α, IL-8, IL-17, E-selectin	• Significant vasodilation and vessel elongation • Increase tortuosity and vascular permeability • Enhanced proliferation and migration • Enhanced blood flow to the skin	[57] [58] [59] [47, 60, 61]
Atopic dermatitis	VEGF-A, VEGF-B, VCAM-1 Increased serum level of soluble ICAM-1, ICAM-3, E-selectin	• Hyper-permeability of blood vessels • Increased density of blood vessels • Persistent erythema and edema in AD	[56, 62] [63]
Rosacea	VEGF-A, mTORC1, LL-37, TNF-α, IL-8, D2-40 (lymphatic endothelium marker)	• Increased permeability of vessels • Flushing and erythema	[64-67]
Bullosa	VEGF, TGF-β	• Induction of increased microvascular permeability in bullous diseases • Leads to papillary edema and fibrin deposition	[68, 69]
Melanoma	VEGF, fibroblast growth factor (FGF), platelet derived growth factor (PDGF), TGF-α and β, IL-8	• Contributes to melanoma tumor growth and metastasis • Poor prognosis	[70-72]

Increased and abnormal vasculature is a hallmark of cancer.[73] Malignant melanoma is a common skin cancer and has been associated with rapid angiogenesis and vascular modelling. The aberrant vascular

sprouting is due to the presence of a hypoxic environment, secreted angiogenic growth factors such as VEGF, interleukins, FGF2, angiopoietins, and an upregulation of proteinases.[74] Erhard et al. showed that angiogenesis and increased VEGF production in melanoma microenvironment leads to vertical migration of cancer cells indicating metastatic phase.[75] Owing to the importance of blood vessels in melanoma, several therapeutic agents have been utilized in the past to target angiogenesis. For instance, several phase 1 and 2 clinical trials are based on VEGF receptor tyrosine kinase inhibitors. However, the patient response of anti-angiogenic therapies in melanoma (and cancer in general) has been unsatisfactory. Nevertheless, novel therapies that target blood vessels for skin cancer treatment are still under study.

2.3. Strategies to fabricate vascularized skin model

Numerous techniques have been taken to develop and improve vascularization in skin models. The main approaches are 1) providing an optimal 3D environment for the ECs to form vascular networks 2) development of vascular-permissive hydrogels 3) co-culture of ECs and fibroblasts 4) micro-fabrication of sacrificial channels as a framework for the attachment of ECs 5) inclusion of angiogenic growth factors as soluble factors or within the scaffold for prolonged release 6) utilization of decellularized tissues as scaffolds as they already possess the required intricate framework for vascularization 7) scaffold-free techniques that use cell-derived ECM for ECs permissive environment 8) genetically modified cells to express angiogenic factors or to prevent cell apoptosis 9) utilize microfluidic approaches with several cellular compartments.[76] **Table 2.2** lists several vHSMs that are commercially available. The preliminary step in the formation of vHSMs is the accurate choice of 3D environment to be provided to the cells depending on the experimental needs. The following part of the review summarizes the notable efforts in the fabrication of vHSMs.

Table 2.2. *Commercially available skin models and their applications*

Manufacturer	Skin Model	Description	Applications
Episkin	EpiSkin™	Human epidermis developed from normal human keratinocytes cultured on collagen matrix at the air-liquid interface	Skin irritation, Skin corrosion, UV exposure, DNA damage, Bacterial adhesion, Omics, and Permeability
	SkinEthic RHE™	Human epidermis developed from normal human keratinocytes cultured on inert polycarbonate filters at the air-liquid interface in a chemically defined media	Skin irritation, Skin corrosion, UV exposure, DNA damage, Bacterial adhesion, Omics, and Permeability and Medical devices

	T-Skin™	A human full-thickness model which consists of human fibroblasts overlaid by human keratinocytes on a tissue culture insert	UV exposure, DNA damage, Bacterial adhesion, Omics, and Permeability
	SkinEthic™ RHE-LC	The standard epidermal model with the additional incorporation of Langerhans cells (LCs)	Skin Immune response, UV exposure, Bacterial adhesion, Omics, and Permeability
	SkinEthic™ RHPE	The standard epidermal model cultivated in the presence of different melanocytes corresponding to 3 different phototypes of human skin, namely, Phototype II (Light), IV (Tanned) or VI (Brown)	Pigmentation, Depigmentation, Omics, and UV exposure
MatTek Life Sciences	EpiDerm FT™	A full-thickness skin model cultured from normal, human fibroblasts (NHFB) and NHEK at the air-liquid interface in tissue culture inserts to form a multilayered model of the human dermis and epidermis	Anti-Aging, Wound healing, Skin hydration, and UV protection efficacy of compounds/formulations
	MelanoDerm™	A differentiated 3D co-culture of Keratinocytes and melanocytes from different ethnicities	Skin Lightening and Pigmentation studies
	Psoriasis	The diseased tissue model consists of healthy human keratinocytes and psoriatic fibroblasts harvested from psoriatic lesions	Anti-Psoriasis drug screening, Psoriasis disease research
	Phenion™	A full-thickness human skin model	Skin Physiology, Transdermal drug delivery, Skin penetration, Mode of action of active agents, Toxicology Assessment, Wound healing, and UV/IR radiation effects

Phenion	Phenion FT AGED Skin Model	A full-thickness human skin model characterized by connective tissue with senescent fibroblasts, reduced synthesis of ECM proteins like collagen and elastin, and elevated MMP secretion	Study basic biology of skin ageing mechanism and to develop formulations which can delay/counteract ageing
Cell Systems	epiCS®-FT	A full-thickness human skin model launched in 2017	
	epiCS-M	An *In vitro* reconstructed human epidermis consisting of primary epidermal keratinocytes and melanocytes from three different donor types	Skin tanning, Skin bleaching, and UV protection
	StrataTest®-FT	A full-thickness human skin equivalent (HSE) where a near-diploid human keratinocyte cell line, NIKS, was utilized	
	StratiCELL®		
LabSkin	Labskin	A full-thickness human skin equivalent which can be colonised with the skin microflora to provide a life-like platform	Basic skin research, structural, metabolic and physiological studies, Microbial colonisation, Gene and Protein expression, Penetration and delivery, and Pre-clinical screening
Fraunhofer Institute for Laser Technology	ArtiVasc 3D	An artificially vascularized 3-layered (Fat, epidermis, and dermis) skin model for 3D tissue regeneration	Pharmaceutical, cosmetics, and chemicals substance testing *in vitro*, and *in vivo* model for skin replacement
Creative Bioarray	FTSK-HSM	A full-thickness skin model equivalent to the human skin composed of human skin fibroblast in a collagen matrix and human	Skin irritation, Skin sensitization, Stress/Inflammation, Anti-aging, UV protection, Skin

		keratinocytes seeded on top to form the epidermis	barrier function and moisturizing
	Neurodermatology cell model	This model generated by co-culturing sensory neurons with keratinocytes and melanocytes with keratinocytes	Pigmentation, Photo-aging, Skin aging, Inflammatory skin disorder, Microcirculation, Warming sensation, and Hair growth
	Psoriasis skin model		Psoriasis
	Pigmented skin model	Human Keratinocytes + Melanocytes with three different phenotypes (II, IV, and VI)	Pigmentation disorder, Skin pigmentation, and Skin aging
GenoSkin	InflammaSkin®	The only ex vivo skin inflammation model developed using human T-cells with a psoriasis-like phenotype	To study the efficiency of anti-inflammatory drugs that can target T-cells, IL-17, IL-22and TNF-α
Epistem®	*In vitro* Psoriasis model	The human keratinocytes are stimulated with different pro-inflammatory cytokines to induce psoriasis	Gene expression and protein expression is studied using this model
	3D Human Living Skin Equivalent model	This model is developed within a collagen gel using freshly isolated human keratinocyte and fibroblast cells at the air-liquid interface for up to 0 days	WST-1 assay for cytotoxicity screening, Protein expression, Gene expression including anti-aging and anti-oxidant pathways, UV damage marker quantification and histometric analysis

Collagen-based skin models

Collagen is the most abundant ECM protein in the skin and has been used historically for skin tissue engineering. Collagen in human tissue are highly organized and provide structural support and flexibility to the tissue. In 1998, Black et al. reported capillary-like tubular structures in chitosan-linked collagen-glycosaminoglycan sponge skin models.[77] A combination of HUVECs and dermal fibroblasts

were seeded and cultured under media submersion. Keratinocytes were later added to create the epidermal layer. The models were then shifted to an air-liquid interface (ALI). It was observed that no additional factors were necessary for angiogenesis due to secreted ECM and growth factors from fibroblasts and keratinocytes. [77] Hudon et al. went on to further analyse these VHSMs, examining the influence of angiogenic and angiostatic molecules.[78] They reported that the capillary-like tubes were modulated by the addition of angiogenic factors, demonstrated by the increased number of capillary tubes and observed a reduction in vessels after the addition of an angiostatin factor. [78] These observations made it evident that the collagen-glycosaminoglycan models could be utilized as *in-vitro* platform for the screening of angiogenic compounds or drugs.[78]

In order to facilitate vessel formation, researchers in the past have utilized genetically modified cells that overexpress angiogenic factors and assembled them with collagen-based hydrogels to form vHSMs. For instance, Supp et al. utilized genetically modified keratinocytes that overexpress VEGF to fabricate a full thickness vascularized skin model.[79] The models with the VEGF expressing Keratinocytes showed better vascularization and attachment to wound bed after grafting as compared to models with normal keratinocytes.[79] Following this, Supp et al. fabricated endothelialized collagen-glycosaminoglycan skin substitute by the mixture of human dermal endothelial cells (HDMEC), fibroblasts and keratinocytes derived from a single autologous biopsy sample. At day 3, the model was exposed to an ALI and cultured for 15 days. After implantation in mice, the skin models with HDMEC showed the ability deposit basement membrane proteins and form vascular analogs. However, the limitation of these VHSMs was the detection of low number of HDMEC at the end of culture period.[80]

Tremblay et al. used collagen/ glycosaminoglycan/ chitosan sponge along with fibroblasts and HUVECs as the dermal compartment to fabricate vascularized skin models and observed capillary-like tubes within their model before grafting it unto mice.[81] In less than 4 days post-transplantation, red blood cells (RBCs) in the capillary-like structures of the fabricated skin models were observed. The presence of RBCs in graft vasculature demonstrates the anastomosis of vessels from the host tissue and the graft. It was observed that a non-epithelialized skin model required at least 14 days in order to achieve similar results. Auxefans et al. constructed vHSMs using the common method of seeding endothelial cells and fibroblasts together on a scaffold and later adding keratinocytes on the top. [82] Collagen-glycosaminoglycan-chitosan was used as the base scaffold. The novelty to their approach came from the use of adipose derived stem cells. Both progenitor and pre-differentiated cells were tested, and only the pre-differentiated endothelial cells appeared successful. When endothelial cells and fibroblasts were seeded together, the equivalent displayed capillary-like structures.[82] Similarly, Hansbrough et al. fabricated 3D collagen-Glycosaminoglycan models for burn wound closure. The collagen-Glycosaminoglycan served as a substrate where cells from the underlying wound bed migrated and provided essential factors for the survival of keratinocytes.[83]

The type of ECs (HUVECS or HDMECs), collagen type and culture condition affect the vascularization in collagen vHSMs. Ponec et al. utilized three different methods to fabricate the rat-tail collagen-1 based vascularized dermal compartment namely 1) collagen overlay method 2) collagen sandwich method and 3) collagen matrix method.[84] In method 1, HDMEC/fibroblast co-culture was seeded on top of the culture dish followed by the addition of collagen solution. In method 2, cells were seeded on top of a collagen gel followed by the addition of a collagen solution on top of the cells. In method 3, cells were mixed with a collagen solution and directly seeded on the culture surface. A mixture of keratinocytes and melanocytes were then added on top of the dermal compartments. In all the three dermal constructs, the HDMECs preferentially migrated laterally but not vertically. Furthermore, the culture of HDMECs/fibroblasts on the bottom of the trans-well filter and the addition of keratinocytes on top of the filter allowed for uniform tube formation. Fibroblast secreted ECM in the presence of keratinocytes that presented an angiogenic 3D milieu for uniform tube formation.[84]

The limitations of collagen-based skin models are their weak mechanical properties and the constriction of the gel due to traction forces generated by the encapsulated fibroblasts. In terms of the vascularization, collagen-based models have certain limitations such as 1) constriction of gels 2) time-dependant degradation of the hydrogel due to increased pro-angiogenic, and protease activity 3) inadequate or immature vascularization 4) regression of vessels due to susceptibility of collagen gels to proteases.[24] To overcome these limitations, hybrid mixture of collagen with other biomaterials is utilized by several researchers to construct the vHSMs.

Hyaluronic acid-based skin models

Hyaluronic acid is an abundant ECM present in the skin tissue. Hyaluronan in the skin is associated with the collagen and elastin fiber spacing and the structural integrity of the skin.[85] Tonello et al. fabricated dermal equivalent with blood vessels using a hyaluronic acid based scaffold, which comprised of HDMECs and fibroblasts. They reported that the production of ECM assisted in the proliferation and the organization of the endothelial cells into micro-capillary-like structures. Open lumen was observed after 21 days of culture.[86] Cerqueira et al. combined Gellan Gum-Hyaluronic Acid Spongy-like hydrogels with human adipose stem cells (hASCs) and human adipose microvascular endothelial cells (hAMECs) to fabricate vHSMs. The presence of hAMECs facilitated neo-vessel formation.[87] Tonello et al. improved upon their previously reported epithelialized dermal equivalent by the addition of keratinocytes to create an epidermal compartment. Using the hyaluronic based scaffold, they seeded dermal fibroblasts and seeded HDMECs and cultured for 10 days. Keratinocytes were seeded and after one week of cultured exposed to ALI for 21 days. Histology showed evidence of dermal and epidermal compartments as well as endothelial cells organized into rings similar to capillary structures with a lumen. They reported the production of two-layered skin construct with a micro-capillary network.[88]

Fibrin-based skin models

Fibrin is a natural and biodegradable scaffold that has a significant role in wound healing. Fibrin has several advantages over other hydrogels which are 1) tuning of gel properties such as porosity and stiffness and 2) superior wound healing properties 3) provides angiogenic 3D environment for vascular modification 4) limited foreign body reaction due to autologous nature, and 5) high mechanical properties.[89, 90]

Chen et al. fabricated fibrin-based tissues that were pre-vascularized. Fibrin was mixed with HUVECs and fibroblasts to construct the dermal compartment. After 7 days, the vascularized tissues were implanted in immune-deficient mice and collected at different time points. As early as day 5, RBCs were found in HUVECs-lined vessels. Post-implantation, tissues containing ECs showed a greater number of perfused lumens compared to controls. The pre-vascularization of the tissue was showed to significantly accelerate the time the tissue inoculates with host vasculature and further promote cellular activity indicative of tissue remodelling.[91] Chan et al. fabricated a skin model consisting of adipose stem cells that were isolated from discarded burn skin. The epithelial and hypodermal compartments were composed of collagen hydrogel whereas the vascularized dermal construct was a collagen PEGylated fibrin-based bi-layered hydrogel. The advantage of this hydrogel is that it doesn´t necessitate the pre-differentiation of the ASCs before seeding.[92] The PEGylated-fibrin environment allowed differentiation of ASCs to tubular networks that resembled the vascular phenotype, whereas the collagen layer allowed the ASCs to maintain its fibroblast-like phenotype. The collagenous hypodermal compartment was nourished with the adipogenic media triggering the differentiation of ASCs into adipocytes. Recently, Xue Liu, et al fabricated 3D printed fibrin-based VHSMs to mimic AD.[93] The dermal compartment was composed of fibroblasts, induced pluripotent stem cells (iPSC) ECs and pericytes. To stimulate the AD-like diseased phenotype, IL-4 was added to the culture media at the time of ALI. A decrease in Trans-epithelial electrical resistance (TEER) values in AD-models as compared to non-diseased models was observed and correlated with decreased epidermal barrier differentiation protein expression in the vascularized diseased models. The addition of IL-4 also upregulated the production of endothelial adhesion proteins VCAM-1 and ICAM-1.[93]

Scaffold free vHSMs

Although scaffold-based approaches to develop HSMs are valuable in the formation of skin models, scaffold-free HSMs are also generating traction. Conventionally, hydrogels or a porous scaffold would provide the 3D environment necessary for endothelial tube formation. Scaffold-free approaches exploit the cell´s ability to produce its own ECM. The advantages of scaffold-free methods include 1) low immune-rejection after grafting 2) physiological similarity to native skin tissue as compared to scaffold-based models (ref) 3) improved epidermal formation 4) improved vascularization 5) low batch-batch variability/high reproducibility. The techniques utilized by researchers to fabricate scaffold-free skin models are stacking of cell-sheets (CS), cell-coating technique, and decellularized scaffolds.[94, 95] The

CS technique involves the stacking of dermal sheets to form a thick tissue. Fibroblasts are cultivated media supplemented with ascorbic acid, which triggers the cells to rapidly produce ECM. The formed sheets are then extracted and stacked. Cell-coating and accumulation technique, on the other hand involves rapid construction of thick tissues by an accumulation of ECM-coated cells. The coated nano-layer of ECM allows cells to interact with one another and rapidly forms a 3D tissue.

Cerqueira et al. utilized the CS technology to fabricate vHSMs for wounds.[93] Dermal sheets composed of fibroblasts, keratinocytes and hDMECs were utilized to fabricate the VHSMs. The wound healing capability of the cell sheets composed of different cell types were analysed. After 21 days of transplantation, it was observed that sheets with 1) Fibroblasts, hDMECs and Keratinocytes and 2) Fibroblasts and Keratinocytes showed the highest wound closure percentage than control. ECs also led to neovascularization.[93] Recently, Bourland et al. fabricated a vascularized 3D melanoma model utilizing CS technology.[96] Melanoma tumor spheroids were integrated with the vascularized dermal sheet following which keratinocytes were added. The melanoma spheroid integrated, proliferated and migrated in the 3D model. There was an increased secretion of ANG-2 and CCL21 in vHSMs suggesting metabolically active ECs.[96]

Cell coating technique relies on layer-by-layer coating of ECM moieties on cell surface and assembling the coated cells to form 3D tissues. This technique is relatively faster than self-assembly technique and has been used in the past to fabricate various in-vitro tissues. Matsusaki et al. fabricated skin models with blood and lymph capillaries by using cell-coating technique.[95] Fibronectin and Gelatin-coated dermal fibroblast along with HUVECs and hLECs were utilized to fabricate the vHSMs. Miyazaki et al. utilized the same model to use as a functional engraftment.[97] The vHSM was implanted onto the excised wound in immuno-deficient mice. After 7 days of transplantation of the skin models without ECs, blood vessels were observed only in the periphery of the graft, whereas pre-vascularized models were fully perfused. Anastomosis between the graft vessels and the host vessel was observed on day 14 of transplantation. Contrary to hydrogel-based skin models, these vHSMs didn´t show graft contraction or shrinkage after transplantation. Furthermore, after 7 days of transplantation, non-vascularized models showed epidermolysis which was not observed in vHSMs.[97]

Researchers have also focused on using decellularized tissues for skin tissue engineering. The advantage of decellularized tissue is the intact scaffolding and intricate architecture that can be beneficial for vascularization. Schechner et al. utilized cadaveric acellular pieces of the dermis to create skin models. Keratinocytes were added on top of the decellularized dermis to create the epidermal compartment. A day before implantation in mice, HUVECs that were modified to express Bcl-2 endothelial survival gene were seeded on the reticular dermis or the bottom side of the skin equivalent. The vHSMs were sutured superficially on the excised skin of mice and demonstrated graft perfusion. The Bcl2 modification also appeared to promote perfusion and maturation of the vasculature.[98] Sahota et al. used

acellular donor dermis and seeded dermal fibroblasts and HDMECs on the reticular surface towards the top. After twenty-four hours the dermis was flipped over leaving the reticular surface to the bottom and the papillary dermis on top, allowing the exposed surface to be seeded with primary epidermal keratinocytes. The skin equivalent was autologous as all the cells were from the same patients.[99]

Implantation of skin graft with human ECs can lead to immunological complications. Alternative ECs sources include EC derived from the recipient or by utilizing ECs from circulating endothelial progenitor cells (EPC). Shepherd et al. compared Bcl2-transduced and non-transduced HUVECs with endothelial cells derived from umbilical cord blood (CB-EC) and from peripheral adult blood (AB-EC).[100] The skin models with CB-EC, AB-EC and Bcl2-transduced HUVECs showed robust vessel formation within the decellularized scaffold and were also able to promote host vascularization within the implanted graft as compared to non-transduced HUVECs which stimulated slow host vascularization within the graft. The study, highlighted the application of alternate ECs source for the vascularization of skin grafts.[100]

2.4. The current trends in vHSMs

Cultivation of VHSMs in a dynamic environment

Emerging technologies such as 3D bioprinting allows the fabrication of durable and thick viable tissues.[101] Currently, 3D printing technologies, sacrificial scaffolds and microfluidic methods have enabled the fabrication of perfusable in-vitro vHSMs. Vessel perfusion allows the 1) transport of essential growth factors and nutrients to individual cells 2) study of circulating cancer cells or immune cells into the skin tissue. 3) Observation of drug absorption into the blood vessels 3) Understanding of the transport of intra-venous drugs/nanoparticles/nanogels into the skin tissue 4) construct thick viable skin models.

Mori et al fabricated collagen-based skin models with perfusable vasculature [102]. Here, a 3D printed bioreactor with anchoring connectors was manufactured and nylon wires were fixed across the printed device. Collagen with human dermal fibroblast was then assembled in the reactor followed by the extraction of nylon wires post-collagen gel solidification. Hollow openings formed due to the removal of nylon wires in the dermal compartment were then filled with endothelial cells **(Figure 2.3 B, C)**. The perfused skin equivalent showed a higher cell density compared to non-perfused models as well as showed promising results in predicting vascular absorption.

Abaci et al. utilized iPSC-derived ECs to fabricate a perfusable skin model.[103] A micro-pattern of sacrificial alginate gel was prepared on 3D printed molds. Collagen gel containing dermal fibroblasts was then added on top of the patterned vasculature. After polymerization around the channels, keratinocytes are seeded on top of the matrix and cultured under submerged conditions and exposed to ALI for 7 days **(Figure 2.3A)**. The sacrificial alginate was treated with sodium citrate to dissolve the

alginate followed by addition of iPSC-derived EC. In a recent study, Kim et al. fabricated a fully perfusable skin model comprising of hypodermis, dermis and epidermis compartment. The hypodermis and dermis bio-ink were composed of adipose-derived dermal-ECM and skin-derived dermal-ECM together with bovine fibrinogen respectively. Gelatin hydrogel was used for the fabrication of vascular channels in the skin model.[104] Helmedag et al. used a fibrin-based scaffold to fabricate vHSMs.[105] The fibrin gel and the fibroblast allowed for rapid vascularization of the tissue. The vHSMs were cultivated on a 3D printed bioreactor and under the flow perfusion culture. The study showed the effect of flow rate on for fibrin based vHSMs.

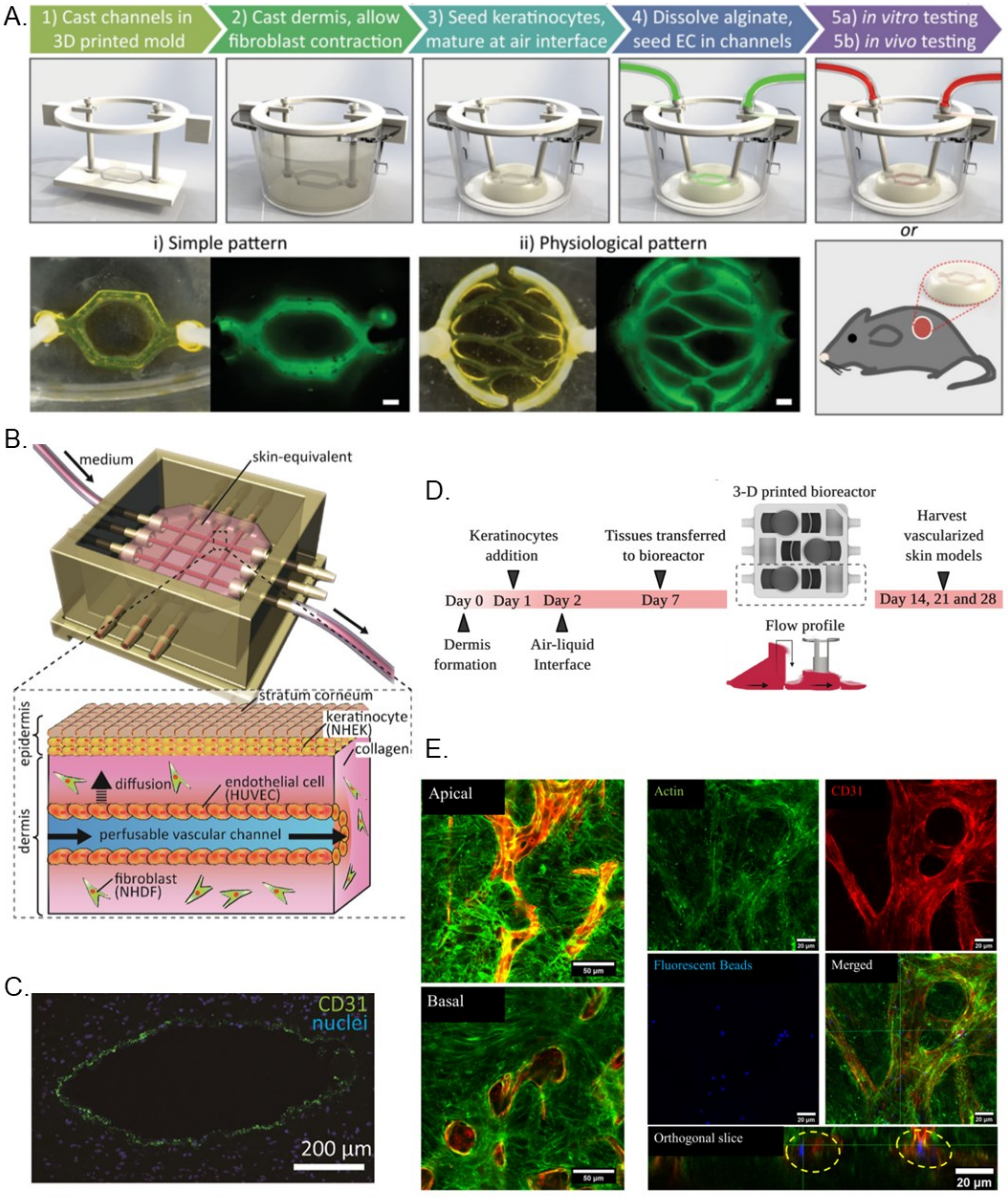

Figure 2.3. *shows skin models cultured in dynamic flow environment. A) Patterned vasculature fabricated within 3D printed mold. B, C) Formation of large vessels within the dermal compartment by creating microchannels. D, E) Formation of perfusable sites on the basal compartment of the skin due to continuous media flow. Reproduced with permission from*[1, 102, 103]

Increase in the flow rate was associated with decreased vascular branching and vessel length. Jusoh et al. described a microfluidic device where a fibrin-based vascularized skin model was constructed.[106] The device comprised of a several compartments separated with micro-posts that included a fibrin compartment comprising of human dermal fibroblast, a 2D keratinocyte compartment and EC compartment. Stimulated growth factors from the Keratinocytes led to the migration of vessels towards the keratinocytes and the micro-posts aided in the formation of endothelial lumen. The vHSMs were used for skin irritation testing. Chemical irritants such as sodium lauryl sulfate (SLS) and steartrimonium chloride (SC) were tested on keratinocytes and their effect on vascularization was observed. The increase in sprout length, vessel proliferation and lumen formation with SLS and SC addition showed the potential of such models as a platform for skin irritation testing.

Groeber et al. utilized a biological vascularized scaffold take from a segment of the jejunum as a vascularized bed. After de-cellularization, the scaffold was placed in a bioreactor.[107] Human microvascular endothelial cells would line the walls of the vessels which can be perfused with physiological volume. Dermal fibroblasts were added to the surface of the vessels which are connected in fluidic system in turn the surface and bottom of the model are also connected to fluidic system that can provide media.[107] Another study from the same group fabricated perfusable vHSMs to study skin fibrosis.[108] TGF-β was added to induce the fibrosis process. Furthermore, anti-fibrosis drug Nintedanib was tested on the vHSMs. Nintedanib reduces TGF-β induced ECM production and fibroblast to myofibroblast transition.[108]

In our recent study, 3D printed bioreactors were utilized to cultivate scaffold-free. It was shown that flow culture prevented degradation of the vascularized dermal compartment and allowed for the maintenance of long-term vascular integrity. Perfusable sites spanning the basal compartment of the skin was visible (**Figure 2.3E)**. This was attributed to alterations in angiogenic growth factors, proteinases and inhibitors of proteinases between flow-treated and static models. Furthermore, it was demonstrated that flow culture led to faster wound healing in laser-irradiated VHSMs as compared to static models, thereby emphasizing on the need of dynamic perfusion of tissue models for disease modelling.[1]

Multi-cellular vHSMs

Skin consists of numerous cell types that continually cooperate with one another to maintain homeostasis. The future of a physiologically relevant skin models would be the one that includes diverse cell types such as neurons, lymphatic vessels, immune cells and skin appendages. The additional cell types influence the vasculature via cell-cell contact or by release of essential angiogenic growth factors. As the inclusion of these cells in skin models become more widespread, the requisite for vascularization becomes more apparent. The presence of vascularization not only nourishes the different cell types, but also secretes and responds to growth factors and cytokines. Therefore, there will be a demand of vHSMs

(both healthy and diseased) as biological templates, where other ancillary cell types will be supplemented.

In a recent article, Baltazar et al. fabricated a 3D-printed full thickness skin model comprising of endothelial cells and pericytes.[109] The addition of pericytes allowed stable vascularization for a long-frame. The printed models were implanted in an immune-deficient mice and vessel perfusion was observed. Furthermore, Pericytes allowed for better Keratinocytes differentiation and maturation. Marino et al fabricated both collagen and fibrin skin models comprising of vascular and lymphatic capillaries.[110] Both hDMECs and hLECs formed intricate networks spanning the entire tissue construct. Transplantation studies showed anastomosis of lymphatic vessels between the skin models and the host.

Kreimendahl et al. fabricated a fibrin-based vHSMs with macrophages.[111] Wound healing experiments elucidated the interplay between vasculature and macrophages. Laser treated samples in the presence of macrophages showed significantly higher vascularization as compared to laser treated skin models without macrophages. The presence of macrophages also led to faster wound healing after laser treatment. Furthermore, the detection of macrophage specific markers CD14 and CD163 after infliction of wound points out to the transformation of quiescent macrophage phenotype to activated phenotype (M2-macrophages) which has implication in angiogenesis and wound healing.[111] Kwak et al. engineered a skin model in a microfluidic chip comprising of vascularization and immune cells to study immunological response.[112] HUVECs were cultured on the bottom of a porous PDMS membrane and exposed to the fluidic compartment, whereas the upper compartment comprised of the collagen-based dermis and the epidermis. Furthermore, toxicity tests were conducted with the addition of doxorubicin. It was observed that the presence of HUVECs in the model resulted in higher viability of dermal fibroblast in the presence of the drug. To recapitulate immune response in the skin, the models exposed to UV irradiation followed by addition of Leukocytes to the fluidic compartment. UV irradiation resulted in higher recruitment of leukocytes that migrated from the fluidic compartment, through the HUVECs monolayer and into the dermal compartment.[112]

Personalized skin models

The concept of treating patients as an individual rather than a part of a large patient population could be the next step to treat specific skin diseases more effectively. Personalized skin models could be fabricated by cells extracted from 1) skin patches followed by sub-culture of individual cells (immune cells, keratinocytes, fibroblasts, ECs) and formation of HSMs or 2) iPSCs that could be differentiated into different cell lineages and subsequently be used to fabricate HSMs. Few studies have already fabricated functional HSMs from patient-derived iPSC differentiated into keratinocytes and fibroblasts.[113]

In a recent article, Girardeau-Hubert et al. demonstrated that the skin models created from cells derived from different ethnic sources leads to altered epidermal fate.[114] It was observed that collagen-based HSMs from African skin consists of more number of proliferating basal keratinocytes and lower FLG levels in terminally differentiated epidermis layers as compared to HSMs from Caucasian sources. Furthermore, several genes extracted from the HSMs pertaining to lipid/ceramide metabolism, FLG processing and epidermal differentiation differed significantly between the two groups.[114] Genetic characteristics could therefore be one of many criteria to define the efficacy of drugs and cosmetics both in treatment of the ailment as well as safety/side effects of the drug. The fabrication of patient-derived personalised VHSMs could in the future, be essential in eradicating skin diseases.

Cultivation of multiple organs

A multi organ-on-a-chip would allow for understanding the interaction between different organs and skin diseases. Numerous skin diseases are linked to other more critical diseases in distant organs. For instance, such hybrid systems would elucidate the link between psoriasis and psoriatic arthritis, AD and cardiovascular risk and melanoma metastasis to other organs. In order to fabricate the multi-organ chip, vascularization of individual in-vitro organ would be an important step. A vascularized multi organ-on-a–chip would allow better understanding of tropical or injected drug absorption, penetration, transport and efficacy in patients. Preliminary work on multi organ-on-a-chip has been explored by several research groups. Wagner et al. constructed a multi-organ chip system comprising of 3D skin model and human liver model.[115] Skin biopsies and Liver spheroids were integrated in the chip and a continuous flow of media was applied. The cross-talk between the liver tissue and the skin was showed by the consumption of liver-released albumin by the skin tissue. Troglitazone was tested on the system and revealed dose dependent sensitivity to the drug.[115] Similarly, Maschmeyer, in 2015, fabricated an organ-on-a-chip platform comprising of interconnected human kidney, skin, liver and intestine models.[116] The skin, however, was acquired from prepuce samples from which biopsies of required diameter was excised and integrated into the chip. The individual models showed high tissue viability and architecture during the 28-day culture period.[116] Similar studies have utilized the skin-integrated multi organ-on-a-chip to mimic the complex interactions of individual organs in the human body.[116] The future could entail multiple vascularized organs including vHSMs integrated in a single organ-on-a-chip and provide a platform for fast and efficient drug testing.

Conclusion

The recent ban on cosmetic animal testing has sparked the interest of the tissue engineering community to fabricate more clinically-relevant in vitro skin models. Animal models are still an indispensable tool in preclinical drug testing. This is due to the lack of complex, high-throughput, multi-organ human-based models. Vascularization is an essential step to fabricate organ-like tissues that can, in future, drastically reduce animal experimentation, and completely replace 2D models. The future entails the

testing of drugs and cosmetics on personalized models comprising an assembly of multiple patient-derived, vascularized tissues. VHSMs—owing to the progress of novel angiogenic biomaterials as well as advancements in scaffold-free techniques, perfusion culture bioreactors, 3D printing, and organ-on-a-chip systems—are a promising platform for future dermatological research.

Chapter 3

Clinically-relevant human skin equivalent for psoriasis

This chapter was adapted with permission from the publication "Long-Term and Clinically Relevant Full-Thickness Human Skin Equivalent for Psoriasis" in *ACS Applied Bio Materials.* 2020 Sep 3; 3(10):6639-47.
Direct link: https://pubs.acs.org/doi/10.1021/acsabm.0c00202. All schematics were created using Biorender.

3.1. Introduction

Psoriasis is a chronic immune-mediated inflammatory disorder mainly affecting the skin of 2–3% of the general population.[117] Histologically, it is characterized by raised, well-demarcated, erythematous oval plaques. Psoriatic plaques are characterized by an abnormal proliferation and differentiation of keratinocytes leading to epidermal hyperplasia and results in the reduction or complete absence of the epidermal granular layer. This causes incomplete cornification of the keratinocytes with retention of nuclei (parakeratosis) in the *stratum corneum*. On the other hand, compared to the normal skin mitotic rate of the basal keratinocytes is increased. This gives rise to a thickened epidermis.[118] Since, in psoriasis, premature cell death is combined with accelerated keratinization, late differentiation markers of keratinocytes such as pro-FLG and loricrin are downregulated. Moreover, keratinocyte differentiation markers such as keratin (K)1 and 10 are reduced while an increase in expression of proteins KALP/elafin, K6, K16, and K17 which are absent in healthy skin are expressed. Pathologically, immune cells infiltrate the dermis and epidermis of the psoriatic lesion. This involves the innate and adaptive immune systems, where dendritic cells (DCs), and T cells, among other cells, play a major role.[118, 119] Due to the presence of CD4+ T_h1 and CD8+ cytotoxic T cells type 1 (Tc1), TNF-α, high levels of interferon (IFN)-γ and IL-12 in psoriatic lesions, initially psoriasis was considered to be a T helper cell type1 (T_h1) cell-mediated disease. 'Type 1' inflammatory environment is created by the interaction of T cells with DCs subsequently releasing T_h1 type cytokines. Lately, added role of T_h17 cells and their main effector cytokines IL-17A, IL-17F, IL-21, and IL-22, as well as granulocyte-macrophage colony-stimulating factor (GM-CSF) [120-122] has been demonstrated in the pathogenesis of psoriasis.[123] In addition, reports also show the involvement of T_h22 cells in the pathogenesis of psoriasis due to their ample secretion of pro-inflammatory IL-22.[124]

Beyond affecting the skin, psoriasis exposes the patient to an increased risk of many other diseases like psoriatic arthritis, metabolic syndrome, autoimmune conditions, cardiovascular disease, malignancies, and psychiatric disorders.[125-127] Thus, psoriasis is a complex and multifactorial disease involving

multiple interactions between different cell types and impacts on virtually all aspects of health. Despite the challenges put forward by this debilitating disease, its immune pathogenesis still lacks complete understanding. Therefore, a better understanding of the mechanisms of psoriasis is required so that new therapeutic agents can be developed for better patient outcomes. Over the years many *in vitro* models of psoriasis are developed to study the pathogenesis of psoriasis and to explore for new therapeutic drug candidates.[128-131] Currently, the cytokine stimulation approach to develop disease pathogenesis is mainly applied to collagen-based full thickness skin models. In the collagen models, fibroblasts are embedded in collagen I gels which function as dermal equivalents.[120] Collagen models can demonstrate characteristic psoriatic phenotype like epidermal hyperplasia and hypo-granulosis and express the typical disease marker like HBD-2, SKALP/elafin and/or S100A7 [120, 132] but these models suffer from poor mechanical strength, contraction and a limited life span.[133] Typically, these full thickness skin models start to degrade after approximately fourteen days. One of the main causes of the limited life span of these models is the upregulation of collagenase, which deteriorates the existing extracellular matrix (ECM).[134] After stimulation with a disease-specific cytokine cocktail, it generally takes at least five days for the development of the disease phenotype like psoriasis.[120, 135] Thus, the relatively short life of the current skin models does not allow testing the treatment/therapy after full development of the disease, thereby failing in mimicking the realistic clinical scenario.

To replicate the clinical drug testing condition on skin models the study can be divided into three phases. Phase I: development of the model, Phase II: development of characteristic disease phenotype and Phase III: start of the treatment protocol **(Figure 3.1)**. Due to the short longevity of the existing models, mostly Phase II and III are combined, which minimizes the duration between actual disease onset and treatment. Eventually, this can give rise to testing results, which do not correlate to the clinical situation. Hence, it is imperative to develop skin models that are viable for long-term treatment. Such models can better mimic clinical situations of diseases such as psoriasis and atopic dermatitis and will enable a time-course study during treatment, equivalent to sequential biopsies. Due to ethical reasons it is not possible to derive sequential biopsies form patients in clinical studies since biopsies involve the risk of anaphylactic reaction to local anesthesia and always lead to scaring, sometimes even hypertrophic scars or keloids. Therefore, most psoriasis studies often only monitor the clinical condition of the patient (Psoriasis Area and Severity Index (PASI) score) and analyze blood samples derived at every patient visit.

Long-term skin models would further assist the development of more complex models with incorporated immune cells and vascularization. A long-term organotypic skin that can accurately model the diseased tissue architecture, with the added potential of the introduction of multiple cell types, however, has not been previously reported.

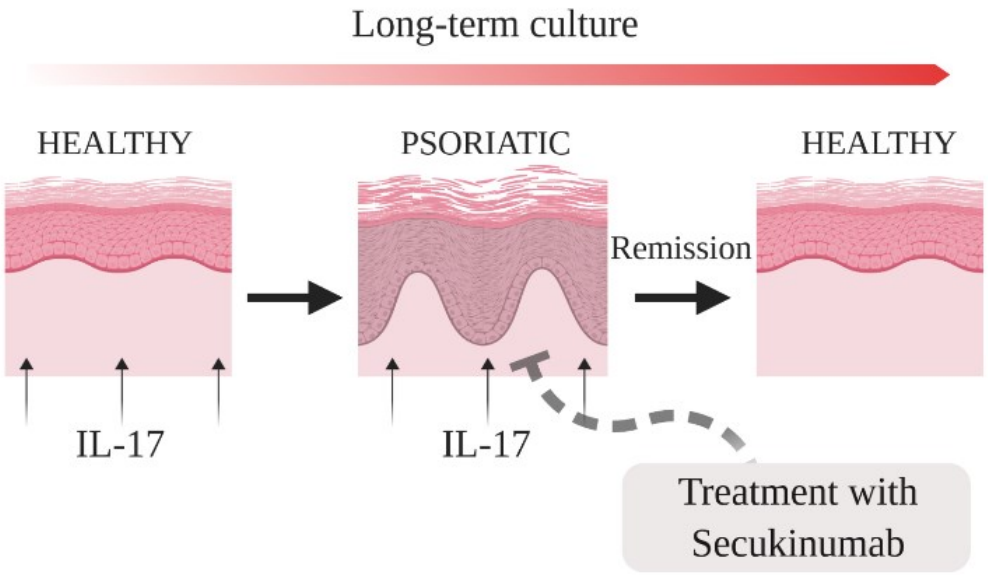

Figure 3.1. *shows the experimental overview. The long-term experimental protocol involves fabrication of scaffold-free skin models, stimulating the healthy models with IL-17 to induce psoriasis-like state, treatment with anti-Il17 antibody Secukinumab, and observing the remission of the disease models to healthy phenotype after treatment.*

Different from the approaches used so far, this approach of making a full thickness skin model is neither based on scaffolds or hydrogels but instead on the targeted physical modification of cells. In this approach, seeded single cells carry a minimum ECM nano-coating to generate tissue. The approach is based on recent reports by Akashi and Matsusaki[94]who have shown that primary human cells (fibroblast, endothelial, epithelial cells) equipped with layer by layer nano-coating of fibronectin and collagen can (i) spontaneously form 3D tissue and (ii) can be cultivated in hetero cell cultures. This concept has led to entirely new and extremely promising hetero-cell tissue models in which contacts between different cell types can direct the differentiation from an unstructured cell assembly to an organized and functional micro-tissue. However, the capability of this technique for long-term skin models has not been explored and such models have never been used to study disease progression and remission. In this chapter the benefits of a long term HSE was demonstrated to investigate the role of the inflammatory cytokine IL-17A in the pathogenesis of psoriasis and the molecular effects of systemic targeted treatment with Secukinumab.

3.2. Materials and Methods

Materials

Isolation of human epithelial keratinocytes and dermal fibroblasts- Normal human epithelial keratinocytes (NHEK) and normal human dermal fibroblasts (NHDF) were isolated and cultured as previously described.[136] NHEKs and NHDFs were obtained from foreskin or specimens from cutaneous surgery in healthy subjects, after informed consent and according to the institutional

guidelines and the Declaration of Helsinki principles. The ethics committee of the University Hospital, RWTH Aachen, Germany, approved this study.

3D human skin equivalents

Individual fibroblast cells were ECM-coated with Fibronectin(FN) and Gelatin(G) as previously described.[94] Briefly, dermal fibroblasts were trypsinized, centrifuged, and washed with PBS and mixed with 0.04 µg/ml FN and 0.04 µg/ml G with intermediate PBS washing step. After each mixing step, the cells were centrifuged for 1 minute at 400g. A total of 9 coating steps were performed. Coated fibroblasts were then seeded inside 0.4µm pore-sized 6.5mm trans-well inserts. A total of 1.5×10^6 and 0.5×10^6coated NHDFs was used for 15 layers and 5 layers of dermis respectively. The NHDFs were used from Passage 4-9. The formed dermis was incubated for 24 hours (37ºC, 5% CO_2) with DMEM, 1% penstrep, FBS 5% before the addition of human Keratinocytes. The next day, 1.8×10^5 Keratinocytes in 300µl of keratinocyte media (Derma Life K Serum-Free Keratinocyte Culture Medium) were seeded on top of the formed dermis layer. The lower compartment of the trans-well was filled with 1mL media. The construct was incubated for 2 hours at 37°C and 5% CO_2 to allow optimal attachment of Keratinocytes to the dermal compartment. After the incubation time, the media from the outer and inner part of the trans-well inserts was extracted and 2.3 ml of fresh growth media (Dermalife K Serum-free Keratinocytes medium: DMEM (50:50), 0.5% penstrep and FBS 5%) was added. The models were incubated for 24 hours. The next day, media from the well plate was extracted and the outer compartment of the trans-well was filled with 1 ml of differentiation-media (Dermalife without TGF alpha: DMEM (50:50), FBS 5%, 0.5% penstrep, $CaCl_2$ 1mM and 50µg/ml ascorbic acid) whereas no media was added on the inner compartment. The models were cultured in ALI for 7 weeks with media changes every alternate day.

Psoriasis-like skin conditions were generated by adding rhIL-17A (50 ng/ml, Peprotech) to the basolateral compartment when models were lifted to the air-liquid interface. 3D models were stimulated for a total of 19 days. To assess the impact of secukinumab, 3D models were concurrently treated with secukinumab (6µg/mL in dimethylsulphoxide (DMSO) and rhIL-17A (50 ng/mL)). 3D skin cultures were harvested 19 days after stimulation with the cytokine and rhIL17A with or without pretreatment of 5 days with rhIL17A. The culture medium was changed and stimulation was repeated every other day. To ensure reproducible results, all experiments were performed in triplicate.

Collagen-based HSE

Collagen based full-thickness 3D skin equivalents were constructed as described previously.[137] In brief, to establish the dermal part of the skin equivalents ice-cold bovine collagen I solution (Vitrogen, Cohesion Technologies, Palo Alto, CA, USA) and 10× concentrated Hank's balanced salt solution (Gibco/Invitrogen, Darmstadt, Germany) were mixed in 8:1 by volume ratio. This was neutralization with 1 M NaOH, followed by addition of one volume of fetal calf serum (FCS) containing 1×10^6

NHDFs. Four millilitres of this solution (4×10^5 cells) were seeded into polycarbonate cell culture inserts for 6 well plate (3 µm pore size, Nunc; Thermo Fisher Scientific, Langenselbold, Germany). The dermal equivalent was seeded with 1×10^6 NHEKs after 2 days and submerged in equal volumes of DMEM and Keratinocyte growth medium (Dermalife K Serum-free Keratinocytes medium) with 5% FCS, 50 µg ascorbic acid, and 5 µg/mL aprotinin (Applichem, Chicago, IL, USA). On day 3 the HSEs were lifted to the air-liquid interface.

RNA isolation

Total RNA was isolated from psoriasis-like 3D skin models. Whole tissue was lyzed with a tissue lyzer II (Quiagen) in lysis buffer of Nucleospin RNA Kit (Macherey-Nagel, Duren, Germany), according to the manufacturer's instructions. The quantity of the RNA was measured (NanoDrop Technologies, Wilmington, DE, USA), and the integrity was confirmed (Agilent 2100 Bioanalyzer; Agilent Technologies, Palo Alto, CA, USA).

Quantitative real-time PCR

Purified RNA was reverse transcribed into cDNA using the SuperScript VILO Mastermix (Life Technologies, Langenselbold, Germany), according to the manufacturer's instructions. Quantitative real-time (qRT) PCR analyses were performed on an ABI Prism 7300 Sequence Detection System (Applied Biosystems, Weiterstadt, Germany) using Assays-on-Demand gene expression products (Applied Biosystems) for human CCL8 (HS00271615_m1), CCL20 (HS01011368_m1), CXCL1 (HS00236937_m1), CXCL5 (HS00171085_m1), CXCL6 (HS00605742_g1), CXCL17 (HS01650998_m1), CRNN (HS00211833_m1), FLG (HS00856927_g1), DSC1 (HS00245189_m1), DSG1 (HS00355084_m1), DSG4 (HS01125472_m1), IL-1beta (HS00174097_m1), IL6 (HS00985641_m1), IL18 (HS01038788_m1), IL24 (HS01114274_m1), IL-33 (HS01125943_m1), IL-36alpha (HS00205367_m1), IL-36beta (HS00758166_m1), IL-36gamma (HS00219742_m1), IL36RN (HS00202179_m1), IGFL-2 (HS03645208_m1), KRT1 (HS01549614_g1), KRT10 (HS00166289_m1) according to the manufacturer's recommendations. An Assays-on-Demand product for HPRT (Hs99999909_m1) was used as an internal standard.

Microarray analysis

For microarray analysis, purified mRNA was amplified, labeled and hybridized to Human Clariom S Array, according to the manufacturer's instructions as previously described.[136] Data were analyzed using GeneSpring GX 14.9 software (Agilent Technologies, Frankfurt am Main, Germany). Gene ontology enrichment analysis was performed using http://www.geneontology.org/.

Light microscopy, immunofluorescence and immunohistochemistry

The tissues were either fixed in 10% formalin for paraffin embedding or embedded in Tissue Tek O.C.T.for cryosections. For light microscopy, 4µm paraffin sections of 3D models were stained with hematoxylin and eosin (H&E). For immunohistochemistry paraffin-embedded tissue was cut into 4-µm sections, mounted on Superfrost slides (Menzel, Braunschweig, Germany), deparaffinized and rehydrated. To unmask antigens, the specimens were treated with 'Target Retrieval Solution Citrate pH

6.0, (Dako) according to the manufacturer's instructions and rinsed in distilled water. Specimens were incubated for 60 min with primary mouse anti human monoclonal antibodies: FLG (clone AKH1, 1:100; Santa Cruz Biotech, Santa Cruz, USA). Cytokeratin 10 (1:500, Ki67, 1:50, Collagen IV, 1:50; Dako Glostrup, Denmark); Integrin ß4 (1:200; Abcam, Cambridge, UK); Vimentin (1:200; Sigma Aldrich, Missouri, USA). Binding of the antibodies was visualized by the Dako 'Real Detection System Alkaline Phosphatase/RED' on the Universal Staining System (Dako) as specified by the manufacturer. Finally, specimens were counterstained with haematoxylin and mounted with coverslips. For immunofluorescence, 4-µm cryo-sections were fixed in acetone and incubated for 1 h with primary antibodies as described above. Goat anti-mouse IgG Alexa Fluor 488-conjugated secondary antibody (Molecular Probes, Eugene, OR, USA) was added for epifluorescence detection using the Leica DM IL photomicroscope (Leica Microsystems, Wetzlar, Germany) with digital photo documentation (DISKUS; Hilgers, Konigswinter, Germany). The illustrations used in the publication were created with BioRender.com

3.3. Results and Discussion

To prepare the HSEs, normal human epithelial keratinocytes (NHEK) and normal human dermal fibroblasts (NHDF) were obtained from specimens of cutaneous surgery in healthy volunteers, after informed consent and according to the institutional guidelines and the Declaration of Helsinki principles. The models were prepared using layer by layer coating and accumulation approach. This process is based on preconditioning of cells by ECM proteins thereby, recapitulating the cell adhesive properties of ECM surrounding cell microenvironment. For fabrication of the models, NHDFs were coated with nanometer thick fibronectin-gelatin (FN-G) films. The films were coated on the surface of a single cell in a layer by layer process $(FN\text{-}G)_8$-FN. After coating, cells were allowed to assemble to form a 3D tissue by cell accumulation in a confined space. This adhesion of the matrix to the cells and itself is solely by integrin binding and protein-protein interaction, equivalent to those present in the natural ECM. For fabrication of the HSEs, 15 layers of coated fibroblasts were assembled on day 1 to form dermis. This was followed by the addition of a monolayer of keratinocytes on day 2. The HSE was introduced to the air-liquid interface (ALI) on day 3 and cultured up to 7 weeks. Histological examination of the HSEs was conducted every week.

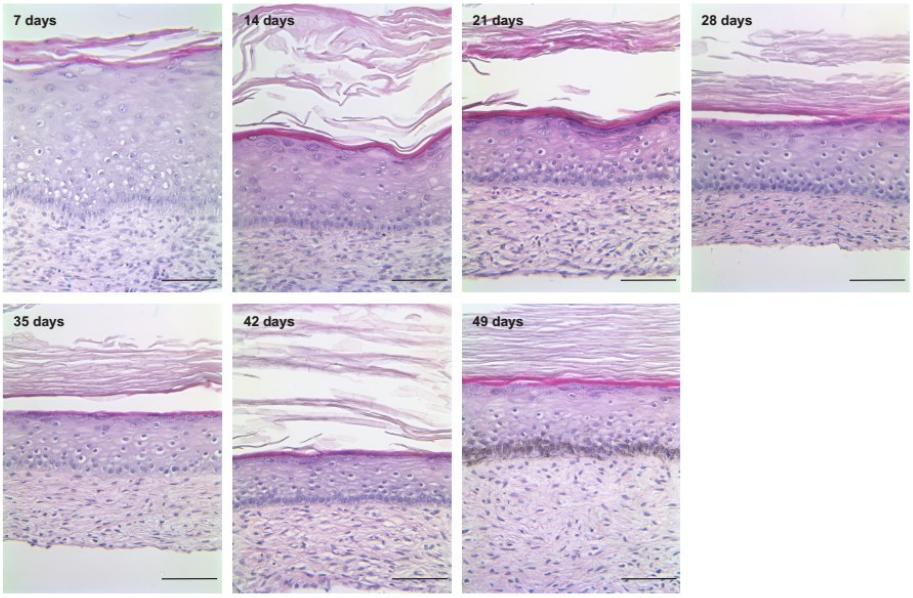

***Figure 3.2**. Histological analysis of the developed HSEs up to 7 weeks of culture; on the paraffin section. The scale bar represents 100 µm. HSEs older than 28 days are n=3; while models younger than 28 days are n>3.*

Histological examination of the 3D HSEs (**Figure 3.2**) revealed a well-stratified epidermis, which is differentiated into four distinct layers- cornified, granular, spinous and basal. The images show the formation of a basement membrane separating the homogeneous dermis from the epidermis layers. As expected, the thickness of cornified epidermis was increased with increasing the duration of ALI culture. For the first time, it was shown that up to 7 weeks no histological changes owing to the instability of the model could be observed. Staining with Ki67, which is a proliferation marker further confirmed the viability of the epidermis for the cultured time (**Figure 3.3**).

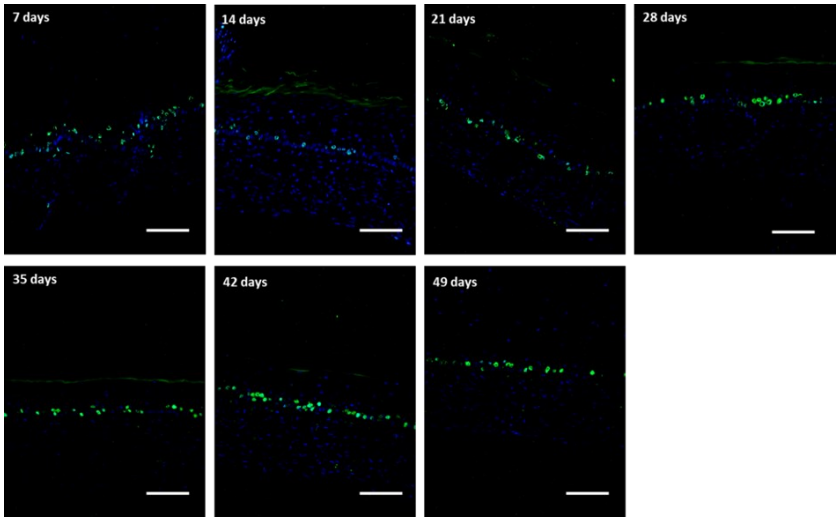

***Figure 3.3**. Ki67 staining of HSEs at different time points shows the long-term viability of HSE. The scale bar represents 100 µm.*

Measuring the thickness of the dermis for each time point showed a maximum increase in thickness after 49 days (**Figure 3.4**). Additionally, the fibroblast density used to make the model can further augment the ECM production. Conventional collagen gels used for skin models suffer from contraction due to the exertion of traction force by the fibroblasts on local collagen fibers[138] and are prone to degradation by matrix metalloproteases (MMPs) after two weeks,[139] making them unstable for long term culture.

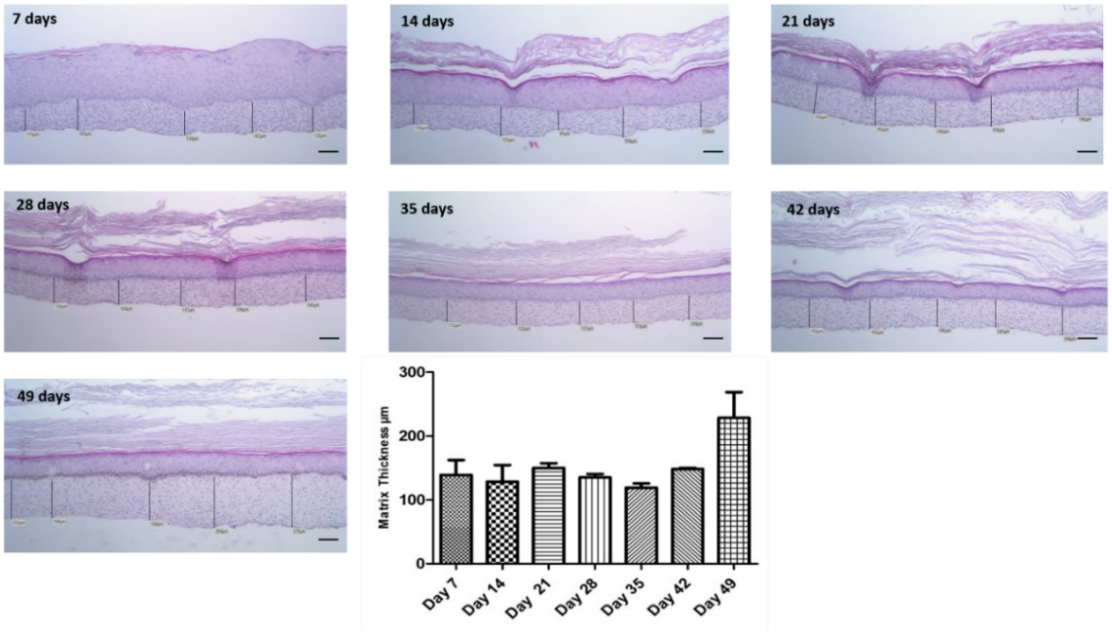

***Figure 3.4**. Thickness of the dermis at five different spots for each time point was measured and a graph is plotted for the thickness of the HSE versus duration of culture. Error bars indicate standard deviation.*

Contrary to this, FN-G nanofilm coating onto single-cell surfaces promotes the formation of an ECM, while Van der Waals interactions and biological recognitions between layers ensure the arrangement of macromolecules in their most stable conformation. The integrins on the cell membrane link the actin cytoskeleton within the cell to external structures in the ECM, allowing cell-cell contact and cell-ECM contact. Based on these characteristics, HSEs that were produced by cell-accumulation technique can be cultivated over a longer period than collagen-based models **(Figure 3.5).**

A fine balance between cellular proliferation and differentiation is required to maintain epidermal homeostasis. Therefore, to better characterize proteins of the epidermis and the dermis, various immuno-markers were used (**Figure 3.6 a-g**). Filaggrin staining in **Figure 3.6b** shows the staining of well-developed keratin fibers in epithelial cells that forms a cornified envelope of *stratum corneum*. Filaggrin is an S100 fused type of protein essential for epidermal function.[140, 141] Its disruption or deficiency leads to abnormal epidermal differentiation and epidermal barrier defects as seen in the case of atopic dermatitis and psoriasis.[142, 143] Cytokeratin 10 (K10) is the early differentiation marker of

keratinocytes. These keratin filaments are present in the intracytoplasmic cytoskeleton of the *stratum spinosum* of the epithelium (**Figure 3.6c**).

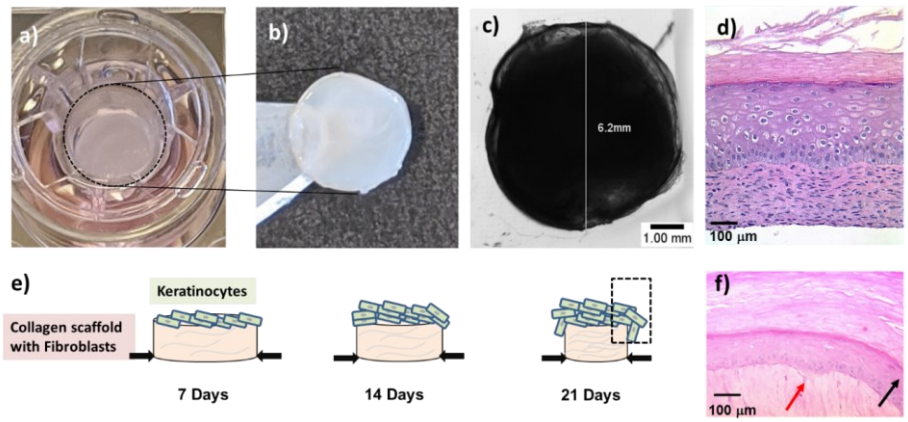

Figure 3.5*. a) Photograph of the insert with HSE fabricated using cell coating shows no contraction after 21 days b) HSE after being removed from the insert (diameter of 6.5 mm), c) bright field image of the HSE, d) histological image of HSE prepared by cell coating (21 days) and e) graphical representation: contraction of collagen based HSE with time and infiltration of keratinocytes in the dermal compartment (inset). f) Histological image of collagen based HSE after 21 days of culture. Compared to cell coating the collagen based HSE shows clear signs of degradation, the red arrow indicates the degeneration of the basement membrane, while the black arrow indicates infiltration of the keratinocytes in the dermal compartment.*

Integrin ß4 (ITGß4) is a receptor for laminin. It plays a structural role in cell-cell contact of hemidesmosomes in epithelial cells of the epidermis. ITGß4 staining shows the polarizing keratinocytes adjacent to the basement membrane (**Figure 3.6d**), while **Figure 3.6e** shows proliferating keratinocytes by Ki67 staining. **Figure 3.6f** shows the staining for collagen IV, which is a major component of the basement membrane while vimentin is the cellular maker for the fibroblast layer (**Figure 3.6g**).

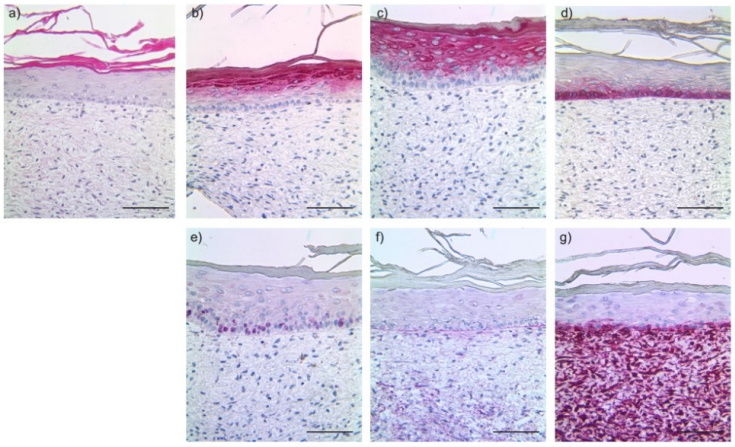

Figure 3.6. *Immuno-histological characterization of the HSEs after three weeks of cultivation. a) HE staining. Immuno-histochemical staining demonstrates the presence of b) FLG, c) cytokeratin 10, d) integrin β, e) Ki67, f) collagen IV and g) vimentin. Representative images are shown. Scale bar represents 100 µm.*

To validate the potential applications of the HSE as a disease-specific skin model and as a model for pharmacological examinations, the model was utilized for a study of psoriatic phenotype progression and remission. For disease progression, rhIL-17A was used while for disease remission fully humanized IgG1κ monoclonal antibody Secukinumab was applied. This anti-IL-17A antibody selectively targets IL-17A and blocks its interaction with the IL-17 receptor (IL-17RA/IL-17RC receptor complex).

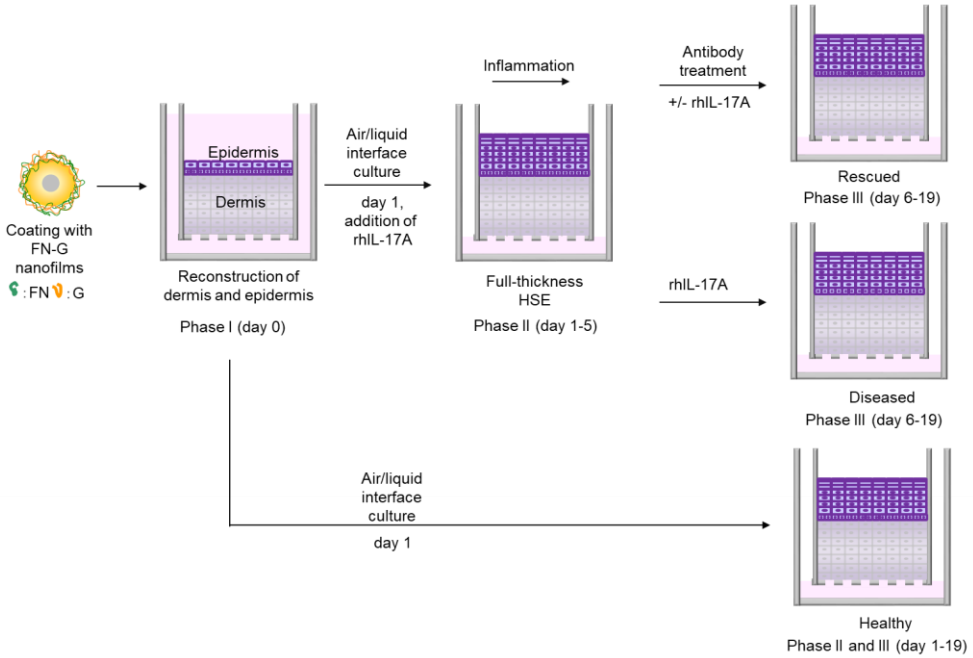

Scheme 3.1 *Study design. The study was divided into three phases: The first phase (day 0) comprised the reconstruction of the dermis and epidermis. Within the second phase (day 1-5), HSEs were lifted to the ALI and stimulation with rhIL-17A was conducted. The third phase was divided into three different approaches. While an untreated model served as a control (healthy), one model was stimulated further with rhIL-17A (diseased) and the third model was treated with the anti-IL-17A antibody, with or without rhIL-17A (rescue).*

In the pathogenesis of chronic plaque psoriasis, the cytokine IL-17A functions as an important effector cytokine of the T_h17 cell lineage. It exerts its biologic function through binding to the respective transmembrane IL-17 receptor (IL-17R) which is highly expressed on the surface of keratinocytes. In addition to T cells, IL-17A is also secreted from mast cells and neutrophils during the development of psoriasis.[144] This maintains a positive flux for increased production of IL-17A and other mediators involved in the psoriasis gene signature. To model this pathomechanism, after ALI, rhIL-17A was added for 5 days. This was followed by the addition of secukinumab, an antibody against IL-17A along with the addition of rhIL-17A for 14 days (**Scheme 3.1**). As controls untreated and rhIL-17A treated HSEs were used.

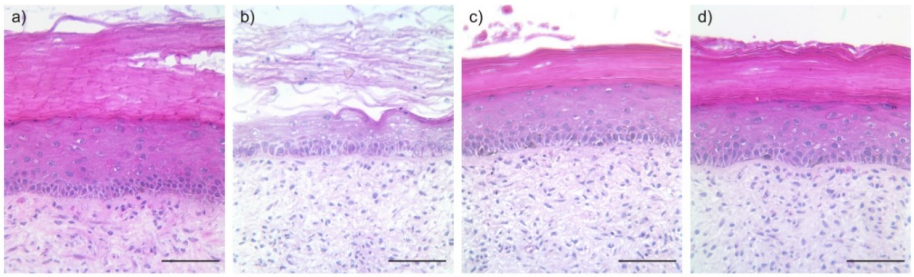

Figure 3.7*. Treatment with an anti-rhIL-17A antibody reverted the cytokine-induced psoriatic phenotype in HSEs. Representative HE images of a) untreated controls, b) rhIL17A-stimulated HSEs, c) HSEs that were stimulated with rhIL-17A for 5 days and then additionally treated with an anti-IL17A-antibody for 14 days (+ rhIL17A), d) HSEs that were stimulated with rhIL17A for 5 days and then only treated with an anti-IL17A-antibody for 14 days (- rhIL17A). Scale bars: 100 µm.*

Histological assessment of HSEs treated with rhIL-17A for a total of 19 days demonstrated strong inhibition of keratinocyte differentiation. As a result, hyperproliferative epidermis with premature differentiation of keratinocytes is seen in these models. In psoriatic lesions, the granular layer is reduced and the *stratum corneum* is formed by incomplete cornified keratinocytes - a phenotype that occurred in the HSEs treated with rhIL-17A (**Figure 3.7b**) compared to the non-treated control (**Figure 3.7a**). These morphological features of psoriasis were completely negated when the HSEs were treated with anti-IL17A antibody for 14 days with (**Figure 3.7c**) or without rhIL-17A (**Figure 3.7d**). These results suggest that secukinumab reverts psoriasis-like morphology in HSEs and for the first time it was shown that, the HSEs could be 'rescued' after the induction of psoriasis-like phenotype for 14 days along with the antibody. This characterization of the established HSEs shows that these models can mimic the clinical scenario where T_h17 cells in diseased skin constantly produce IL-17 and new biologicals such as an anti-IL17A antibody are administered to achieve therapeutic effects. To show the longevity of models, as a follow-up, the HSEs were treated by rhIL-17A for 5 days followed by the addition of secukinumab for 23 days. It could be seen that the models were stable and were completely recovered from the psoriatic phenotype (**Figure 3.8**). This was further confirmed by immunofluorescence staining of CK 6, CK 16, Ki 67 (**Figure 3.9, 3.10, 3.11**)

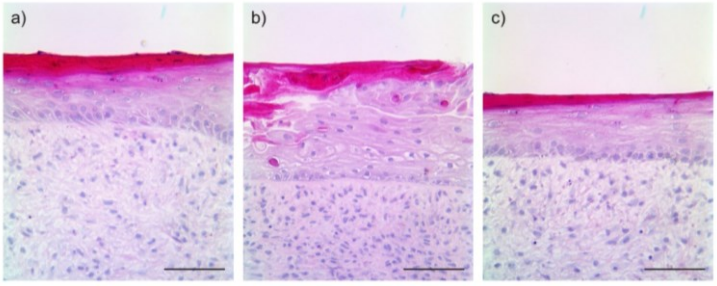

Figure 3.8. *Histological analysis of a) an untreated HSE, b) HSE treated with rhIL-17A (50 ng/ml), and c) HSE treated with rhIL-17A (50 ng/ml) and anti-rhIL-17A antibody (6.0 µg/ml) over a period of 28 days. The scale bar represents 100 µm.*

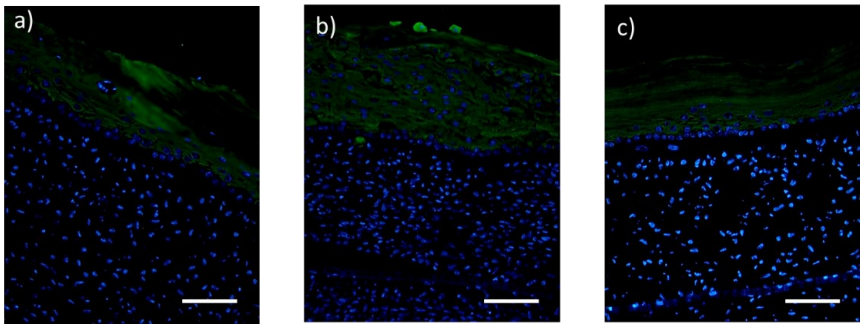

Figure 3.9. *CK6 staining of HSEs a) untreated b) IL 17 treated and c) IL 17 + anti-rhIL-17A antibody after 28 days. The scale bar represents 100 µm.*

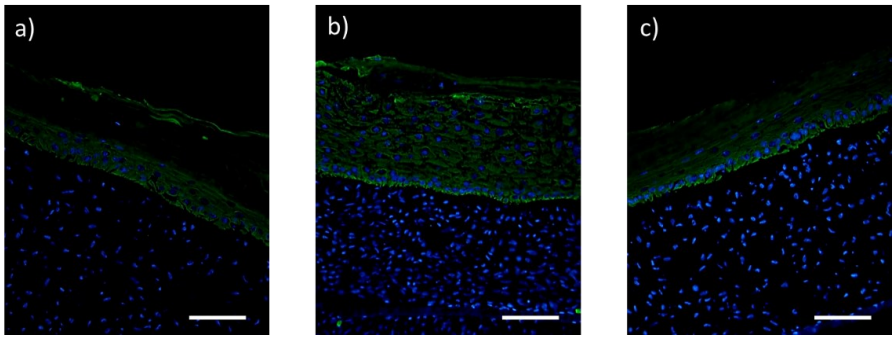

Figure 3.10. *CK16 staining of HSEs a) untreated b) IL 17 treated and c) IL 17 + anti-rhIL-17A antibody after 28 days. The scale bar represents 100 µm.*

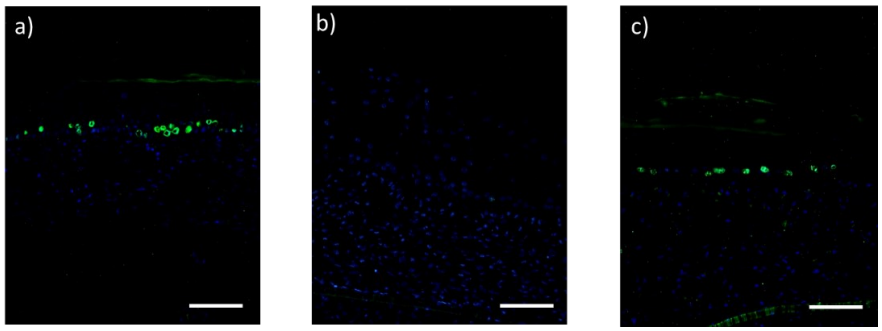

Figure 3.11. *Ki67 staining of HSEs a) untreated b) IL 17 treated and c) IL 17 + anti-rhIL-17A antibody after 28 days. The scale bar represents 100 µm.*

The effect of rhIL-17A inhibition on the FLG expression was further evaluated using immunofluorescence staining (**Figure 3.12**). In psoriasis, late differentiation markers like pro-FLG and loricrin disappear as a result of accelerated keratinization with premature cell death. Additionally, IL-17A down-regulates the expression of FLG as well as the genes that encode FLG processing and inhibits the expression of tight junctions' desmosomes proteins and the epidermis-associated adhesion molecules such as ZO-1 and ZO-2, E-cadherin and various integrins respectively., molecule.

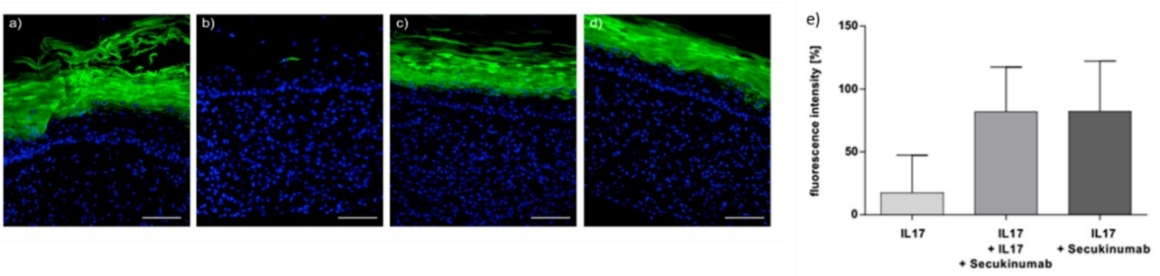

***Figure 3.12**. The effects of anti-IL-17A antibody treatment on rhIL-17A induced impairments were evaluated based on its impact on the FLG expression using immunofluorescence staining. a) untreated control, b) rhIL17A-stimulated HSEs, c) HSEs that were stimulated with rhIL-17A for 5 days and then additionally treated with an anti-IL17A-antibody for 14 days (+ rhIL17A), d) HSEs that were stimulated with rhIL17A for 5 days and then only treated with an anti-IL17A-antibody for 14 days (- rhIL17A). The scale bar represents 100 µm. e) Evaluation of fluorescence intensity, normalized to the untreated control. Error bars indicate standard deviation (n=3).*

In both models treated with anti-IL17A-antibody for 14 days (+/- rhIL17A) FLG expression could be restored (**Figure 3.12c and d** respectively) compared to the rhIL-17A stimulated models (**Figure 3.12b**). The relative fluorescence intensity of both models (Figure 4c-d) was normalized to the untreated control condition (**Figure 3.12a**). In the psoriasis-like model, the intensity was reduced to 15 % (**Figure 3.12b**). However, treatment with anti-IL-17A antibody restored the FLG expression up to 80% (**Figure 3.12e**) in both the models +/- rhIL-17A in Phase III. This shows that FLG expression could be restored in a psoriasis-like condition using anti-IL-17A-antibody, even after the HSEs were continuously subjected to rhIL-17A.

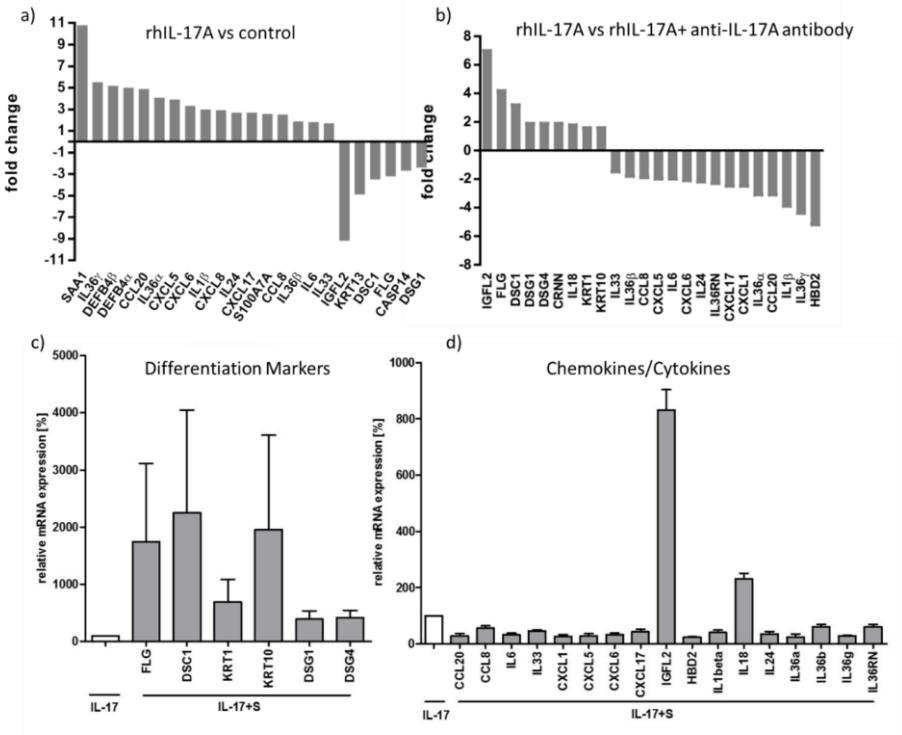

***Figure 3.13.** Gene expression profiling using microarray analyses was used to investigate (a) the effects of rhIL-17A stimulation on HSEs and (b) the effects of treatment with an anti-IL-17A antibody on*

rhIL17A stimulated HSEs. RT-PCR analyses confirmed the gene regulations of specific (c) antimicrobial peptides and (d) chemokines and cytokines in HSEs that were treated with the anti-IL17A antibody. S = Secukinumab.

Investigating the molecular effects in more detail additional gene expression profiling (**Figure 3.13a and b**) was performed. Models that were treated with rhIL-17A showed on the one hand a downregulation of differentiation markers (e.g. FLG, KRT13) and on the other hand an upregulation of chemokines and cytokines (e.g. CXCL5, IL36) (**Figure 3.13a**). Similar gene regulations can be found in skin lesions of psoriasis patients. Interestingly, treatment with an anti-IL17A antibody reverted these gene regulations only 14 days after initiation of the treatment (**Figure 3.13b**). These data demonstrate at the molecular level the 'reversing' effects of anti-IL-17A antibody on rhIL-17A-induced gene regulations.

To confirm the microarray data real time -PCR was performed (**Figure 3.13c and d**). In *in vivo*, IL-17A activates CCL20, CXCL1, CXCL2, and CXCL8/IL-8 synthesis, leading to the recruitment of more IL-17-producing T cells and neutrophils into the skin. Thus, blocking IL-17A using anti-IL17A antibody downregulated CXCL 1, 2, 8 and antimicrobial peptides DEFB4-α, -β, CCL20 (a chemotactic for T cells and DCs), CCL8, IL-6, and IL-33. IL-36 cytokines are induced in response to IL-17A in HSE, inhibiting IL-17A downregulated IL36 expression, which leads to the interruption of a feedback loop of the IL-17 signal pathway which might explain the rapid onset of the IL-17A antagonist compared to other biologics used in the treatment of psoriasis (anti IL-23, anti-TNFα).

Interestingly after treatment with the antibody upregulation of two other markers, IGFL-2 and IL-18 were observed. The potential role of IGFL in psoriasis is not well understood. IGFL proteins demonstrate the closest similarity with IGF family, however, their physiological functions are not defined yet.[145] A former study revealed that IGFL-2 downregulation is detected in skin samples of psoriasis patients.[146] Interestingly, treatment of the psoriasis-like HSE with Secukinumab led to a significant upregulation of IGFL-2 expression. Its structural similarity to IGF family suggests that these proteins could act as growth regulators, hence understanding its role in the pathogenesis of psoriasis may further give an insight into its role in the pathogenesis of psoriasis and its treatment.[147]

Keratinocytes in all living layer of epidermis show the presence of IL-18 and its receptors. The release of IL-18 affects the surrounding keratinocytes in an autocrine and paracrine manner. In normal skin this results in preserving the homeostasis of a T_h1 dominant state.[148] However, psoriasis-like symptoms are aggravated combination of IL-18 with IL-17.[148] It was assumed that the addition of rhIL-17A further upregulates the IL-18 production in this model and blocking rhIL-17A, mechanistically did not influence IL-18 regulation. Further dynamics of IL-18 and IL-18 receptor in diseased skin as compared to normal skin have to be investigated to have a better insight.

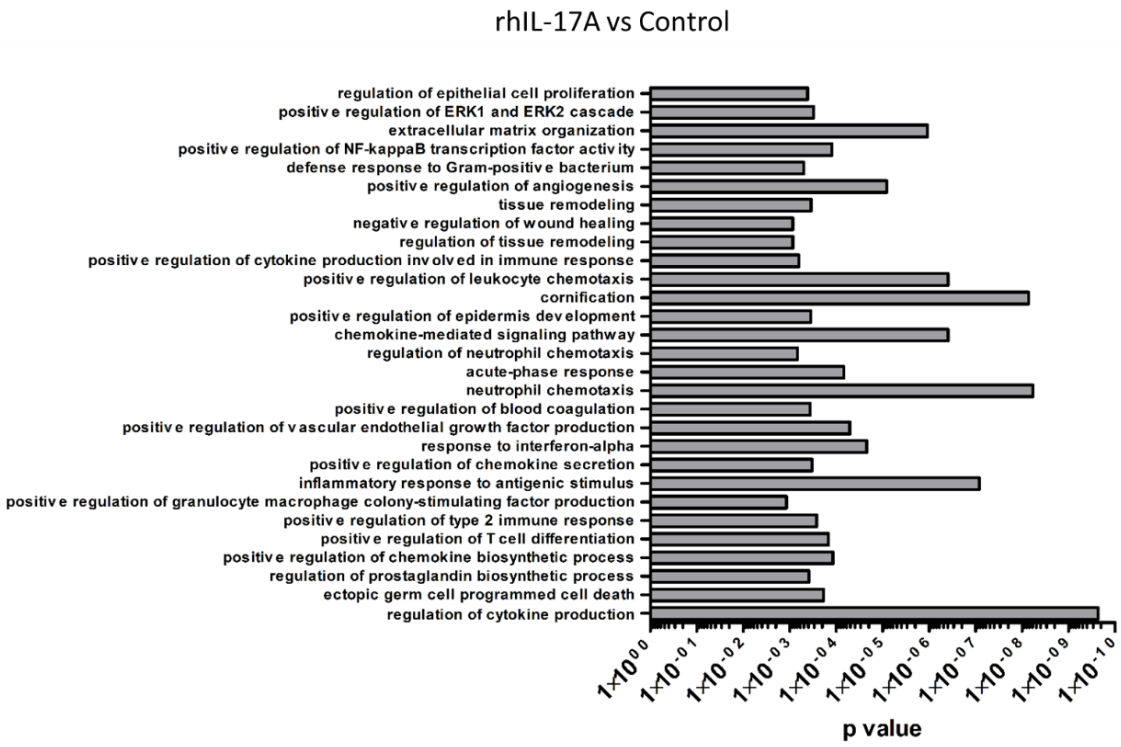

***Figure 3.14**. Gene ontology (GO) analysis revealed an impact of rhIL17A on the developed HSEs.*

Gene ontology (GO) analysis revealed an impact of rhIL17A on biological processes such as "regulation of epithelial cell proliferation", "positive regulation of cytokine production involved in immune response" and "positive regulation of chemokine secretion" (**Figure 3.14**). These data substantiate the pro-inflammatory and chemotactic effects of rhIL17A on the established HSEs.

3.4. Conclusion

The cell coating technique was used to fabricate the 3D skin equivalents. This technique involves layer-by-layer assembly of extracellular matrices nano-films on the cell surface and allows the rapid fabrication of scaffold-free skin models. After lifting the model to the air-liquid interface on day three, keratinocytes as a major cell population showed homogeneous differentiation into four layers on the surface of the dermis. Histological examination revealed a stable skin equivalent in long-term cell culture (49 days), this is beyond any reported state of the art.

Owing to the long-term stability of the skin models, a 3D psoriatic skin model was further developed that mimics the clinical psoriatic phenotype. The pilot study consisted of inducing the psoriasis phenotype by stimulation of the skin equivalents with 50ng/mL rhIL-17A for five days, followed by a systemic treatment from day 6 to day 19 with the monoclonal antibody secukinumab along with rhIL-17A. After treatment with an anti-IL7A antibody, upregulation of keratinocytes differentiation markers such as FLG, KRT1, KRT10, DSG 1 and 4 and downregulation of antimicrobial peptides such as DEFB4B, DEFB4A (HBD-2) was observed. Inhibiting rhIL-17A also downregulated CCL20 (a

chemotactic for T cells and DCs), CCL8, CXCL1, 2, 8, IL 6, IL33 and IL36. To conclude, a psoriatic-like disease phenotype could be induced in a 3D organotypic skin model and in addition also demonstrated the restoration of the model by antibody treatment. For the first time, the performed study aimed at mimicking the clinical situation in psoriasis. In the next step, it is planned to induce the psoriasis phenotype for 5 days, followed by 14 days of treatment with biologicals and then withdraw the treatment and monitor the washout phase for an additional 14 days. Furthermore, it is known from the clinical practice that especially laser- and aesthetic treatments reveal clinical effects up to two months after treatment, these effects can only be monitored in a long-term 3D skin model. The use of developed skin models has the potential to act as an alternative to diseased tissue biopsies and animal testing.

Chapter 4

The role of dynamic flow environment in the maintenance of skin vascularization

This chapter was adapted with permission from the publication "Dynamic flow enables long-term maintenance of 3-D vascularized human skin models" in *Applied Materials Today*. 2021 Dec 1; 25: 101213.
Direct link: https://www.sciencedirect.com/science/article/pii/S2352940721002766. All schematics were created using Biorender.

4.1. Introduction

Skin is the largest organ of the human body. As the outermost organ, the skin is continually in contact with the external environment and is susceptible to various ailments that range from benign to malignant. To combat skin diseases that arise due to environmental factors, barrier dysfunctions as well as genetic conditions, novel therapeutic agents have to be tested and their efficacy and side effects need to be thoroughly investigated. Conventionally, drugs and cosmetics are tested on two-dimensional (2D) monocultures or animal models. However, 2D cultures lack the complex architecture of the native skin tissue. In contrast, animal models are highly complex but are known to have variations from human tissue architecture and the underlying cellular mechanisms. Such differences narrow down direct cross-species translation of findings, limiting the applicability to humans.[11] Furthermore, ethical issues on the use of animals for drug testing remain. This strengthens the necessity for *in-vitro* human 3D skin models that can recapitulate the complexity and response of the native human skin tissue.

An essential step in the development of a physiologically relevant *in-vitro* skin model is the incorporation of functional blood vessels (BVs). Adequate vascularization is a prerequisite for the survival and maintenance of lab-grown tissues.[149] BVs serve as a biological pipeline for the transport of oxygen, nutrients, and growth factors to individual cells, and most importantly, play an active role in maintaining tissue homeostasis. Also, BVs are a vital component in several skin diseases and could emerge as a potential target for novel therapies.[150] Although, the importance of BVs in tissue models is widely accepted, most conventional HSEs lack BVs. The advent of current tissue engineering strategies has facilitated the fabrication of vascularized human skin equivalents (vHSEs). However, the challenge of maintaining the stability and durability of the developed vHSEs for a long duration persists and as a result, most vHSEs are cultured only for short periods. Unfortunately, the source and the solution for the instability of both vascularized and non-vascularized HSEs are seldom reported in the literature.[24]

In general, the instability of HSEs can be attributed to the contraction of the dermal scaffold that is facilitated via the traction force exerted by the dermal fibroblast on the surrounding matrix.[151] Several strategies have tackled the issue of gel contractility in HSEs by the utilization of cross-linkers,[152] proteinase inhibitors,[153] or the inclusion of scaffolds.[154] However, such techniques could hamper the introduction of vasculature into the models as well as the process of vasculogenesis and subsequent angiogenesis. Endothelial cells (ECs) require an appropriate surrounding environment for cellular proliferation, migration, tube formation, micro-vessel branching, and maintenance.[155] Concomitantly, the stability of BVs in vHSEs is challenged by the EC-mediated proteolysis of the surrounding extracellular matrix (ECM).[156] This may lead to loss of matrix support, apoptosis of the ECs due to integrin detachment from the ECM, and vascular regression. Another aspect that is overlooked during the construction of vHSEs is the role of keratinocytes (KCs), the prominent cells present in the epidermis. It is known that KCs modulate the balance between the expression of MMPs and tissue inhibitor of metalloproteinase (TIMPs) as well as secrete angiogenic growth factors such as vascular endothelial growth factor (VEGF).[157] BVs in turn can respond to such factors and undergo rapid branching or regression depending on the signal.[158] The cross talk between KCs and the vascularized dermis results in a vicious cycle of vascular regression and matrix degradation *in vitro*.[158] Additionally, the presence of numerous cell types could also have a detrimental effect on the overall integrity of the engineered tissue. Thus, to recapitulate a multicellular tissue with vasculature is a challenge, as it not only requires distinct nutrient and growth factor composition in culture media but also the regulation of cell-cell, cell-ECM interaction for maintenance of homeostasis. *In vivo* the quiescence of BVs is attributed to 1) a feedback loop that maintains multiple cell types and ECM proteins interaction 2) continuous replenishment of oxygen and nutrients as well as constant removal of cellular waste 3) mechanical stimulus.[159, 160] It was therefore hypothesized that tissue homeostasis and vascular quiescence can be maintained by fabricating a scaffold-free vHSEs (with physiological cell-cell and cell-ECM interactions) cultured in a dynamic flow environment.

Unlike the conventional HSEs cultured under static conditions, native skin tissue encounters numerous forces such as mechanical tension and compression, interstitial fluid flow, shear stress, and pressure changes. Previous reports have elucidated the influence of dynamic cultures on the epidermal component of the HSEs, mostly showing improvements in the barrier properties.[161-164] Only a few examples where a dynamic flow culture was utilized to cultivate vHSEs are reported.[102, 103, 105, 107, 165] To the best of knowledge to date, the influence of a dynamic flow environment in sustaining long-term vessel architecture, dermal integrity, and thereby maintaining vHSEs homeostasis has not been explored in its entirety.

This chapter reports the fabrication of scaffold-free vHSEs by utilizing cell-coating and accumulation technique that allows for rapid assembly of cells into viable tissues.[166] The effect of dynamic flow on the maintenance of vHSEs homeostasis was explored **(Schematic 4.1)**.

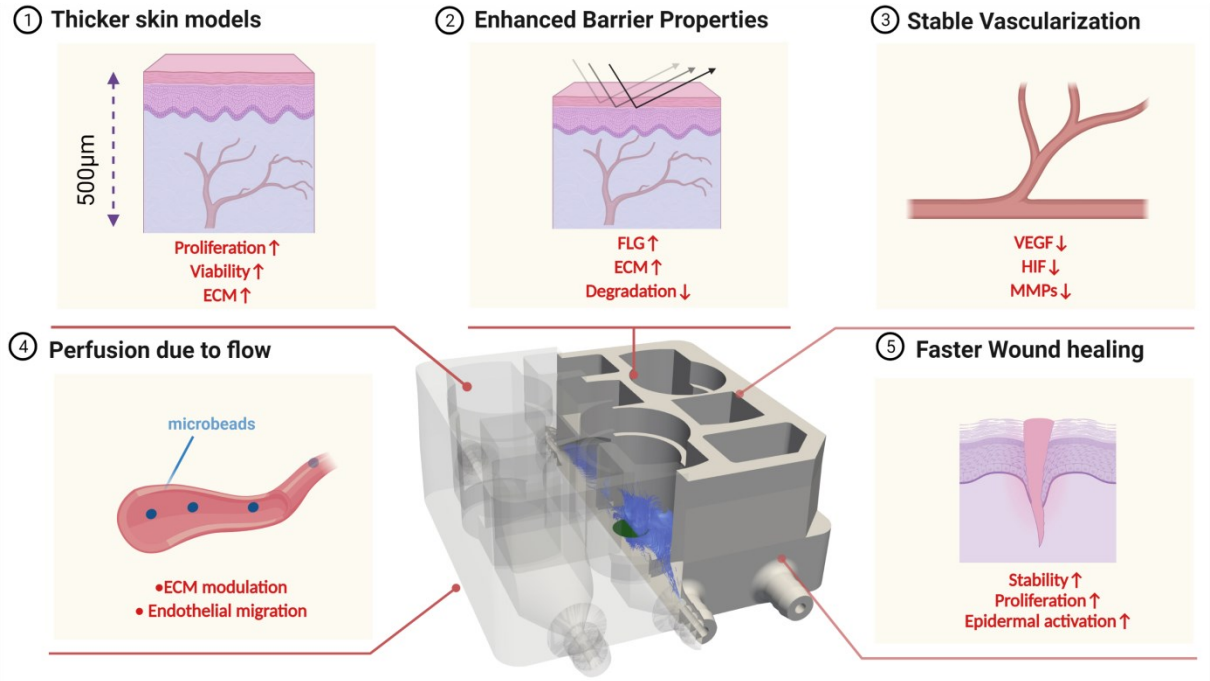

Schematic 4.1 *summarizes the influence of bioreactor-based flow cultivation on several aspects of vHSEs that enable the long-term maintenance of vascularized skin tissues in-vitro. Factors such as vascular stability, barrier properties, perfusion, viability, and ECM deposition are paramount in the fabrication of long-term vHSEs.*

The vHSEs were cultivated in custom-built 3D printed bioreactors with continuous media perfusion of the dermal compartment. The epidermal compartment was exposed to air, thereby mimicking the native skin physiology. It was shown that flow culture mitigates the uncontrolled formation of BVs in the vHSEs by the modulation of vascular endothelial growth factor (VEGF), hypoxia inducible factor 1A (HIF1A), and MMPs/TIMPs gene expression. Apart from the enhancement of barrier properties, optimal epidermal differentiation, ECM modulation, and improved dermal stability, flow culture also resulted in the formation of perfusable vascular openings attributed to the flow patterns and angiogenic growth factor gradients. As an example of the application of flow culture, 3D wound healing assay was conducted and differences in wound closure was demonstrated in the flow as compared to static culture. Together, this chapter attempts to explain the basis of vascularized tissue disintegration and creates a benchmark for future studies involving lab-grown tissues with different cell types.

4.2. Materials and Methods

Human dermal fibroblasts and human KCs isolation

NHDFs and KCs were obtained by isolation of skin biopsies, surgically extracted from healthy volunteers (Department of Dermatology, RWTH Aachen University Hospital, Germany). Extraction and isolation were conducted in accordance with the Declaration of Helsinki principles and was approved by the ethical committee of RWTH Aachen University hospital, Germany, Project Number EK188/4. The excised skin tissue was washed thrice with 70% ethanol (VWR). The tissue was incubated for 12 hours in 25U/ml type 2 dispase (Gibco) in PBS. Following this, the epidermis compartment was peeled off from the dermal compartment. The dermal compartment was digested using 1mg/ml type 2 collagenase in PBS (3 hours) at 37 degrees. DMEM (10% FBS) was added to the digested fibroblasts and sieved through a 100 µm strainer. The filtered fibroblasts were centrifuged (500 g, 5 minutes). Cells were cultivated in DMEM. The peeled-off KCs were incubated with 0.25mg/ml Trypsin/EDTA (Lonza) for 30 mins. The tissue was sieved through a 100µm strainer. The digested tissue was then centrifuged at 300 g for 5 minutes. KCs were cultivated in Dermalife complete media and used until Passage 3.

ECM-coating of single cells

Individual fibroblasts were coated layer-by-layer with FN and G moieties as previously described [94]. Products used in the study are listed in **Supplementary Table S4.2**. Briefly, dermal fibroblasts were trypsinized, centrifuged, and washed with 1X PBS. The cells were alternatively mixed with 0.04µg/ml FN and 0.04µg/ml G with an intermediate PBS washing step. After each mixing step, the cells were centrifuged for 1 minute at 400g. A total of 9 coating steps were performed. Coated fibroblasts were then mixed with uncoated HUVECs in the ratio of 5:1 and then seeded inside 0.4µm pore-sized 6.5mm diameter trans-well inserts (corning). A total of 1.5×10^6 coated NHDFs (that form 15 layers) and 3×10^5 uncoated HUVECs (that form 3 layers) was used to fabricate one vHSEs. The NHDFs were used from passages 4-9 and HUVECs were used until passage 5. The formed dermis model is incubated for 24 hours (37°C, 5% CO_2) in *dermal media* **(Supplementary Table S4.1).**

Addition of KCs and Air liquid interface (ALI)

The next day, 1.8×10^5 KCs in 300µl of *keratinocyte growth media* **(Supplementary Table S4.1)** were seeded on top of the formed dermis layer. The lower compartment of the trans-well was filled with 1 ml of *dermal media* **(Supplementary Table S4.1)**. The construct was incubated for 2 hours at 37°C and 5% CO_2 to allow optimal attachment of KCs to the dermal compartment. After the incubation time, the media from the outer and inner parts of the trans-well inserts was extracted and 2.3 ml of fresh *growth media* **(Supplementary Table S4.1)** was added. The models were incubated for 24 hours. The next day, media from the well plate was completely extracted and the outer compartment of the trans-well was filled with 1 ml of *differentiation media* **(Supplementary Table S4.1)** whereas no media was

added to the upper compartment. The model was cultured in ALI where the dermal compartment was in contact with the media and the KCs were in contact with air. The tissue was further cultured for 5 days in *differentiation media* and ALI with media changes every alternate day. The trans-well inserts (for flow culture) were then shifted to the 3D printed flow reactor and stimulated for 7, 14, and 21 days.

Quartz Crystal Microbalance with Dissipation (QCM-D) analysis

QCM-D analysis on gold-coated sensors (QSensor QSX 301 Gold) was performed to observe FN-G layer by layer deposition. QCM-D technique can measure the shift in frequency (Δf) and change in dissipation (Δd). The thickness of 9 steps FN-G coating on gold-coated Sensors was analyzed by Qsense Dfind software. Briefly, sensors were exposed 1 X PBS for 10 minutes. Subsequently, 0.04mg/ml FN was pumped to the sensors for 10 minutes. This was followed by PBS wash and G (0.04mg/ml) exposure for 10 minutes. This alternate coating of FN-G was continued for 9 steps. The fluid flow rate was 0.1ml/min. The Δf and Δd were observed and the mass change was quantified by the viscoelastic smartfit model configuration.

3D printed flow device

The 3D printed flow device was fabricated layer-by-layer with a photopolymer (Stratasys, VeroClear) using a polyjet 3D printer (Statasys, Objet Eden 260 V). The flow bioreactor was designed to allow flow stimulation of submerged cultures as well as skin models subjected to ALI. The multi-chamber device allowed the placement of culture inserts containing the skin models such that the basal compartment could be exposed to a continuous flow of fresh media whereas the KCs on the top could be exposed to air. Each insert has dedicated input and output channels through which the media could be perfused. A peristatic pump REGLO Digital MS-4/6 (catalog ISM 8336) that has a flow rate range from 0.002 to 43 mL/min was used in this chapter. For the experiments, a flow rate of 5mL/min that corresponds to a velocity of 0.0256 m/s was utilized. The difference of pressure across the membrane during flow was quantified to be approximately 27 Pa.

Numerical simulations

The simulations have been carried out with the open source finite volume toolkit OpenFOAM.[167] First, the flow in the bioreactor without the cell culture insert and the membrane were analyzed. The volume-of-fluid method has been employed.[168] The 3D Navier- Stokes equations are coupled with a transport equation for the indicator function α, representing the evolution of the volume fraction of one of the phases. The following system of equations has been analyzed:

$$\frac{\partial(\rho \mathrm{U})}{\partial t} + \nabla \cdot (\rho \mathrm{U} \otimes \mathrm{U}) = -\nabla p + \nabla \cdot (\mu[\nabla \mathrm{U} + \nabla \mathrm{U}^T]) + \rho \mathrm{g} + \sigma \kappa \nabla \alpha \,,$$

$$\nabla \cdot \mathrm{U} = 0 \,,$$

$$\frac{\partial \alpha}{\partial t} + \nabla \cdot (\mathrm{U}\alpha) = 0\ ,$$

Here U is the interfacial velocity, p is the pressure, g is the gravitational acceleration and σ is the surface tension at the interface. κ is the local interfacial curvature which is obtained from the volume fractions using the following expression[169]

$$\kappa = -\nabla \cdot \left(\frac{\nabla \alpha}{|\ \nabla \alpha\ |}\right).$$

ρ, μ are the density and the kinematic viscosity, respectively, defined as,

$$\rho = \alpha\rho_1 + (1-\alpha)\rho_2$$

and

$$\mu = \alpha\mu_1 + (1-\alpha)\mu_2\ .$$

Both phases (physiological fluid and air) are assumed to be incompressible Newtonian fluids with fluid kinematic viscosity $\mu_1 = 9.4 \times 10^{-7}\ \mathrm{m}^2/\mathrm{s}$, fluid density $\rho_1 = 1000\ \mathrm{kg/m}^3$ and air kinematic viscosity $\mu_2 = 1.57 \times 10^{-5}\ \mathrm{m}^2/\mathrm{s}$, air density $\rho_2 = 1\ \mathrm{kg/m}^3$, respectively. The phase volume fraction α assumes values in the range of 0 and 1 for the air and the fluid, respectively. A 60^o contact angle between the fluid and the bioreactor walls was estimated by comparing simulation with experimental results. The surface tension of the fluid is assumed to be $0.056\ \mathrm{mN/m}$. Non-slip velocity wall boundary conditions were applied at the bioreactor walls. The numerical simulations have been carried out with an in-flow rate of $5\ \mathrm{mL/min}$ which corresponds with $0.0256\ \mathrm{m/s}$ inlet fluid velocity ($2\ \mathrm{mm}$ inlet diameter).

For the simulation of flow in the bioreactor with the insert and the membrane, the system of equations is extended by an additional source term in the Navier-Stokes equations, which describes the total drag per unit volume acting on the fluid the porous structure.[169] It is expressed in the form of the Darcy law

$$\mathrm{S} = -\mu D \mathrm{U}_D$$

Here U_D is the Darcy velocity, D is the Darcy coefficient given by

$$D = \frac{1}{K}$$

with K as the intrinsic permeability of the membrane. The intrinsic permeability is chosen to

$$K = \phi k_{pore}$$

here ϕ is the porosity of the membrane and k_{pore} is the average permeability of each pore of the membrane given by [170]

$$k_{pore} = \frac{{r_{pore}}^2}{8}$$

with r_{pore} being an average radius of pores in the membrane.

The membrane with a diameter $d_c = 6.5$ mm, thickness $h = 10$ µm and an average pores diameter $d_{pore} = 2r_{pore} = 0.4$ µm has been simulated. The average permeability of a single pore is given by $k_{pore} = 5 \cdot 10^{-15}\ m^2$.

The porosity of the membrane has been estimated based on the image analysis of the insert membrane. First, the background noise of the confocal image is reduced by applying a Wiener filter and then, the ratio between pores and the rest of the membrane is calculated. The membrane porosity is estimated to be around 20% or $= 0.2$. This estimate leads to the Darcy coefficient equal to $D = 10^{15}\ \mathrm{m}^{-2}$.

The fluid streamlines in the bioreactor at the in-flow rate of 5ml/min are shown in **Figure 4.10.** The streamlines clearly demonstrate that the flow is mainly perpendicular to the membrane surface and the fluid can penetrate through the membrane. To estimate the pressure difference across the membrane, the static pressure in the center of the bioreactor has been calculated with and without the membrane. The pressure along the Z-axis of the bioreactor for the flow rate 5 mL/min at 79.7 sec can be seen in **Figure 4.11.** The difference in the pressure across the membrane is approximately 27 Pa.

Tissue viability assay

The viability of tissue was tested using the CellTiter-Glo® 3D Cell Viability Assay. The assay was conducted according to the manufacturer's protocols. Briefly, 21 days static and flow cultivated tissues were removed from the culture inserts and washed twice with PBS. CellTiter-Glo® reagent was added to the tissues and mixed thoroughly for 5 minutes to induce cell lysis. The samples were then placed on a shaker for 30 minutes. The measurement of luminescence determined the tissue viability (SpectraMax M3, Molecular devices).

Field Emission scanning electron microscopy (FESEM)

FESEM was performed using S-4800 ultrahigh resolution SEM (HITACHI, Japan). The trans-well inserts membranes with the KCs monolayer cultured in static or flow were cut and dehydrated using ethanol (19J214027 VWR) (30%, 50%, 70%, and 100% dilution). For each dilution the membranes were incubated for 10 min, followed by drying using Hexamethyldisilazane (H4875 Sigma Aldrich) for another 10 min. The samples were sputtered with a 6 nm layer of Au/Pd using Leica EM ACE600. An accelerating voltage of 2 kV and a working distance of 10-15 nm were used.

Immunostaining and confocal analysis of whole skin samples

The list of antibodies, their dilution and product description is provided in **Supplementary Table S4.3**. For full model immunostaining, the fabricated skin tissues were fixed with 4% Paraformaldehyde (PFA)

for 20 minutes. The tissues were washed with PBS twice. Then, 0.1% Triton-X was added for 10 minutes.

After washing twice with PBS, the tissues were incubated with 2% BSA solution at room temperature (RT) for 1.5 hours. PECAM-1 (or CD31) glycoproteins on the endothelial cell surface were detected using mouse anti-human PECAM-1 primary antibody in PBS (1:50) for overnight at 4ºC followed by washing with PBS (3 times, with 5 minute interval). Then, anti-mouse Alexa 594 secondary antibody (1:200) was added and the tissues were then incubated for 2 hours in RT. After washing with PBS (3 times, with 5 minute intervals) the tissues were placed on a glass slide for confocal microscopy (Leica TCS SP8). Samples were observed for PECAM+ vessels using an excitation wavelength of 594nm (red), actin cytoskeleton using an excitation wavelength of 488nm (green) and Fluorescent microbeads (blue) using an excitation wavelength of 405nm. Images were taken at a resolution of 1024×1024 pixels using either 10X dry objective, 20X Oil immersion objectives or 63X Oil immersion objectives depending on the experimental requirements. The confocal images of vessels were fed into Angiotool software and the vessel area was analyzed according to software instructions.[171]

KCs monolayer culture under flow

For 2D monolayer study, 2×10^5 human KCs were seeded on 0.2 mg/ml FN coated trans-well inserts and incubated in *growth media* for 24 hours. The trans-well inserts were then transferred to the bioreactor and subjected to a flow of 5 mL/min for 3 days. Static KCs monolayer was incubated with media changes on the lower compartment of the insert every day. Cells were harvested from the device, washed with PBS, fixed and stained for actin, Focal adhesion kinase (FAK) and DAPI.

Immunostaining and confocal analysis of monolayer KCs

The list of antibodies, their dilution and product description is provided in **Supplementary Table S4.3**. For 2D KCs monolayer experiments, fixed cells were washed twice with PBS, treated with tritonX-100 for 5 minutes and washed twice with PBS. Samples were then blocked using 3% BSA in PBS. Samples were incubated with primary antibodies for FAK-protein overnight at 4°C. Secondary antibody to FAK (anti-rabbit 488, 1:100) and TRITC-phalloidin (Merck Millipore, 1:500) were added to samples for 2 hours at RT. Samples were washed twice with PBS and stained with DAPI (1:1000,) for 5 minutes and washed twice with PBS. The trans-well membrane containing KCs monolayer was removed from the insert using a scalpel, transferred to a cover-slip and analyzed. The cell count and FAK intensity were calculated in the Fiji (ImageJ) software.[172]

Immunostaining of cryo-sectioned samples

The list of antibodies, their dilution and product description is provided in **Supplementary Table S4.3** Samples embedded in Tissue-Tek O: C: T: (Sakura, Leiden, The Netherlands) were sectioned and stained with haematoxylin and eosin (H&E). Cryo-sectioned tissues were fixed in acetone and stained for 1h with the mouse anti-human FLG monoclonal antibodies (Santa Cruz Biotech). FN was stained 1

hour with mouse anti human fibronectin (1:200, Sigma F7387) Goat anti-mouse IgG Alexa Fluor 488-conjugated secondary antibody (Molecular Probes) was added as a secondary antibody. Stained sections were visualized using a fluorescent microscope with digital photo documentation (DISKUS; Hilgers, Konigswinter, Germany).

Trans-epithelial electrical resistance (TEER) evaluation

The TEER was measured using Evom2 Volt/ohm meter (World Precision Instruments) with the use of adjustable width double electrode. TEER readings were conducted on day 14 and day 21. The vHSEs were removed from the flow device, placed in a 24-well corning plate and washed with PBS twice. Then fresh 650 µl PBS was added to the basal side of the trans-well and 250µl of PBS on the apical side. The electrodes were sterilized with ethanol and equilibrated in PBS before use. The kΩ cm^2 was calculated by multiplying the obtained resistance value with the trans-well area (0.33 cm^2).

VEGF Enzyme-Linked Immunosorbent Assay (ELISA)

Cell culture supernatant from KC+ and KC- models were collected after days 10,14, 21 and 28, in triplicates and centrifuged in 2000 RPM, 10 minutes (at 4 ºC). The supernatant was then utilized to perform the ELISA as per the manufacturer´s protocols. The final protein concentrations were determined at 450nm (SpectraMax M3, Molecular devices).

Cell viability assay

The cell viability (XTT assay) was conducted on coated and uncoated fibroblasts. Briefly, 1×10^4 coated and uncoated cells were seeded on a 96-well plate in triplicates. The cells were cultured for 3 and 5 days at 37ºC and 5% CO_2 with media changes every alternate day. XTT cell proliferation kit (ATCC) was used and procedures were followed based on the manufacturer´s instruction. The absorbance of each condition was read at 450 nm with a reference of 650 nm (SpectraMax M3, Molecular devices)

Transport of Fluorescent Microspheres through vessels

The tissues were fixed with 4% PFA and stained with PECAM-1 and Actin cytoskeleton. A 100µl drop of 2.5wt % Fluorescent beads of size 2µm (1:10 dilution in PBS) was pipetted on top of the basal side of the tissue. After 10 minutes of incubation time, the surface of the tissue was carefully washed with PBS and fluorescent beads that entered the vasculature were visualized through a confocal microscope.

RT-PCR analysis

Total RNA was isolated from static and flow vHSEs. Whole tissue was lyzed using a tissue lyzer II (Quiagen) in a lysis buffer of Nucleospin RNA Kit (Macherey-Nagel, Duren, Germany). The quantity of the RNA was measured (NanoDrop Technologies, Wilmington, DE, USA), and the integrity was confirmed (Agilent 2100 Bioanalyzer; Agilent Technologies, Palo Alto, CA, USA). Purified RNA was reverse transcribed into cDNA using the SuperScript VILO Mastermix (LifeTechnologies, Langenselbold, Germany), according to the manufacturer's instructions. Quantitative real-time (qRT)

PCR analyses were performed on an ABI Prism 7300 Sequence Detection System (Applied Biosystems, Weiterstadt, Germany) using Assays-on-Demand gene expression products (Applied Biosystems) for human HIF1A (HS00153153_m1, VEGFA (HS0090055_m1), FLG2 (HS00418578_m1), MMP2 (HS00234422_m1), MMP10 (HS00233987_m1), FLG (HS00856927_g1), COL1A1 (HS00164004_m1), FN1 (HS00365052_m1), TIMP1 (HS99999139_m1), TIMP2 (HS00234278_m1), TIMP3 (HS300165949_m1), TIMP4 (HS400162784_m1) according to the manufacturer's recommendations. An Assays-on-Demand product for HPRT (Hs99999909_m1) was used as an internal standard.

Gene Chip analysis

For microarray analysis, purified mRNA was amplified, labeled and hybridized to Human Clariom S Array, according to the manufacturer's instructions. Data were analyzed using GeneSpring GX 14.9 software (Agilent Technologies, Frankfurt am Main, Germany). The gene ontology (GO) of the upregulated and the downregulated genes were performed using GOrilla online database.[173] The GO terms were fed to REVIGO application to omit redundant GO terms. 2000 upregulated DEGs were added to the STRING online software (http://string-db.org) to construct the protein-protein interaction (PPI) network and subsequently imported to the Cytoscape software version 3.8.1.[174] Using the MCODE application (degree cut-off 2, Node score cut-off 0.2), the top three significant modules from the PPI were identified and the GO process pathway of each cluster was noted in the Cytoscape software.[174, 175]

Laser irradiation to administer wound

The vHSEs were cultivated for 7 days in static and subsequently irradiated with an Er:YAG laser (MCL31 Dermablate, Asclepion LaserTechnologies GmbH, Jena, Germany). The laser setting was fluence per pulse 10 J/cm^2, 4 pulses (40 J total fluence), pulse duration 300µs, coverrate 10%. Laser irradiation was applied after the removal of cell culture media. After the irradiation, the models were cultivated in fresh *differentiation media* and were harvested on day 3. For static culture, the media was changed every day.

Statistical analysis

Experiments were performed in triplicates unless specified. Data are expressed as mean ± standard deviation (SD) or confidence interval (CI) depending on the respective experiment. Non-parametric two-tailed Welch-test or Anova two-way analyses with Tukey's test were used to determine the statistical difference between experimental groups. The p-values are indicated in the graphs.

4.3. Results and discussion

Development of scaffold-free vHSEs

Normal human dermal fibroblasts (NHDFs) were coated with a nano-film of ECM moieties using layer-by-layer deposition of Fibronectin (FN) and Gelatin (G). The cell-coating technique relies on the binding of cell surface integrin to FN and the interaction of FN with G.[94] To analyze the layer-by-layer deposition of FN and G complex, QCM-D experiments was conducted on gold-coated sensors. The sensors were alternately exposed to 0.04 mg/ml FN and G for nine FN-G alternate steps. A FN/G-coating thickness of approximately 30 nm on the sensor surface was observed **(Figure 4.1a, b)**. On the contrary, FN-only coating without G did not lead to the layer-by-layer deposition of ECM complexes **(Figure 4.1a, b)**. The coating technique requires multiple centrifugation steps that could affect cell viability. To test this, a cell viability assay on coated and uncoated NHDFs was conducted. It was noted that the viability of cells on days 3 and 5 post-coating, was comparable to that of the uncoated cells **(Figure 4.1c)**.

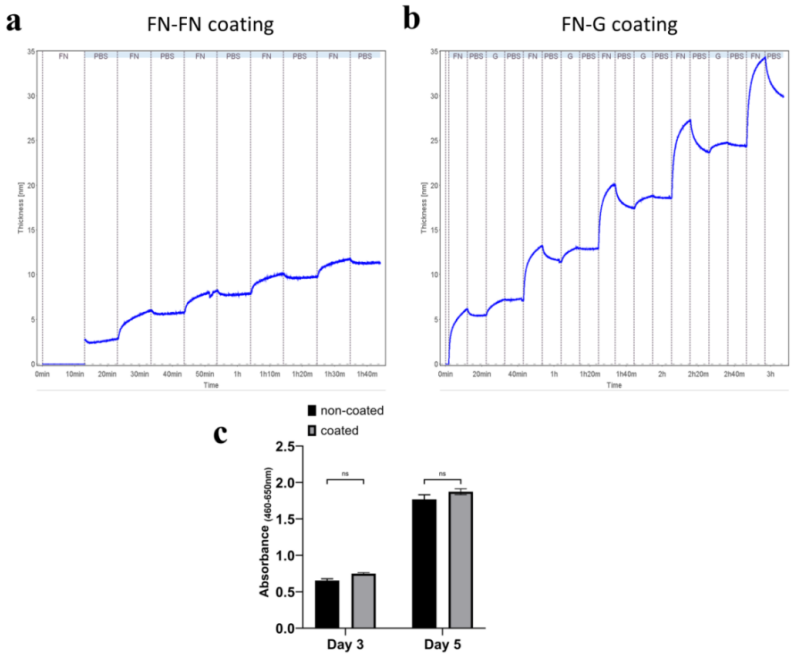

Figure 4.1 *a, b) QCM-D experiment showed increase of coating thickness in FN-G coating as compared to FN-FN deposition. c) Cell viability assay (3 biological replicates) conducted between coated and uncoated fibroblasts showed a non-significant difference in viability. Analysis used was unpaired two-tailed t-test with Welch's correction.*

Next, to construct the vascularized dermal tissue, the coated-NHDFs were mixed with ECs (in 5:1 ratio) and accumulated in a FN-coated cell culture insert. Human KCs were added on top of the formed dermal compartment to achieve the full-thickness vHSEs. The vHSEs were cultured in a static condition at an air-liquid interface (ALI). The tissues were then maintained in *differentiation media* **(Supplementary Table S4.1)** to facilitate KCs differentiation.

Sprouting vessels that spanned the entire dermal tissue construct were observed on day 7 of culture **(Figure 4.3a).** The vessels were mature as observed *in-vivo* like lumen formation within the vHSEs **(Figure4.3b).** To visualize the ultrastructure of the vHSEs, transmission electron microscopy (TEM) images of the vHSEs cultured for 7 days were analysed **(Figure 4.2).** Multiple epidermal layers and the dermal-epidermal junction (DEJ) were observed **(Figure 4.2a, b).** Strands of collagen fibrils could be detected in the DEJ. BVs with lumen surrounded by fibroblasts and the deposited ECM was observed **(Figure 4.2c, d).** ECs tight junctions were observed that show high vessel integrity. Around the BVs, sites of ECM degradation were also visible **(Figure 4.2e, f).**

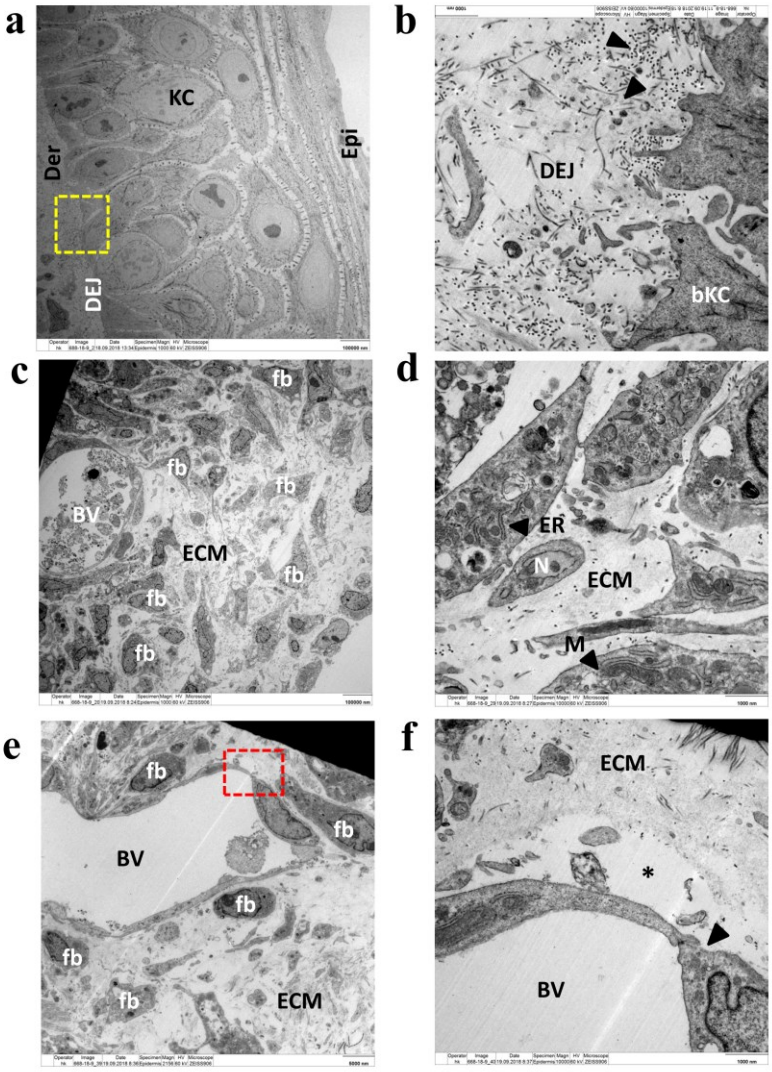

Figure 4.2 Ultrastructure of vHSEs: *Skin models were cultivated for 7 days. a) Overview of the epidermis (Epi) showed structured keratinocytes (KC) and dermis (Der). The Dermal-epidermal junction (DEJ, yellow box) is expanded in (b) which shows collagen deposition (black arrow) and the basal keratinocytes (bKC). c) Overview of the dermal compartment consisting of blood vessels (BV) lumen with supporting fibroblast (fb) and fb released extracellular matrix (ECM). d) Magnified image of fb and ECM within the dermis, nucleus is denoted as N. e) Overview of the BV shows open lumen*

and endothelial cellular junction (yellow box). f) Magnified image exhibits an endothelial cell junction (arrow). The asterisk (*) denotes degradation of the ECM surrounding the BV.

Following this, the period of the vHSEs culture was increased to 14, 21, and 28 days to obtain long-term vHSEs. However, degradation sites characterized by open spaces (devoid of cellular components) spanned the dermal compartment of the vHSEs on days 14 and 21 **(Figure 4.3c)**, and an increased disintegration of the dermal compartment was observed on day 28 of ALI culture **(Figure 4.3c)**.

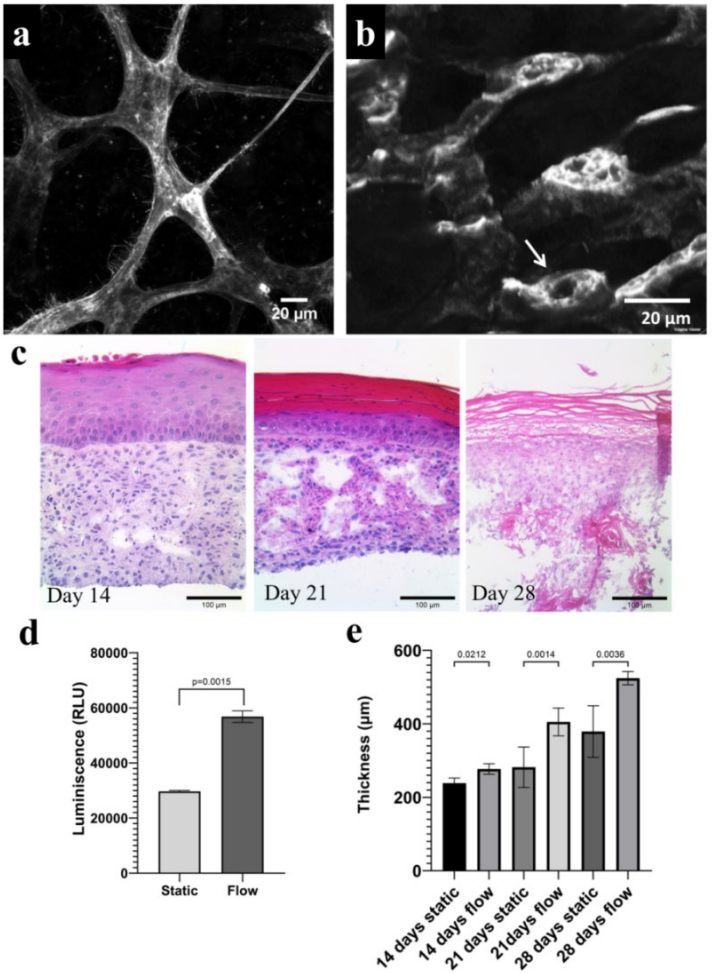

***Figure 4.3** a) Network of vessel formation on vHSEs on day 7 of static culture. b) Lumen formation observed from confocal microscopy, scale bar=20µm. c) Dermal degradation on day 14, 21 and 28 days of static culture. The vHSEs tend to completely disintegrate as time progresses, scale bar=100µm. d) Tissue viability assay shows that flow culture significantly improves the viability of the vHSEs (3 biological replications) e) Graph shows significant differences in the thickness of the vHSEs on days 14, 21 and 28 between flow and static cultures (3 biological replications, 3 measurements per replicates). Analysis used was unpaired two-tailed t-test with Welch's correction.*

Such degradation sites were previously absent up to the 7-week culture of scaffold-free non-vascularized HSEs.[176] Therefore, it was hypothesized that the interaction between KCs and ECs could potentially be responsible for the vHSEs degradation and the subsequent tissue instability. Such

degradation sites on the dermal compartment would eventually lead to unrepairable dermal disintegration and hinder the utilization of long-term vHSEs for clinical applications.

The interplay between keratinocytes and blood vessels

To test the influence of KCs on angiogenesis within the vHSEs, the vascularized dermis with and without KCs (KC+ and KC- respectively) were cultured. A time-dependent increase in PECAM-1^{+} vessels was observed in the KC+ models, whereas the KC- models showed a stable vasculature throughout the 28-day culture period **(Figure 4.4a)**. On days 21 and 28, the KC+ tissue was entirely occupied with BVs, which coincides with the amplified dermal degradation. The vessel area percentage on day 21 and day 28 of KC+ models was significantly higher than that of KC- models **(Figure 4.4b)**. To deliberate the role of KCs on angiogenesis, soluble VEGF levels in KC+ and KC- models were determined. It was observed that KC- models showed stable VEGF readings on days 10, 14, 21, and 28, whereas, KC+ models showed a time-dependent increase in the VEGF secretion **(Figure 4.4c)**.

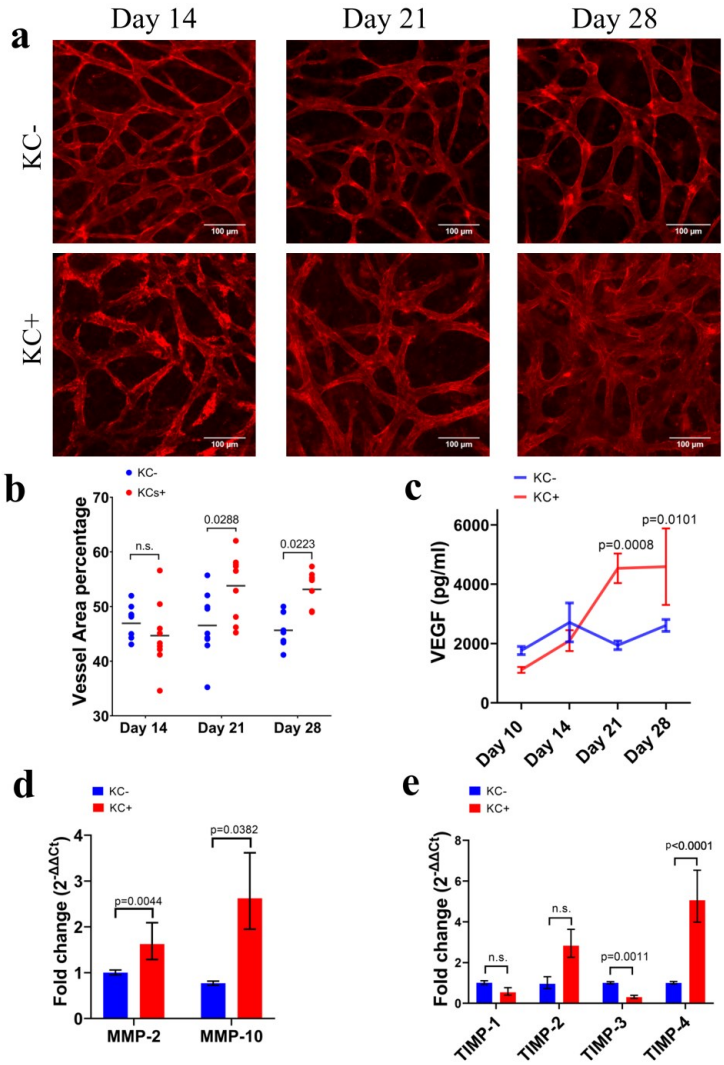

Figure 4.4 KCs influences angiogenesis and MMP/TIMPs interplay in vHSEs *a) Images show the network of vessel formation in KC- and KC+ models on days 14, 21, and 28, scale bar=100µm. b)*

Significant increase in the vessel area percentage in KC+ models on days 21 and 28 (3 biological replicates, 3 images per replicate). Data show mean values ± standard deviation (SD). The analysis used was two-way Anova with Tukey´s test. c) ELISA analysis shows a significantly increased secretion of VEGF on days 21 and 28 (3 biological replicates, data show mean values ± SD), the analysis used was two-way Anova with Tukey´s test. d) RT-PCR expression analysis of MMP-2 and MMP-10 expression exhibits a significant increase of both MMPs in KC+ models, analysis was done on day 21 models (3 biological replicates, data show mean values ± confidence interval (CI)). e) RT-PCR analysis of TIMP-1, 2, 3, and 4 expression shows a significant decrease of TIMP-3 expression in KC+ models and a significant increase of TIMP-4 in KC+ models as compared to KC- models. Studies were done on day 21 models (3 biological replicates, data show mean values ± CI). In all RT-PCR graphs, the p-values were calculated from ΔC_t values and the analysis used was an unpaired two-tailed t-test with Welch's correction.

On days 21 and 28, there was a significant difference of soluble VEGF present in KC+ models compared to the KC-model. Similar observations were reported previously in HSEs where the presence of both fibroblast and KCs led to a higher VEGF production as compared to models consisting of only fibroblasts.[177] Enhanced VEGF production elicits dissimilar responses in HSEs and vHSEs due to the absence and presence of BVs respectively. For instance, BVs exposed to VEGF becomes activated, regulates the proteinase activity, and remodel the surrounding ECM constitution.[178] Such a response is not observable in HSEs without BVs, thereby highlighting the importance of vascularization in tissue-engineered skin constructs to accurately mimic skin physiology.

Dermal degradation and the consequent instability could also be linked to the interplay between ECM proteinases such as MMPs and TIMPs.[179] To understand the impact of KCs on the MMPs/TIMPs dynamics, the gene expression of MMP-2 and MMP-10 as well as the inhibitors TIMP-1, TIMP-2, TIMP-3 and TIMP-4 were analyzed using RT-PCR at day 21 in both KC+ and KC-models. *In-vivo,* MMP-2 (also known as gelatinase A) is expressed by both fibroblasts and KCs, and MMP-10 (also known as stromelysin-2) is expressed primarily by KCs.[180] Both MMP-2 and MMP-10 have the ability to degrade several ECM proteins and subsequently lead to enhanced angiogenesis.[181] There are contradictory observations in prior HSEs that show both KCs dependent increase or decrease in MMP-2 expression.[134, 182] In observation, RT-PCR analysis indicated that there was a significant upregulation of both MMP-2 and MMP-10 in KC+ vHSEs compared to KC- vHSEs **(Figure 4.4d)**. These models comprise BVs as an additional component that in the presence of KCs could modulate MMP-2 and MMP-10 expression differently, and cannot be compared with the observations presented in prior research conducted on non-vascularized HSEs.

TIMPs on the other hand actively inhibit MMPs and are known to mediate vessel quiescence.[183] A downregulation of TIMP-1 (non-significant), a downregulation of TIMP-3 (significant), an upregulation of TIMP-2 (non-significant), and an upregulation of TIMP-4 (significant) in KC+ as compared to KC- models was observed **(Figure 4.4e)**. There are contradictory observations regarding the expression of TIMP-3 in the presence of KCs.[157, 184] Again this chapter emphasizes here that

previous studies on the expression of TIMPs in HSEs are devoid of the effect of the vasculature. TIMP-3 is unique from other TIMPs because it not only inhibits several MMPs but also prevents the binding of VEGF to the VEGF Receptor-2 (VEGFR-2), which suppresses further angiogenesis.[185] The significant downregulation of TIMP-3 in the presence of KCs could restrict MMPs inhibition and allow the enhanced VEGF interaction with VEGFR-2. Interestingly, the KC+ led to a significant upregulation of TIMP-4 as compared to KC- models **(Figure 4.4e)**. The dynamics of TIMP-4 in human skin have not yet been revealed in its entirety. Studies show that TIMP-4 is expressed in psoriatic skin and near the vicinity of some blood vessels in chronic wounds.[186] Although TIMP-4 has been shown to inhibit a wide range of MMPs, previous reports suggest that, unlike other TIMPs, TIMP-4 does not modulate angiogenesis and therefore would not affect the vasculature directly.[187]

These observations indicate that KCs and ECs in vHSEs enhance the VEGF production and modulate the MMPs/TIMPs interplay resulting in increased angiogenesis and the subsequent dermal degradation.

Flow prevents dermal degradation by regulating proteinase activity

The vHSEs were first cultured for 7 days in static conditions and then transferred to a custom-built 3D printed bioreactor until days 14, 21, and 28. The experimental overview is shown in **Figure 4.6a.** The design and the dimensions of the flow device are provided **(Figure 4.5)**. Previous studies have shown the effect of the flow culture on skin tissue viability.[188, 189] Similarly, to elucidate the role of flow on cellular nourishment, viability assays were conducted after 7 days of flow stimulation (5 mL/min flow rate). A significant increase in tissue viability in flow-stimulated vHSEs as compared to static models was observed **(Figure 4.3d)**.

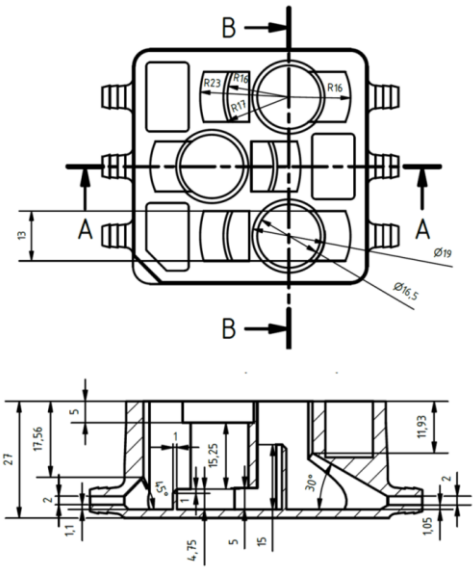

Figure 4.5 *Computer aided drawing of the bioreactor. The picture shows the top-view and the side-view of the 3D printed bioreactor. The dimensions of the flow bioreactor are depicted.*

On days 14, 21 and 28, the vHSEs subjected to flow (5 mL/min flow rate) eliminated the formation of KCs and EC mediated dermal degradation sites was observed **(Figure 4.6b, d)**. To investigate the role of flow in the modulation of MMPs and TIMPs, RT-PCR analysis of MMP-2, MMP-10, and TIMPs (TIMP-1, 2, 3 and 4) was conducted. The gene expression of flow-treated and untreated vHSEs was compared on day 21. The downregulation of both MMP-2 (not significant) and MMP-10 (significant) was observed in models exposed to flow **(Figure 4.6g)**. Therefore, it can be inferred that flow culture reduced the enhanced MMPs expression that resulted from KCs and ECs interaction in the vHSEs. In the case of TIMPs, a significant downregulation of TIMP-4, a slight upregulation of TIMP-3 (not significant), a slight upregulation of TIMP-1 (non-significant) and a slight upregulation of TIMP-2 (non-significant) was observed **(Figure 4.6h)**.

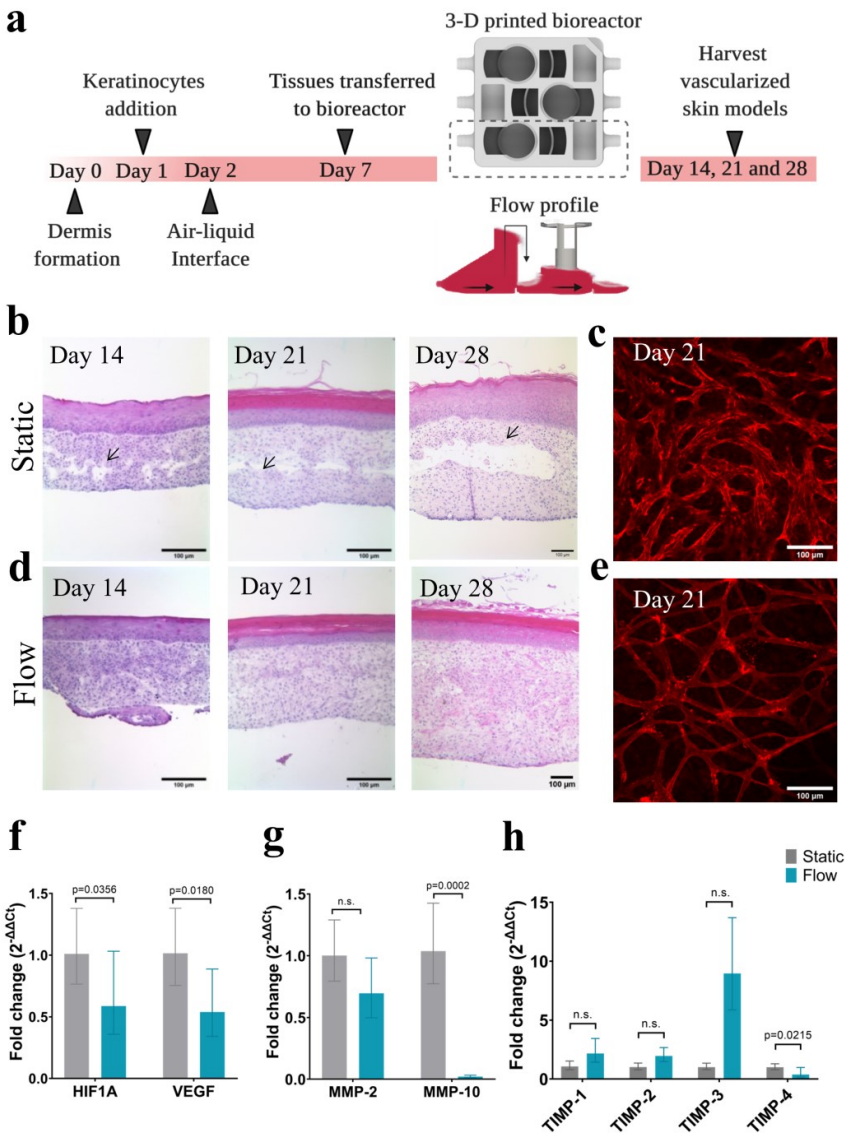

Figure 4.6. Flow culture prevents dermal degradation and controls vascularization *a) Experimental overview and the timeline of flow culture. b) H&E images show dermal degradation after 14, 21 and 28 days of static culture, scale bar=100 µm, arrow denotes the degraded dermal area. c) Confocal*

image of the vessel abnormality after 21 days of static culture, red=PECAM-1, scale bar=100 µm. d) H&E images show an absence of degradation sites at days 21 and 28 of flow culture, scale bar=100 µm. e) Confocal image of vascular network formation after 21 days of flow culture, red= PECAM-1, scale bar=100 µm. f) RT-PCR analysis of HIF1A and VEGFA expression shows a significant downregulation in flow-treated vHSEs, analysis was done on 21 days models (3 biological replicates). g) RT-PCR analysis of MMP-2 and MMP-10 expression shows a significant decrease of MMP-10 in the 21 days flow models (3 biological replicates). h) RT-PCR analysis on TIMP-1,2,3, and 4 expression shows a non-significant increase of TIMP-1, 2, and 3 in flow-treated models and a significant decrease of TIMP-4 expression in static models. Analysis was done in 21 days models (3 biological replicates). All RT-PCR data are given as mean ± CI. In all RT-PCR graphs, the p-values were calculated from ΔC_t values and the analysis used was an unpaired two-tailed t-test with Welch's correction.

The significant downregulation of TIMP-4 in the flow as compared to static culture is an interesting observation. Previously, TIMP-4 has been shown to be expressed in inflammatory cardiac diseases.[190] Future studies that involve flow culture along with inflammatory disease skin models could better elucidate the role of TIMP-4 in skin integrity. Most MMPs are not highly expressed in normal quiescent skin unless exogenous signals stimulate and activate the skin. These stimuli could be induced by wounds, skin diseases and barrier disruption, fibrosis, tumors, and photoaging. In the quiescent native skin, the MMPs, TIMPs, and angiogenic factors maintain an intricate balance that restricts dermal degradation. *In-vitro*, however, the addition of KCs on top of a dermal construct lead to enhanced proteinase activity. Such a scenario would not significantly affect HSEs (without vasculature) however, ECs within vHSEs respond to enhanced MMPs, that facilitate the release of ECM-bound angiogenic factors thereby leading to increased angiogenesis and dermal degradation. We show flow culture restored the quiescence of the formed skin model by downregulating MMPs and modulating TIMPs expression.

Next, the regulation of VEGFA and hypoxia inducible factor A (HIF1A) genes was studied. Both of these genes are known to be key players in the regulation of angiogenesis. RT-PCR analysis showed that HIF1A expression was significantly downregulated in flow-treated vHSEs as compared to static vHSEs **(Figure 4.6f)**. Interestingly, there was also a significant downregulation of VEGFA in flow-treated samples **(Figure 4.6f)**. It is known that hypoxia leads to an upregulation of HIF1A and an increase in VEGF expression.[191] A thick scaffold-free 3D tissue in static culture is hypoxic due to the presence of a large number of tightly packed cells and low media diffusion. Flow culture leads to better convection of media into the tissue, thereby reducing hypoxia. This could result in the downregulation in HIF1A and VEGFA expression. Analogous to ours, a previous report showed that osteoblasts exposed to perfusion flow for 14 days downregulated HIF1A and VEGFA.[192] To confirm that angiogenesis is regulated by flow culture, BVs architecture in both flow and static vHSEs was observed. Confocal images of 21-days vHSEs show that the vessel network and morphology were preserved in flow-treated models, whereas static culture resulted in amplified vascularization **(Figure 4.6c, e)**.

Flow enhances epidermal barrier properties and ECM deposition

Previously, epidermal barrier properties were shown to be improved in HSEs following dynamic flow stimulation.[193] To study the effect of flow culture on the barrier properties, the trans-epithelial electrical resistance (TEER) values were obtained. A significant increase was noted in the TEER values in flow-stimulated models as compared to static models after 14 and 21 days of flow culture **(Figure 4.7a)**. After 14 days of flow stimulation, an increase in TEER value was observed from 605.99±46.38 Ω cm^2 for static models to 2332.88 ± 323.12 Ω cm^2. After 21 days of flow treatment, an increase in TEER value was observed from 673.64±152.35 Ω cm^2 in static models to 2963.29±180.43 Ω cm^2 for flow-stimulated models **(Figure 4.7a)**.

To investigate further the effect of flow on KCs barrier properties the expression of FLG was examined. The skin barrier properties have also been linked to the FLG content in the epidermis.[194] The expression of FLG and FLG2 in the flow and static vHSEs was studied and a significant upregulation of FLG protein in flow-treated vHSEs compared to static vHSEs was observed **(Figure 4.7b)**. FLG is a key marker for enhanced keratinocyte differentiation and functionally relevant mutations in the FLG gene are associated with an impaired barrier function.[195] However, FLG2 expression did not show significant differences **(Figure 4.7b)**. Immunostaining of FLG protein showed increased expression in flow-treated vHSEs as compared to static vHSEs **(Figure 4.7c)**.

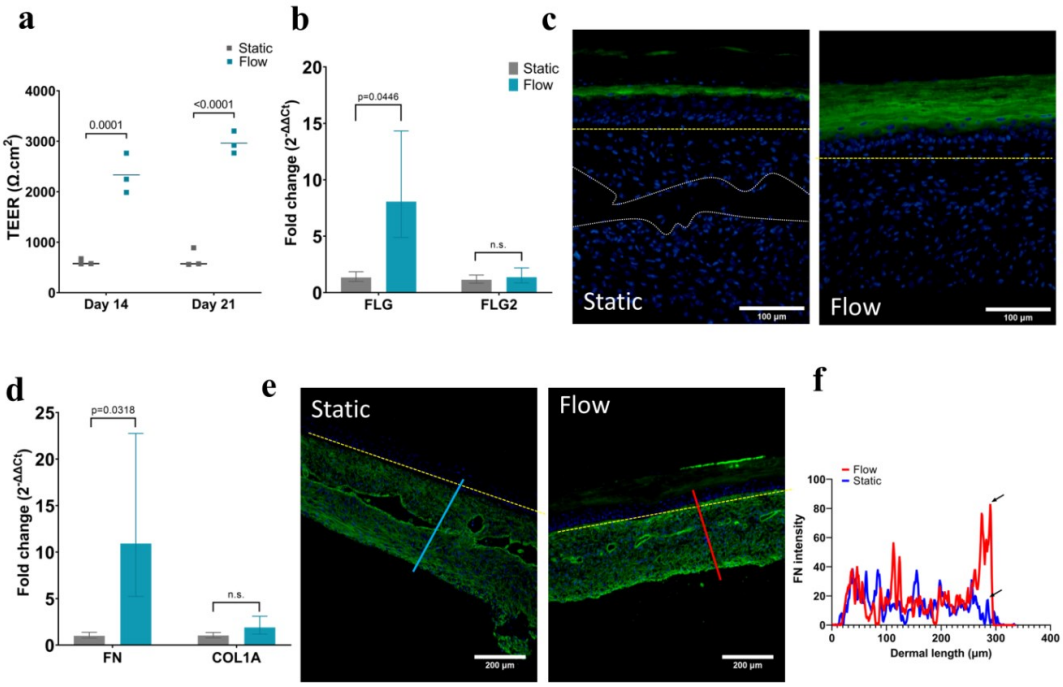

Figure 4.7. Flow culture modulates barrier properties and ECM deposition *a) TEER readings indicate a significant increase in the resistance values in flow-treated vHSEs as compared to static (3 biological*

replicates). Data are given as mean ± SD. The analysis used was two-way Anova with Tukey's test b) RT-PCR gene expression analysis of FLG and FLG2 showed a significant increase in FLG expression in flow-treated vHSEs (3 biological replicates). Data are given as mean ± CI. c) Immunostaining of FLG protein showed higher expression in flow-treated vHSEs. The yellow dotted line represents the DEJ, white dotted line indicates the dermal degradation in static vHSEs. Scale bar=100µm. d) RT-PCR gene expression analysis of FN and COL1A showed a significant upregulation of FN in flow-treated vHSEs as compared to static cultures (3 biological replicates). Data are given as mean ± CI. e) Immunostaining of FN indicated higher deposition in the basal side of the flow-treated vHSEs, scale bar=200µm. f) The graph shows a stronger FN intensity on the basal side of the flow-treated vHSEs as compared to static vHSEs. In all RT-PCR graphs, the p-values were calculated from ΔC_t values and the analysis used was an unpaired two-tailed t-test with Welch's correction.

Dermal degradation and vessel abnormality not only result due to the changes in MMPs/TIMPs expression but also could be influenced by the deposition of ECM proteins. Changes in the composition of the tissue environment and the presence of varying ECM moieties have been known to modulate angiogenesis differently.[196] It was observed that flow culture resulted in a significant increase in tissue thickness on days 14, 21 and 28 in comparison to static culture **(Figure 4.3e)**. This attributes to the higher proliferation of cells and enhanced ECM deposition due to better cell-ECM interaction under the flow conditions. Prior studies have already shown that dynamic cultures improve the deposition of ECM.[197] To test the influence of the flow culture on ECM production, gene expression analysis of the two major ECM moieties collagen1A (COL1A) and FN was conducted. Non-significant changes in the COL1A expression and a significant upregulation of FN in flow-treated vHSEs as compared to static vHSEs was observed **(Figure 4.7d)**. It has previously been shown that mechanical stimuli lead to the accumulation of FN around the cells as well as the structural alteration in FN assembly.[197] In the flow-treated models, immunostaining observation of FN showed that there was an increased deposition of FN on the basal side of the vHSEs, which was in direct contact with the flow **(Figure 4.7e, f)**.

Flow affects keratinocytes mechano-responsiveness

It was also interesting to study the influence of flow culture directly on KCs monolayer as several pre-clinical experiments demand epidermis-only models. Several reconstructed-human epidermal (RHE) models already exist commercially but are cultured in static conditions. We, therefore, tested whether the dynamic flow provided by the bioreactor influences the mechano-responsiveness of KCs. For this, a monolayer of KCs was cultured on top of a cell culture insert and exposed to 5 mL/min flow for 72 hours from the basal side.

The KC monolayer was cultured in submerged condition (not exposed to air) and calcium chloride was not supplemented in the media. This was done to delay KCs differentiation and to observe the influence solely due to the dynamic flow. No cellular disruption or detachment of the monolayer due to the media flow of 5 mL/min was observed after 72 hours.

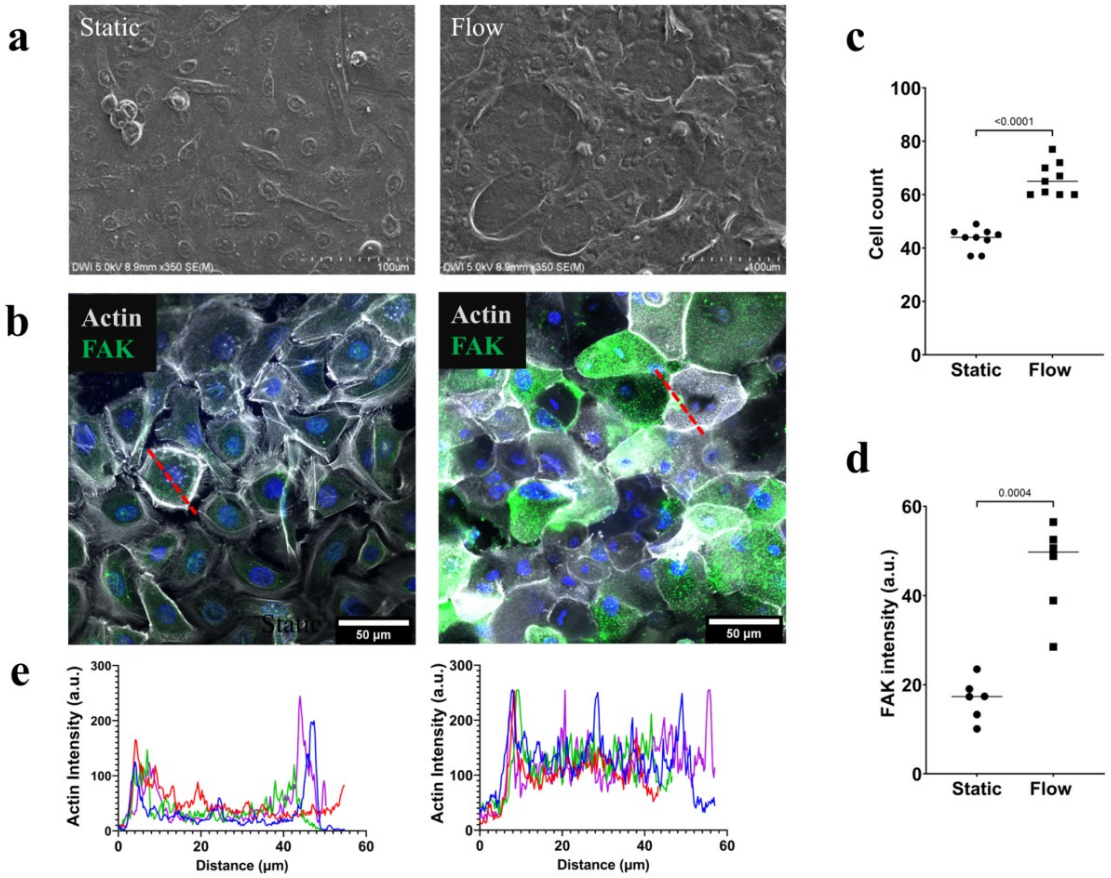

Figure 4.8. Flow culture modulates mechano-responsiveness and proliferation of KCs monolayer *a) Scanning electron microscopy images show a monolayer formation of KCs in static culture, whereas 5 mL/min flow stimulation resulted in a layered proliferation of cells. Monolayers were cultured in static or flow for 72 hours, scale bar = 100 µm. b) Confocal image depicts actin (grey), FAK protein (green), and nucleus (blue). Flow culture showed higher intensity of FAK protein and higher actin distribution in the cell cytoplasm and periphery, Scale bar = 50 µm. c) The quantification of the number of KCs showed significantly increased cell count in flow-stimulated KCs (3 biological replicates, 3 images per replicate). d) Analysis of the average FAK intensity shows significantly higher intensity in flow-treated KCs as compared to static KCs (3 biological replicates, 2 images per replicate). e) Graphs depict the intensity profile of actin from three randomly selected KCs from static and flow cultures respectively. All data are mean values ± SD; all analyses were done using unpaired two-tailed t-test with Welch's correction.*

Interestingly, multiple layers of KCs were observed after 72 hours of flow stimulation, whereas KCs in static culture remained as a monolayer **(Figure 4.8a, b)**. Intercellular space was observed in the static KCs monolayer, whereas a higher cell-cell contact in flow-treated KCs monolayers was observed **(Figure 4.8b)**.

To observe the effect of flow culture on cellular proliferation, the number of KCs nucleus (stained with DAPI) in static and flow cultures were counted. A significantly higher number of cells in flow-treated samples as compared to static monolayer was noted **(Figure 4.8c)**. Similar effects of flow culture on proliferation as well as differentiation have been previously observed in oral KCs.[198] Next, this chapter

analyzed the flow-mediated cellular actin and FAK distribution in the KCs. FAK, a tyrosine kinase receptor that links cell integrin to the actin cytoskeleton, has been previously implicated in KCs migration, spreading and activation.[199] Compared to the static culture of KCs, immunostaining analysis showed an upregulation of FAK in flow culture **(Figure 4.8b,d**). Additionally, in the static culture, actin was confined mostly to the periphery of the KCs, whereas it was observed to be distributed throughout the cell body as well as the periphery in flow-treated KCs **(Figure 4.8b, e)**. Both the regulation of FAK and actin observed in this chapter is consistent with recent reports.[200]

Formation of perfusable vessels under the flow culture

An interesting effect of flow culture on scaffold-free vHSEs was the formation of vascular openings on the basal side of the tissue that was in exposure to the flow **(Figure 4.9a)**. For the vessels to form vascular openings, the vessels must first undergo migration towards the direction of the flow followed by changes in vascular morphogenesis. Similar openings were observed in a recent study with vascularized kidney organoids under the flow culture.[201] Previous studies have shown the migration of ECs towards the perpendicular direction of the flow.[104] Therefore, a synergy of growth factor gradients, as well as the directionality of the flow perpendicular to the scaffold could lead to such vascular openings. These peripheral openings were devoid of any cellular components and it was hypothesized that such openings could be connected to vessels on the deeper layer of the skin model.

Fluorescent microbeads were introduced through the observed openings and transport of beads through the vascular openings to the interconnected apical vasculature was detected **(Figure 4.9b)**. Not a single leaked fluorescent bead was observed in the fibroblast compartment, which strengthens that the vessels have tight cellular junctions that restrict the beads from diffusing out of the vasculature. Orthogonal slices of Z-stacked images show the presence of beads within the lumen of the vessel **(Figure 4.9b).** In the future, such openings could be utilized to transport therapeutic drugs, immune cells, or cancer cells to fabricate more physiological vHSEs

Fabrication of thicker vHSEs under the flow culture

Arguably, one of the biggest challenges in lab grown tissue is mass transfer limitations, which limits the size of tissue construct. To overcome, adequate vascularization of the tissue is required. However, maintenance of the vasculature, as well as the balance of multiple intracellular signalling cascades required in the formation of well differentiated epidermis, is a challenge in conventional static culture. This is true especially in scaffold-free systems where there is increased cell-cell interaction and lower cell-cell spacing contrary to the scaffold-based models (like hydrogels), limiting the diffusion of media. It was hypothesized that the flow culture could maintain sufficient diffusion of oxygen, nutrients, and facilitate the removal of waste products to sustain thicker viable tissue.

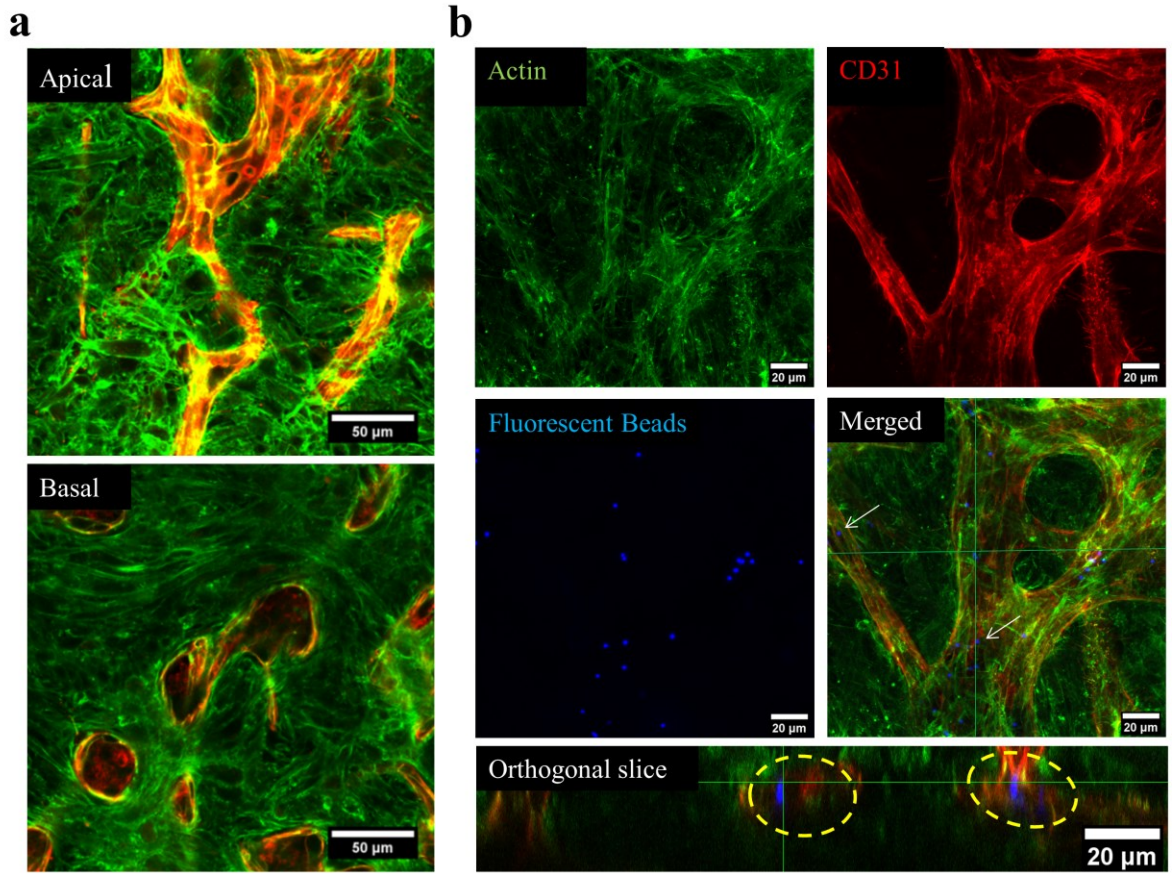

Figure 4.9 Perfusable lumen formation *a) Flow induces the formation of vascular openings on the basal side of the tissue that was directly exposed to the flow for 14 days, whereas the apical side shows intact vasculature. Scale bar=50 µm. b) Fluorescently labeled micro-beads (blue) can be observed inside the vascular lumen that depicts the interconnection of the lumen with apical vessels in the skin tissue. The representative image indicates 21 days flow-stimulated skin models that are stained with actin (green) and PECAM-1 (red) and a merged overlay image. Scale bar 20 µm. The orthogonal projection of the vasculature shows that the beads reside inside the vascular periphery (red) and are not present on the actin positive fibroblast compartment (green) that implies continuous intact vasculature. Scale bar=20 µm.*

To test this, vHSEs with double the thickness as compared to the normal vHSEs was prepared. To investigate whether the flow preserves epidermal integrity and vascular morphology. vHSEs consisting of twice the number of fibroblasts and ECs were cultivated in the flow bioreactor and compared to equally thick tissue in static culture conditions. Thirty layers of fibroblast (30×10^5 cells) and six layers of HUVECs (6×10^5 cells) per model were used to engineer the thick dermis compartment. After the addition of the KCs, the models were cultivated under the flow and static conditions for 7 days. The thick vHSEs under the flow showed a viable differentiating epidermis as well as vessel formation **(Figure 4.10a)** with an overall thickness over 500 µm, whereas, in static culture, the dermis was thin with limited vessel formation and a complete lack of epidermis **(Figure 4.10a, b)**. This could be attributed to the limited media penetration in the static model, thereby limiting the diffusion to the epidermal compartment.

One of the challenges of a scaffold-free tissue-engineered model is the formation of thick tissues. It is relatively less challenging to engineer a thick hydrogel-based model as the hydrogel itself provides nutrition to the embedded cells. Cells within the hydrogel can cleave the surrounding matrix and utilize the released nutrition. In a scaffold-free model, however, the only source of nutrition is the culture media and to a lesser extent the cell-derived ECM. This is also a primary challenge in other scaffold-free systems such as organoid and spheroid models, where the lack of nutrients in the organoid/spheroid core leads to hypoxia and cell apoptosis. In a full-thickness skin model, it becomes even more challenging as the models are cultured in ALI. Therefore, the only source of nutrition is present from the dermal side of the model. We challenged the vHSE to answer the question, whether a flow culture would be sufficient to preserve epidermal morphology in a thick scaffold-free model. For this vHSE was constructed with twice the number of fibroblasts and ECs than what we use (Section 4.2, Methods) and stimulated with flow culture. Increasing the cell number led to the formation of 500 µm thick tissue within 7 days.

Counterintuitively, KCs still differentiated into multiple epidermal layers in this thicker tissue and the ECs still formed vascular networks in thick dermal tissue which indicates that cellular nourishment within the thick scaffold-free cellular system is possible by using flow culture. In contrast, vHSE with equivalent cell density lacked differentiation of the KCs in static culture.
This flow culture system could therefore be utilized for not only skin tissues but other organ-specific thick scaffold-free tissues such as spheroids and organoids in the future.

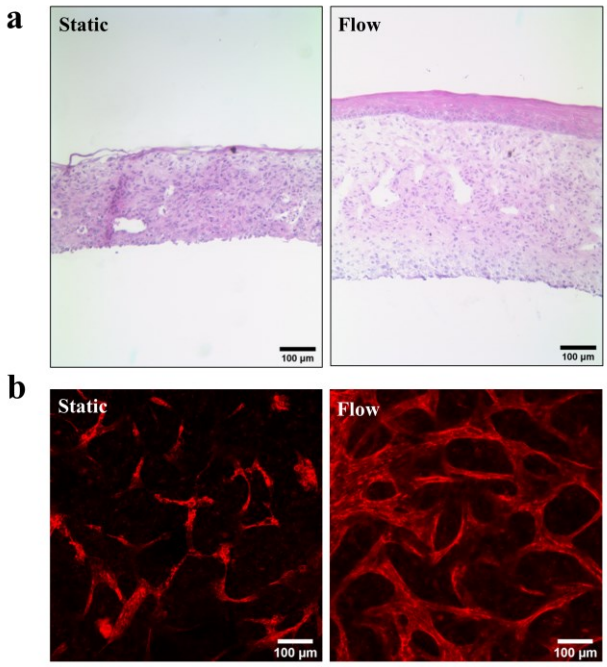

Figure 4.10 Flow bioreactor supports thick skin formation. *36 layers (30 layers of coated Fibroblast and 6 layers of HUVECs, ratio 5:1) were accumulated (2 biological replications). a) Flow of 5 ml/min showed the formation of epidermal compartment, whereas static cultures could not support epidermis*

formation. This could be attributed to better media penetration in flow culture. b) Thick tissues in flow culture possessed vascular network, whereas static culture failed to develop vasculature.

In this system, it is recognized that the influence of direct shear stress is negligible due to the presence of the trans-well insert membrane on the basal side of the tissue. Nevertheless, the pressure difference generated across the cell culture insert as well as the convective nature of flow in the bioreactor allows for improved media penetration, thereby promoting interstitial fluid flow. It should be noted that even a minimal interstitial flow rate triggers drastic vascular morphogenesis.[202] The flow simulation were conducted to deliberate the flow patterns within the reactor and into the cell-culture insert. It was observed that media penetrates through the membrane into the apical side where the vHSEs reside **Figure 4.11**.

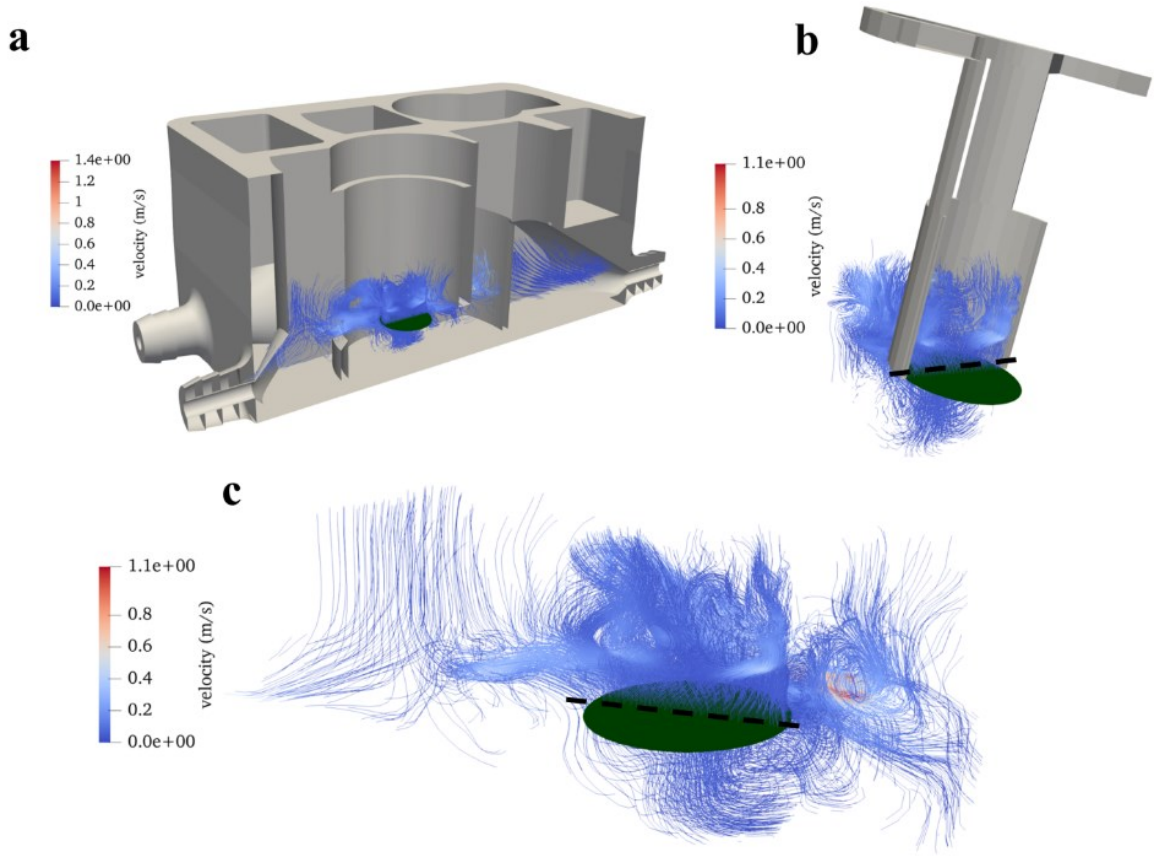

Figure 4.11. Flow streamline visualization a) *Flow streamlines in the entire bioreactor b, c) Flow streamline visualization through the cell culture insert and through the bioreactor well respectively. The flow lines are depicted near the membrane (dark green) after 79.7 secs. The simulation for the system was performed with a membrane that allows a flow rate of 5 mL/min. The value of the absolute velocity (in m/s) is colour-coded.*

It is estimated the pressure difference due to the flow in the bioreactor and the presence of the porous membrane to be 27 Pa (**Figure 4.12**).

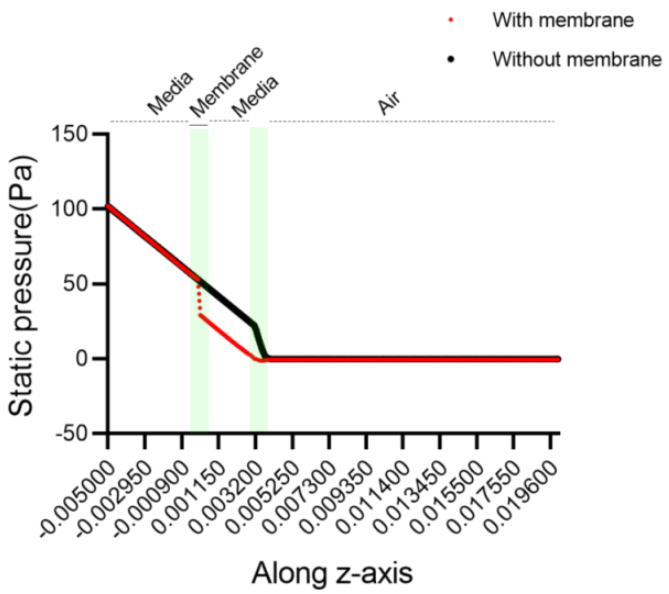

Figure 4.12. *The static pressure at the center of the bioreactor with (red) the membrane and without (black) the membrane. The pressure is calculated along the Z-axis of the bioreactor for the flow rate of 5 mL/min at 79.7 secs. The difference in the pressure across the membrane is approximately 27 Pa. In the case without a membrane, the main pressure drop takes place at the interface between media and air, while with the insert and the membrane, the main pressure drop takes place across the membrane.*

The drop in the pressure between the lower compartment of the cell culture insert and the upper compartment of the insert drives enhanced convection of media through the insert. This transport of media inwards could explain the ability of flow cultures to nourish thick tissues, morph vascular architecture, and alter several gene expressions in the vHSEs.

Flow culture improves wound healing

To demonstrate the importance of dynamic flow culture systems for clinical scenarios, a 3D wound healing assay in the absence and presence of flow was conducted **(Figure 4.13a-i)**. Conventionally, almost all wound healing assays are performed in the static culture that does not recapitulate the *in-vivo* wound healing process. The incorporation of dynamic systems is desired to understand the influence of nutrients, drugs, and oxygen penetration in wound healing, especially for acute wounds. Former studies showed that laser irradiation is a suitable tool to set multiple injuries with defined dimensions in HSEs and thus enable a standardized investigation of wound healing.[203] After laser treatment, the laser-irradiated vHSEs in static and flow culture were cultured for 3 days. It was observed that the flow-treated wound healed faster in comparison to static wounded vHSEs **(Figure 4.13f-i)**.

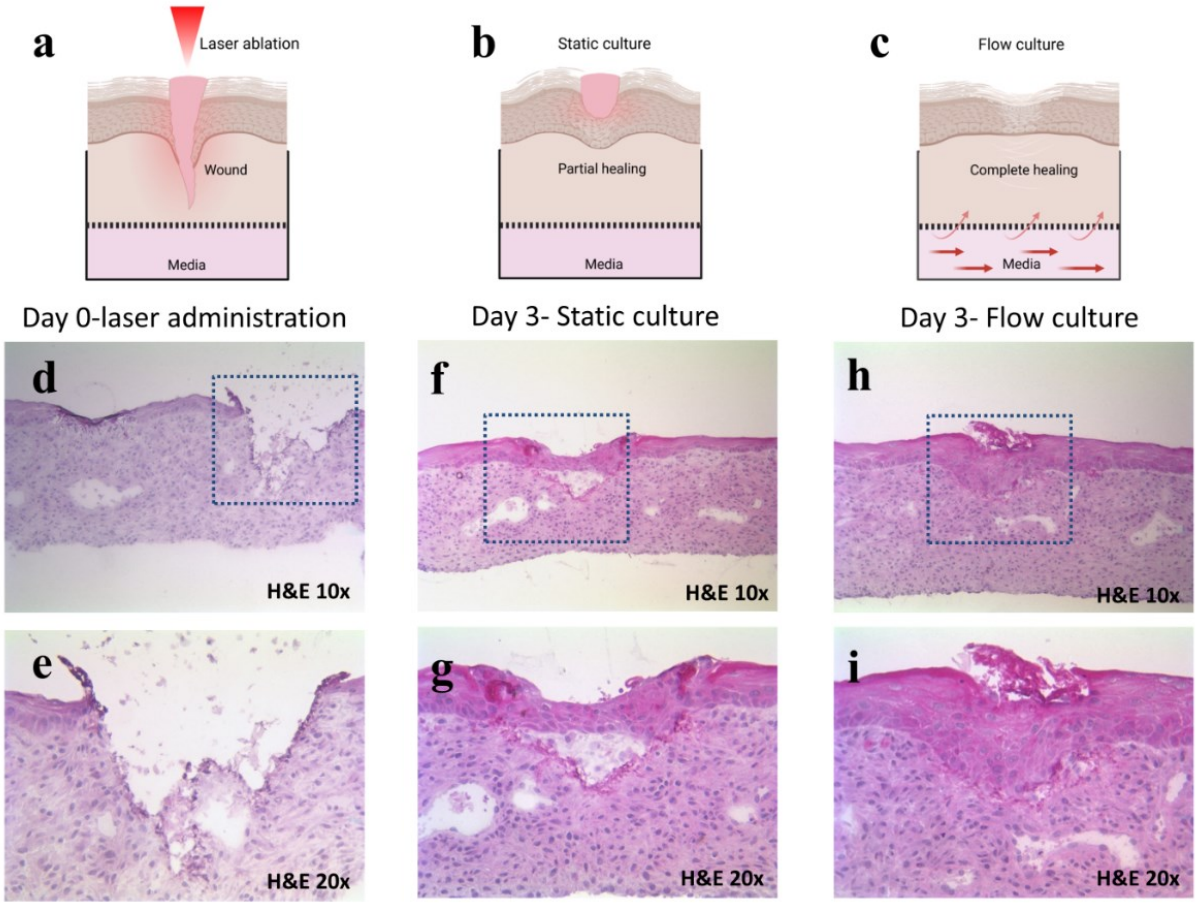

Figure 4.13. Faster wound healing in flow culture *a, b, c) Pictorial representation of the wound infliction, and healing response in static and flow. d) Wound is inflicted on the formed skin model on day 0 (H&E 10 X magnification). e) Magnified image of the blue dotted area from figure d (H&E 20 X magnification) f) Once the wound is inflicted; the vHSEs are cultured in static for 3 days (2 biological replicates). Partial healing of the wound was observed in static culture (H&E 10 X magnification). g) Magnified image of the blue dotted area from figure f (H&E 20 X magnification). h) Wounded vHSEs in flow culture showed faster and complete healing of the inflicted wound at day 3, H&E 10 X magnification (3 biological replicates). i) Magnified image of the blue dotted area from figure h (H&E 20 X magnification).*

Re-epithelialization is an important step in the healing of normal and chronic wounds. During re-epithelialization process, the basal KCs migrate and proliferate to fill the wound. This process requires the KCs to be activated and has been linked to actin remodelling and FAK signalling. Our initial observation of complete wound healing in flow-stimulated vHSEs in contrast to incomplete healing in static vHSEs provides an important discussion point and would be further explored in the future, especially with experiments involving chronic wounds. However, our initial hypothesis of the fast healing in flow culture are 1) deeper penetration of culture media nutrients in flow culture, 2) remodelling of actin and FAK in activated KCs, 3) healthier vasculature that promotes re-epithelialization, 4) faster proliferation of KCs under flow culture as shown in the KCs monolayer experiments, 5) higher ECM deposition, and 6) co-ordination of MMPs and TIMPs.

In the flow culture, the entire wound was observed to be infiltrated by KCs, which are known to play crucial roles in wound repair as structural cells and by exerting important immune functions.[204] This observation ignites the question of whether dynamic flow culture should be employed for testing in clinical applications such as wound healing assays, novel drug testing, and skin disease modeling.

4.4. Conclusion

Vascularization of tissues has been deemed as one of the major challenges in tissue engineering. This challenge is increasingly being tackled, in the case of HSEs by incorporating vascular cells, providing angiogenic factors, and utilizing techniques such as sacrificial templates, bioprinting, and self-assembly. These advancements are elaborated in detail in the described reviews.[205-208] However, an important question that pertains to the maintenance of vascularized tissues for the long term is overlooked. Especially, in *in-vitro* tissues that comprise more than two cell types, the interplay between growth factors and cytokines makes the maintenance of such tissues a highly complex endeavour. This chapter highlights the problem associated with vHSEs instability and emphasize the shortcomings of a static environment for the culture of complex *in-vitro* models. This chapter shows that a dynamic flow system can be used to maintain vHSEs for a long duration, providing a platform to model skin diseases and test novel therapies for an extended period.

4.5. Supporting Information

Table S4.1: Media composition

Media type	**Composition**
Growth media	Dermalife: EGM: DMEM- FBS 10% in the ratio of 50:35:15 and with 1% penstrep (Dermalife: complete Promocell EGM without IGF and EGF)
Differentiation media	Dermalife: EGM: DMEM- FBS 10% in the ratio of 50:35:15, with 1% penstrep, ascorbic acid 50 µg/ml and 1 mM calcium (Dermalife-without TGFα Promocell and EGM without IGF and EGF)
Dermal media	EGM: DMEM- FBS10% (50:50), 1% penstrep, Ascorbic acid 50µg/ml
Keratinocyte Growth Media	Dermalife K complete

Table S4.2: Product information

Product	**Product number**	**Manufacturer**
Gelatin	G9391	Sigma Saint Louis, US
Trans-well inserts	3470	Corning/Costar
DMEM+ Glutamax	61965-026	Life Technologies
Dermalife Keratinocytes media	LL-007	LifeLine Cell Technology
Fibronectin from human plasma	F2006	Sigma Saint Louis, US
Calcium Chloride Solution	C-34006	Promocell
Endothelial Cell Growth Medium 2 Kit	C-22111	Promocell
WT Expression Kit	4411973	Thermo Fisher
Gene Chip WT Terminal Labeling and Controls Kit	901525	Thermo Fisher
CellTiter-Glo® 3D Cell Viability Assay	G9681	Promega
Reglo Digital MS-4/6-100 pumps	ISM8336	Cole Palmer
BSA	A2153	Sigma Aldrich
Triton X	T9284	Sigma Aldrich
Human VEGF ELISA kit	KHG0111	Thermo Fischer
XTT proliferation assay kit	301011K	ATCC
MF-FluoBlue-2.0	L951-1	Microparticles GmbH

Table S4.3. List of antibodies and the dilution factors

Antibody	Dilution	Manufacturer
Anti-human mouse PECAM-1(or CD31)	1:50	ThermoFischer Scientific (MA5-13188)

Anti-mouse Alexa 594	1:200	ThermoFischer Scientific (A11005), goat
DAPI	1:1000	Molecular probes (D1306)
Anti-human FAK Primary antibody	1:100	Novus Biologicals (NPB184750, rabbit
Anti-rabbit Alexa 488	1:100	Invitrogen (A11034), goat
Anti human Filaggrin primary Antibody	1:200	Santa Cruz (sc-66192), mouse
Anti human Fibronectin primary Antibody	1:200	Sigma (F7387), mouse
Anti mouse Alexa 488 secondary Antibody	1:200	Molecular Probes (A11001) , goat
TRITC-phalloidin	1:500	Merck Millipore
Alexa Fluo 488 Phalloidin	1:500	Invitrogen (10125092)

Chapter 5

3D Vascularized Breast Cancer Models

This chapter was adapted with permission from the publication "3D vascularized breast cancer model to study the role of osteoblast in formation of a pre-metastatic niche" in *Scientific Reports*. 2021 Nov 9;11(1):21966. Copyright© 2021.
Direct link: https://www.nature.com/articles/s41598-021-01513-x. All schematics were created using Biorender.

5.1. Introduction

Breast cancer is the most frequently diagnosed cancer and the leading cause of cancer-related death in females worldwide.[209] Once the tumor metastasizes to a distant site, the 5-year survival chance decreases from ~93% to ~22% (National Cancer Institute SEER database). There are five molecular subtypes of breast cancer of which the triple negative subtype is particularly challenging.[210] Triple negative tumors represent around 15% of invasive ductal breast cancers. They display distinctive epidemiological, phenotypic and molecular features with distinctive patterns of relapse, and a poor prognosis despite relative chemosensitivity.[210] Increasing clinical evidence has suggested that the most common site of triple negative breast cancer (TNBC) metastasis is bone,[211-214] which disrupts the balance between bone formation and resorption.[215] Patients with this condition have a median survival of around 2-3 years following initial diagnosis of bone involvement.

To understand better the propensity of breast cancer cells (BCCs) to metastasize preferentially to bone, an investigation of the mechanistic pathways that drive organ-specific metastasis is crucial. Conventionally, researchers have relied on two-dimensional (2D) assays and animal models in order to study the metastatic process.[216] However, 2D models do not recapitulate the tissue architecture and the cellular interactions of the tumor microenvironment. On the other hand, animal models have failed to translate pre-clinical success to patient outcome, thereby questioning its resemblance in the cellular level to the human tissue. With animal models, it is difficult to study the interaction of specific cell types in a controlled manner thereby limiting the possibility to conduct parametric studies. Additionally, ethical issues in using animals as models for human disease exist. An alternative approach is the use of three-dimensional (3D) cultures such as hydrogels composed of either ECM molecules[217-219] or synthetic polymers,[220] scaffold-free organoids culture,[221, 222] and microfluidic chips.[223, 224]

Although there are a large number of prior studies focused on the fabrication of sophisticated 3D *in-vitro* models utilizing the above-mentioned techniques, most models are not developed for the

investigation of cancer metastasis progression. Out of the limited number of research articles that deal with breast-to-bone metastasis, the majority of these studies recapitulate the late-bone metastatic stage where the BCCs have already colonized the bone microenvironment, leading to further metastasis or dormancy.[216, 225, 226] In other words, these studies focus on post-metastatic, direct interaction between BCCs and bone. However, to understand the metastasis process in its entirety, the study of early-stage pre-metastatic progression of BCCs within the primary site is equally important.

One overlooked pre-metastatic phenomenon is the involvement of the distant secondary site in remotely regulating the primary site. Bone could act as an active participant, releasing cytokines and growth factors to the primary breast tumor site, and play a functional role in the initiation of tumor metastasis.[227] The concept that primary tumors can prime the secondary site remotely prior to the initiation of metastasis is not controversial.[228, 229] However, the reciprocal crosstalk from the secondary site, although understudied, could also influence changes in the primary site. It is intriguing to note that high bone mineral density (BMD) in postmenopausal women has been linked with an increased incidence rate of breast cancer.[230, 231] Furthermore, it was shown that low levels of bone turnover proteins c-terminal telopeptide (CTX1, bone resorption marker) and osteocalcin (bone formation marker), independent of BMD, correlated with increased breast cancer risk in postmenopausal women.[232] Although these phenomena are not fully understood and require further investigation, it begs the question of whether the bone can indirectly, via release of soluble factors, lead to breast cancer initiation and progression.[227]

To mimic this early-stage pre-metastatic cross-talk scenario *in-vitro*, there is a need to develop a 3D indirect culture protocol where the secondary and primary sites are not in direct contact but interact via indirect paracrine signaling. Due to the lack of such models and protocols, the study of organ specificity (organotropism) observed in metastasis remains a challenge and several open questions like the role of future secondary sites in conditioning the primary tumor persists. The goals of our study were therefore to engineer a 3D vascularized breast cancer tissue (VBCTs) representing the primary tumor site indirectly co-cultured together with OBs, representing the secondary site. We further strived to study whether and how this indirect interaction with bone cells could lead to alterations in the primary breast tumor microenvironment. Therefore, a quad-culture system was developed consisting of TNBCs (MDA-MB231), fibroblasts, and endothelial cells (HUVECs) for indirect co-culture with OBs, the bone-forming cells. We opted for a scaffold-free model system due to its several advantages over scaffold-based models.[233] To engineer the scaffold-free models, we utilized layer-by-layer ECM coating and accumulation technique.[94] This technique allowed the formation of thick vascularized tissues and provided a microenvironment to the cancer cells with enhanced direct cell-cell interactions.[94, 234] Fabrication of the models in cell-culture inserts allowed easy handling and the indirect interaction of the formed VBCTs (within the insert) with the OBs (on the well plate).

We show the formation of a vascularized breast cancer model using MDA-MB231 and the influence of OBs on the VBCT morphology, vasculature and gene expression. Furthermore, the effect of blood vessels (BVs) on the model in presence of OBs was elucidated. We observed that the morphology of MDA-MB231 changes significantly in 3D scaffold-free tissues as compared to 2D cultures. Following this, we investigated the influence of OBs and MDA-MB231 on the tissue vasculature. Finally, utilizing gene microarray analysis, the indirect paracrine effect of OBs on the VBCTs was studied. Since vascular re-modeling is one of the first steps in the initiation of a pre-metastatic niche, we also studied the influence of BVs in the breast cancer tissues co-cultured with OBs. Important hub genes and highly interconnected PPI clusters were identified to understand the influence of OBs and BVs in the VBCTs.

In short, we fabricated a simple and realistic biological system that was utilized to understand the influence of the secondary bone site on the primary breast cancer microenvironment. This system, in the future, could be used to dissect the role of secondary tumors that drives breast cancer organotropism.

5.2. Methods and Materials

Cell culture and media condition

Green fluorescence protein (GFP^+) MDA-MB231 cells were kindly provided by Dr. Julia Steitz, Institute of Laboratory Animal Science, RWTH University Hospital, Aachen, Germany. The cells were cultured in DMEM (11965092, Thermofisher Scientific) with 10% fetal bovine serum (FBS). Osteoblasts were procured from Sigma Aldrich (406-05F), and cultured in Osteoblast growth media (417-500, Sigma Aldrich). Fibroblasts were obtained by isolation of skin biopsies that were surgically extracted from healthy volunteers (Department of Dermatology, RWTH Aachen University Hospital, Germany). The extraction and isolation were conducted in accordance with the Declaration of Helsinki principles and was approved by the ethical committee of RWTH Aachen University Hospital, Germany. Fibroblasts were cultured in DMEM with 10% FBS. HUVECs (Lonza, Passage <4) were cultured in an endothelial growth medium (C-22111, Promocell). For the culture of VBCTs, DMEM: EGM (1:1) with 10% fetal bovine serum (FBS, Biowest) and 50 µg/ml Ascorbic acid (A92902, Sigma) was used.

Migration assay

OBs (passage<5) were cultured in 24 well plates (7×10^4 cells) and allowed to cultivate for a day. MDA-MB231 cells were cultivated in serum-free DMEM media for 24-hours. Required number of cells was treated with 25 µg/ml AMB3100 (EMD Millipore) for 1 hour. Cell culture inserts (8µm pore size, Corning) were pre-treated with DMEM medium for 2 hours prior to cell addition. 1×10^4 treated or untreated MDA-MB231 cells were added to the upper compartment of the 8µm pore size cell culture inserts in 250 µl of serum-free DMEM (with 0.1%BSA) whereas 600 µl of serum-free DMEM (with 0.1% BSA in media) was added to the lower compartment. After 1 hour of attachment time, inserts were transferred into the well plate containing OBs and fresh media was added. CXCL12 (Sigma,

SRP3276) in serum-free DMEM media was added to appropriate chambers depending on the experimental requirement. After 18 hours of the assay, the lower compartment was stained with DAPI and images were taken in a fluorescent microscope (10X magnification). Three separate regions were selected per insert. Experiments were done in triplicates.

XTT assay

5×10^4 fibroblasts, HUVECs or MDA-MB231 cells were seeded on 96-well plates. In each cell conditions, 0 ng/ml (vehicle: DMSO), 50 ng/ml and 100 ng/ml of CXCL12 were added for 24 hours in respective serum-free media (0.1% BSA). XTT (11465015001, Sigma) was utilized as per the manufacturer´s protocol. The specific absorbance at 460 nm was observed and the unspecific absorbance at 630 nm was subtracted.

ECM-coating and accumulation to fabricate cancer models

Fibroblasts were coated layer-by-layer using ECM coating and accumulation technique as previously described.[94] Briefly, fibroblasts were exposed to 0.04 mg/ml FN (sc-29011A, SCBT) and 0.04 mg/ml G (G9391, Sigma) solutions with an intermediary PBS washing step. After 9 steps of alternate exposure to FN and G, the coated cells were mixed with HUVECs in 15:2 ratios and 2.5×10^4 GFP+ MDA-MB231 were mixed with the HUVECs and coated fibroblasts. The models were cultured for 24 hours in 0.4 μm pore sized inserts (3470, Corning) and the inserts were transferred to well plates containing OBs. Prior to the fabrication of models, 7×10^4 OBs were seeded on 24-well plates and cultured for 2 days.

To fabricate 3D models comprising of MCF-7 and MDA-MB468, we mixed coated fibroblasts with HUVECs (15:2 ratio) and 2.5×10^4 MCF-7 or MDA-MB468 depending on the required model. Both the breast cancer cell lines were first live stained with CellTracker ™ Red CMTPX Dye (C34552, Invitrogen) for 20 minutes according to the manufacturer's protocol and then subsequently mixed with fibroblasts and HUVECs. The models were cultured for 72 hours with media changes every day.

Immunostaining of tissues

Tissues were extracted out of the cell culture insert, washed twice with PBS. The harvested tissues were fixed in 4% PFA for 30 minutes at room temperature (RT). The tissues were washed and suspended in 0.1% Triton-X 100 for 10 minutes. The unspecific antibody binding was blocked by suspending the tissue in 3% BSA (Sigma, Germany) in PBS for 1.5 hours in RT. After PBS wash (2X), mouse anti-human CD-31 primary antibody (MA5-13188, Thermofischer Scientific, 1:100 dilution in PBS) was added to the tissue and incubated overnight in 4ºC. After 24 hours, the tissues were washed with PBS (3X, 5-minute interval in the shaker) and goat anti-mouse Alexa 594 (A11005, Invitrogen) 1:200 dilutions was added for 3 hours in RT. Tissues were washed with PBS (3X, 5-minute interval in shaker). The tissues or 2D MDA-MB231 were further stained with DAPI (1:1000, 5-minute incubation in RT) if required. Finally, the samples were prepared for confocal microscopy (Leica TCS SP8).

Microscopy and image analysis

Stained VBCTs were extracted from the cell culture inserts, fixed on a glass slide and investigated under the confocal microscope. Samples were observed for vessels (CD31) using an excitation wavelength of 594nm (red), GFP^+ MDA-MB231 using an excitation wavelength of 488nm (green) and DAPI (nucleus) with an excitation wavelength of 405nm. Images were taken at a resolution of 1024×1024 pixels using either 10X dry objective, 20X Oil immersion objectives or 63X Oil immersion objectives depending on the experimental requirements. Vessels were analyzed for vascular density, area percentage and junction point using Angio-Tool as per software instruction.[171] All illustrations in the paper were made using Biorender.com

ELISA

The cancer models were cultivated with and without OBs for 7 days with alternative day media changes. Media was harvested and centrifuged (1500 RPM, 10 minutes, 4ºC) and the supernatant was collected. The Human VEGF165 Standard ABTS ELISA Development Kit (900-K10; Peprotech) and ABTS ELISA Buffer Kit (900-K00; Peprotech) were used as per manufacturer´s protocol. Human IL-6 ELISA development kit (900-M16; Peprotech) and Human CCL2 ELISA development kit (900-M31) were used together with ABTS ELISA Buffer Kit (900-K00; Peprotech) as per manufacturer´s protocol.

Gene chip microarray

To generate amplified sense-strand cDNA, 300 µg purified mRNA of each model were processed using the WT Expression Kit (Ambion, Austin, TX, USA). Affymetrix® GeneChip® WT Terminal Labeling Kit Assay (Affymetrix, Inc., Santa Clara, CA, USA) was used for fragmentation and labeling. Prepared hybridization cocktails were applied to Clariom™ S assay (Thermo Fisher Scientific). The assays were washed and stained using the GeneChip® Fluidics Station 450 (Fluidics Protocol FS450_0001). Arrays were scanned using Affymetrix GeneChip® Scanner 3000 7G controlled by GeneChip® Operating Software (GCOS) version 1.4 to produce CEL intensity files.

Gene analysis and gene ontology

The raw CEL files were analyzed using TAC (Applied Biosystems) and subsequent normalization was performed as per software instruction. The expression values were observed and the upregulated genes with fold change ≥2 and P value<0.05 and downregulated genes with fold change ≤-2 and P value<0.05 were chosen for further analysis. The gene ontology of the acquired DEGs was performed in Metascape (http://metascape.org). [235] The DEGs were fed into the online system and the pathway analysis was conducted utilizing a combination of GO Biological Processes, KEGG Pathway, Reactome Gene Sets and WikiPathways. Ontology terms with a p-value < 0.01, a minimum count of 3, and an enrichment factor > 1.5 were considered. The volcano plots were constructed using VolcaNoseR.[236]

PPI network analysis and prediction of hub genes

The entire upregulated or downregulated genes were fed into STRING online application that predicts the PPI network.[237] A medium confidence score of 0.4 was selected. The formed PPI network was uploaded to the Cytoscape software (version 3.8.1).[174] The hub genes from the entire network were obtained by the Cytohubba application.[238] The top nodes were ranked utilizing the MNC network scoring method.

Obtaining highly interconnected clusters

To obtain the clusters, the genes were fed to the MCODE app in the Cytoscape software.[175] The degree cut-off was selected as 2, node cut-off score as 0.2 and K-score as 2. The clusters with a MCODE score greater than 10 was selected. The functional enrichment analysis was conducted in Cytoscape where Reactome pathways were selected.

Expression analysis and survival plots

The gene expression analysis was performed in GEPIA2 with p-value cut-off of 0.05.[239] BRCA and Basal-like/Triple negative datasets were selected. The disease free survival (DFS) was analyzed for the hub genes using median cut-off (cut-off high 50%, cut-off low 50%) in GEPIA2 application.[239] DFS were plotted specifically by utilizing a subtype filter that only selects TNBC patients for the analysis. We omitted subtypes human epidermal growth factor receptor (HER2+) luminal, luminal A and luminal B for the construction of the survival plots.

Statistics

Statistical analyses were performed using GraphPad Prism 9.0.0 software. All experiments were performed in triplicates. Data are presented as mean ± standard deviation unless otherwise stated. Data are analyzed using one-way ANOVA with Tukey´s multiple comparison test. Significance was considered when $p < 0.05$. Individual p-values are stated in the graph.

5.3. Results

Formation of 3D vascularized breast cancer tissues

To fabricate the scaffold-free breast cancer model, we utilized the layer-by-layer ECM coating and accumulation technique. Normal fibroblasts (NFs) were coated with fibronectin (FN) and gelatin (G) proteins to form nano-layer of ECM moieties around the cells.[176, 228] The coated individual NFs were mixed with HUVECs and MDA-MB231 BCCs followed by accumulation in a cell-culture insert. We observed that MDA-MB231 morphology was altered in 3D scaffold-free tissues as compared to 2D culture **(Figure 5.1a, b, e)**. We observed that the BCCs interacted with the BVs either by extending along the vascular length or by remaining in a circular morphology in direct contact with the BVs **(Figure 5.1c, d)**. Majority of the BCCs showed an extended morphology and elongated filopodia in the vascularized 3D culture **(Figure 5.1b, c, e)**. Similar filopodia structures in MDA-MB231 BCCs were

observed previously in a 3D collagen matrix.[240] We quantified the BCCs aspect ratio and circularity and noted that the BCCs morphology in 3D ranged from low (circular) to high (elongated) while BCCs in 2D flat surface did not demonstrate elongated morphology **(Figure 5.1f, g).**

Recently, it was shown that MDA-MB231 morphology fluctuated depending on the ECM composition of the substrate.[241] The presence of FN led to an increase in the formation of tunnelling nanotubes, whereas the presence of Matrigel led to highly elongated cell morphology.[241] Furthermore, MDA-MB231 morphology has been shown to change drastically in collagen substrates of varying concentrations suggesting that the morphology is highly dependent on its surrounding microenvironment.[241]

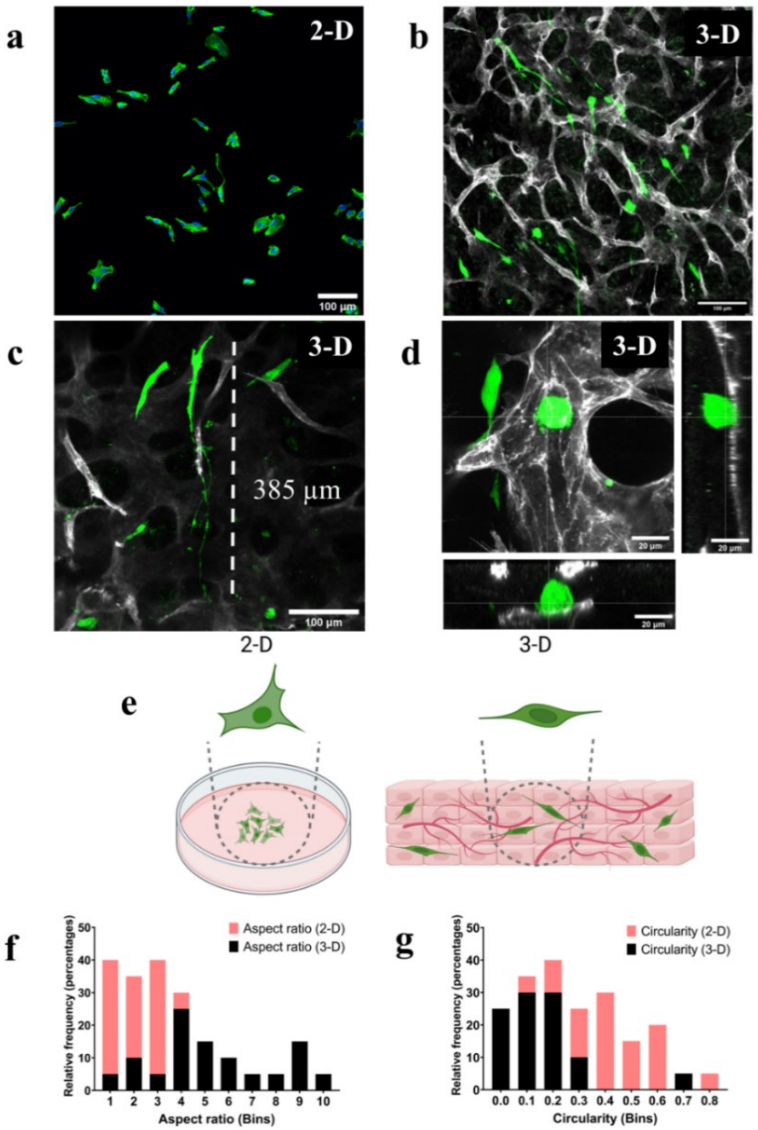

Figure 5.1 Formation of in-vitro vascularized breast cancer tissue *a) Morphology of GFP⁺ MDA-MB231 (green) in 2D cell culture plate, Scale=100 µm b) morphology of GFP⁺ MDA-MB231 embedded in scaffold-free vascularized tissue, vessels were stained (grey) with PECAM1 (CD-31), Scale=100 µm c) highly elongated BCCs filopodia observed in 3D tissues wrapped around a vessel*

branch, Scale=100 µm d) direct interaction between cancer cells and BVs, orthogonal projections are shown e) Pictorial representation of the change of morphology of MDA-MB231 in 2D culture and 3D scaffold-free culture f) cell aspect ratio in 2D is in the lower range as compared to cells in the 3D models that range from low to high (data from randomly selected 20 cells from 3 samples) g) cell circularity (1=circular, 0=elongated) analysis show that cells in 3D tend to be more elongated as compared to 2D cultures (randomly selected 20 cells from 3 samples).

Since our model is comprised of cell-secreted ECM rather than preferentially pre-selected ECM hydrogels with designated concentration, we believe that the scaffold-free models depict an unbiased tumor-microenvironment and therefore predict better the *in-vivo* cellular morphology.

In order to validate the scaffold-free *in-vitro* model for a broad utilization in cancer research, we screened for additional breast cancer subtypes and observed their morphology within the 3D microenvironment **(Figure 5.2a-f)**. Two distinct cell lines MCF-7 and MDA-MB468 were selected. MCF-7 is a non-triple negative BCCs and MDA-MB468 is a commonly studied TNBCs. Epithelial-like MCF-7 are estrogen receptor positive BCCs and are known to self-assemble into groups and subsequently form a tumor mass in 3D cultures.[242] The MCF-7 cell morphology was visualized in both 2D **(Figure 5.2a)** and 3D culture **(Figure 5.2b, c)**. Although the cell morphology was observed 72 hours post-seeding, we could visualize assembled pairs and groups of multiple MCF-7 BCCs residing within the 3D tissue **(Figure 5.2b, c)**. Next, the MDA-MB468 morphology was visualized in both 2D **(Figure 5.2d)** and 3D culture **(Figure 5.2e, f)**. TNBC-line MDA-MB468 displayed rounded and isolated single-cell morphology within the 3D tissue **(Figure 5.2e-f)**. Similar morphological observations of MDA-MB468 have been previously reported in collagen-based 3D scaffolds.[243] These morphological observations set a preliminary understanding of the influence of 3D scaffold-free microenvironment on distinct breast cancer cell-lines and displays the potential applicability of such models for the formation of diverse breast cancer tissues.

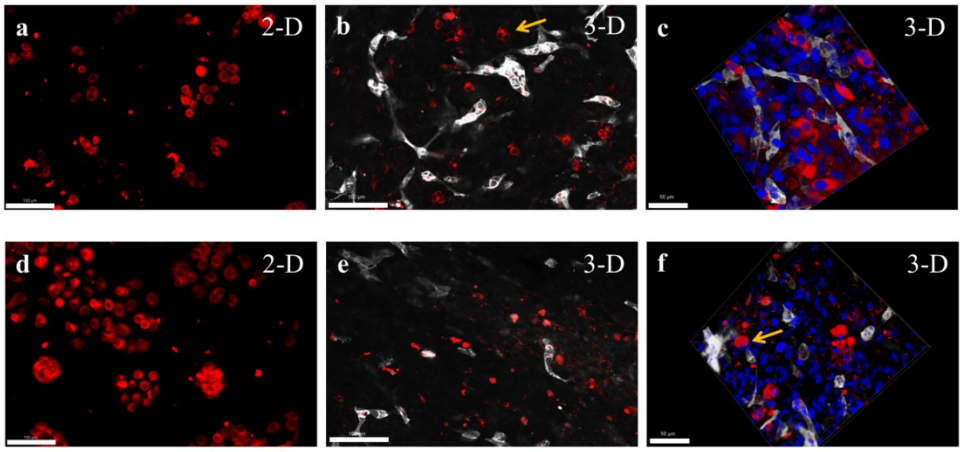

Figure 5.2 Formation of vascularized 3D models with different breast cancer cell types *a) Morphology of non-triple negative MCF-7 BCCs (red) in 2D cell culture plate, Scale=100 µm b) morphology of MCF-7 BCCs embedded in scaffold-free vascularized tissue, vessels were stained (grey)*

with PECAM1 (CD-31), arrow indicates grouping of MCF-7 cells that forms tumor clusters, Scale=100 µm c) 3D z-stacked image of MCF-7 within a vascularized tissue highlights its morphology, Scale=50 µm d) Morphology of triple-negative MDA-MB468(red in 2D culture, Scale=100 µm e) MDA-MB468 display isolated and rounded morphology within scaffold-free vascularized models f) 3D z-stacked image of MDA-MB468 and the vascularized 3D tissue, arrow highlights the rounded morphology within the vascularized model, Scale=50 µm.

Presence of MDA-MB231 and OBs modulates vasculature

Firstly, to confirm that the OBs seeded on the well plate **(Figure 5.3f)** can influence the BCCs within the cell-culture insert, we conducted a 2D migration assay to observe the migration of BCCs due to OBs. We noted an enhanced migration of MDA-MB231 cells in the presence of OBs or 100ng/ml C-X-C-chemokine ligand 12 (CXCL12) **(Figure 5.3a-g)**. Previous studies have shown that the positive-feedback loop initiated by the C-X-C chemokine receptor type 4 (CXCR4), highly expressed in malignant BCCs, to the CXCL12 expressed in bone lead to breast cancer migration.[244, 245] We noted that the pre-treatment of BCCs with CXCR4 antagonist AMD3100 (25µg/ml) restricted this migration of BCCs towards both OBs and CXCL12 **(Figure 5.3d, e, g)**. Therefore, we confirmed that cell culture inserts could be utilized for indirect co-culture assays where the secreted factors of one cell could influence the other cell type.

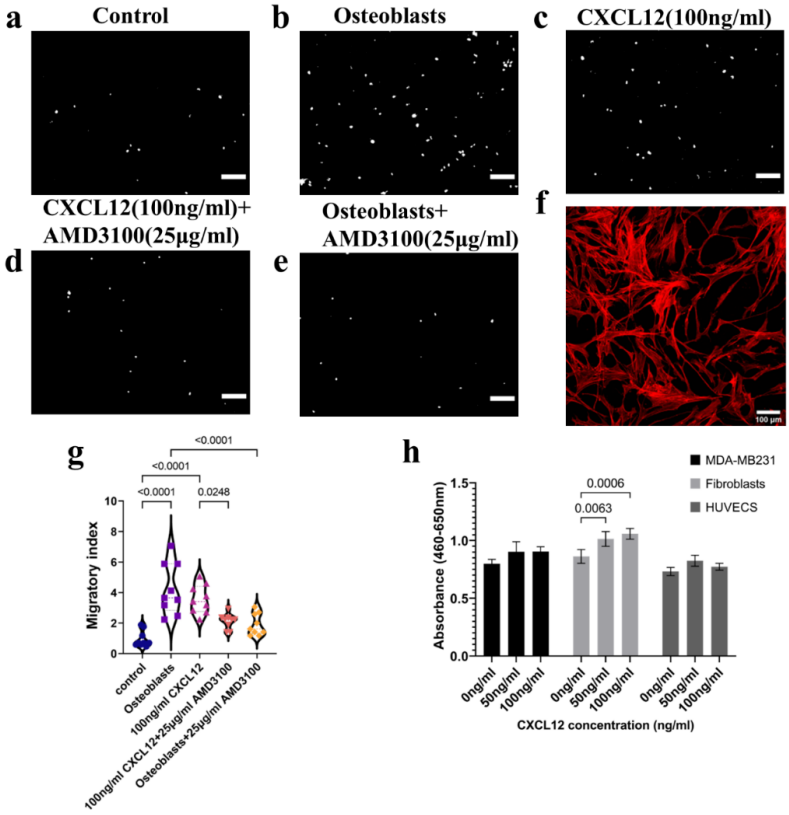

Figure 5.3. *Migration of MDA-MB231 in a) Serum free media (control), b) Presence of osteoblasts in the well-plate in serum-free media c) Presence of 100 ng/ml of CXCL12 at the bottom of the insert in serum-free media d) Pre-treated MDA-MB231 with 25 µg/ml AMD3100 slower migration towards CXCL12 e) Pre-treated MDA-MB231 with 25 µg/ml AMD3100 slower migration towards osteoblasts,*

scale bar=100 µm f) morphology of OBs on the well plate, scale bar=100 µm) g) significant difference in migration of MDA-MB231 in media vs osteoblasts and media vs CXCL12 added in the bottom, significant difference in migration observed after pre-treatment with AMD3100 towards osteoblasts and CXCL12 (n=3, with 3 different regions of the image) h) XTT assay shows slight increase in absorbance values in BCCs and HUVECs treated with 50 ng/ml and 100 ng/ml of CXCL12 and significant increase in Fibroblasts treated with 50 ng/ml and 100 ng/ml CXCL12 (n=3). Statistics used was ordinary one-way Anova with Tukey test.

Following this, we fabricated the VBCTs within the insert and seeded OBs on the bottom of the well plate to study the influence of OBs on vascularization of the tissue. A schematic illustration of the setup is shown in **Figure 5.4a**. For testing the effect of BCCs and OBs on vessel fate, four conditions were tested namely vascularized non-cancerous tissue (NH), vascularized tissue with MDA-MB231 (NHM), vascularized non-cancerous tissue indirectly co-cultured with OBs (NHO) and, vascularized tissues with MDA-MB231 indirectly co-cultured with OBs (NHMO). For clarity, the conditions and their cell constituents are summarized in **Table 5.1**.We observed that the NH and NHO tissues formed an organized vascular network, whereas NHM and NHMO models showed abnormal vascularization with disorganized architecture **(Figure 5.4b)**. A pictorial representation is shown in **Figure 5.4c.** We noted that the vessel area percentage and junction density was significantly lower in NHMO samples as compared to NH and NHO samples **(Figure 5.4d, f)**. Similarly, the average vessel length was significantly lower in NHMO as compared to NH and NHO **(Figure 5.4e)**. The average vessel length was also lower in NHM as compared to NH **(Figure 5.4e)**.

Table 5.1 List of different tissue conditions

Abbreviation	Fibroblasts (N)	HUVECs (H)	MDA-MB231 (M)	Osteoblasts (O)
NH	+	+	-	-
NHM	+	+	+	-
NHO	+	+	-	+
NHMO	+	+	+	+
NMO	+	-	+	+
OBs	-	-	-	+

These readings indicate that in a scaffold-free system, the inclusion of BCCs leads to detrimental alterations in the surrounding vasculature and this process is accentuated when the cancerous tissue is exposed indirectly to OBs.

To further understand the influence of OBs and BCCs derived soluble factors on angiogenesis, we conducted the VEGF-ELISA on day 7 of culture time. Previous reports have indicated that the VEGF levels in the intra-tumoral region of TNBC tissues were significantly higher than non-TNBC tissues.[246] Elevated VEGF level in breast cancer patients has also been linked to diminished progression-free survival and overall survival of the patient.[247] OBs have also been shown to be a source of VEGF, particularly during bone repair.[248] We observed the highest VEGF secretion in NHMO condition followed by NHM, NHO, NH and OBs respectively. VEGF levels from NHMO were significantly different to those from NHM, NH, NHO, NH and OBs **(Figure 5.4g)**. VEGF levels from NHM were significantly different to NH and OBs while NHO was significantly different to OBs **(Figure 5.4g)**. We can therefore conclude that the presence of MDA-MB231 in the *in-vitro* tissue led to increased production of VEGF, and the indirect co-culture with OBs elevates the VEGF levels.

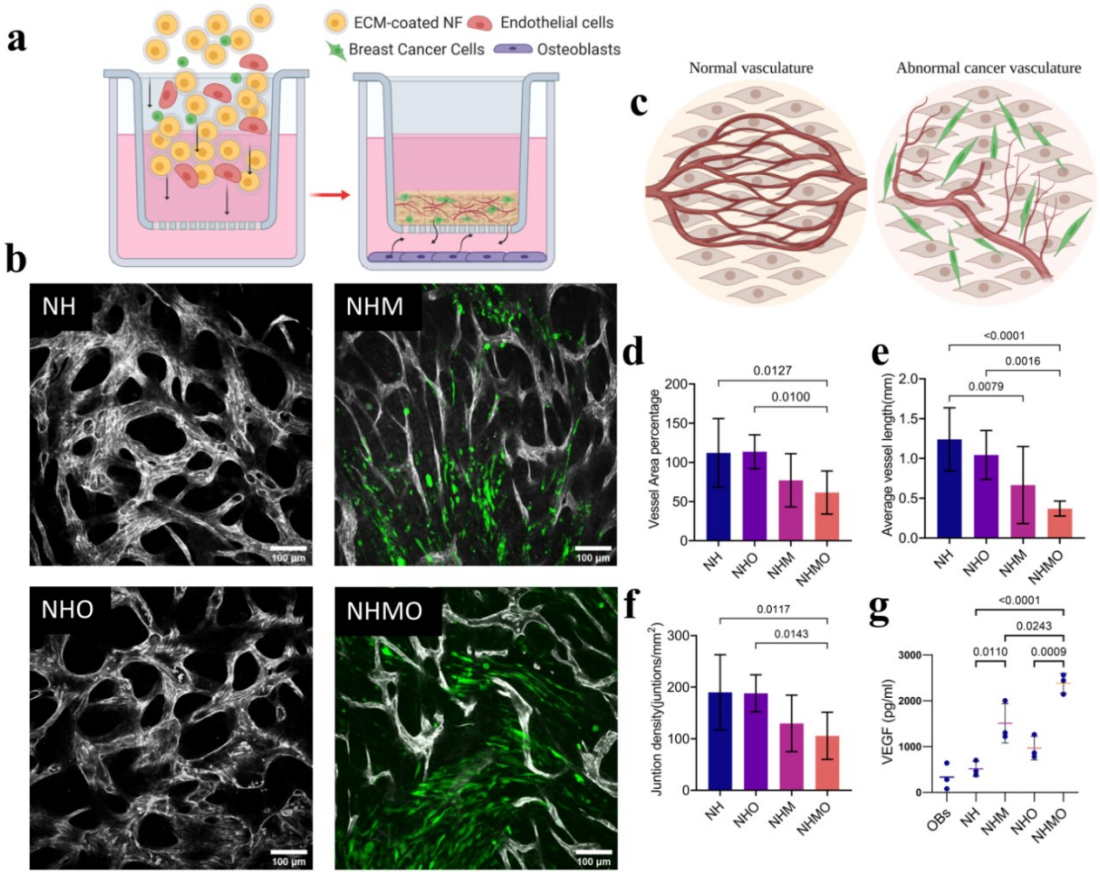

Figure 5.4 Influence of BCCs and OBs on blood vessel architecture *a) Schematic overview of the indirect co-culture experiment and the interaction of several cell types b) Confocal images of tissues (BVs morphology was monitored after day 7 of culture). BVs were observed in NH, NHM, NHO, and NHMO tissue samples. Vessels were stained with PECAM-1 (grey) and MDA-MB231 (GFP^+, green). Scale bar=100 µm. c) Schematics show abnormal changes of BVs in the presence of MDA-MB231. OBs accentuated the abnormality of the BVs d) Analysis shows a significant decrease in vessel area percentage in NHMO samples as compared to NH and NHO samples (n=3, with 3 different tissue area per sample) e) significantly decreased average vessel length (mm) in NHMO as compared to NH and NHO, and significantly decreased vessel length in NHM as compared to NH, (n=3, with 3 different*

tissue area per sample), f) significantly decreased junction density in NHMO as compared to NH and NHO, (n=3, with 3 different tissue area per sample) g) VEGF analysis shows a significant difference in VEGF levels between NH and NHM, NHO and NHMO, and NH and NHMO, VEGF level in OBs monolayer alone was statistically different to NHM, NHO and NHMO but not significantly different to NH (p-values not shown for graph simplicity), (n=3). Values in all the graphs are mean ± standard deviation; analysis was done using ordinary one-way Anova.

In the present cancer model, the vessel area percentage or junctional density in the vascularized tissue did not correlate with the increase in VEGF levels. Instead, we observed segmented, constricted and abnormal BVs in the presence of MDA-MB231 that led to the decrease in vascular density.

The current cancer model comprised BCCs distributed randomly within the 3D tissue. To better deliberate the interaction of BCCs and the vasculature, we fabricated a separate model where cancer cells were seeded on top of the vascularized tissue construct instead of being randomly distributed **(Figure 5.5a)**. As the MDA-MB231 cells were grouped in a single layer, it was expected that the direct interaction of BCCs with the vascular bed beneath would better demonstrate the fate of vessels. At the intersection between cancer cells and vasculature, we observed bright PECAM-1^{+} spots that indicated broken or open vascular ends **(Figure 5.5c)**. Magnified images of the spots showed that the open vascular ends have thin irregular sprouts protruding out of them **(Figure 5.5b, d)**.

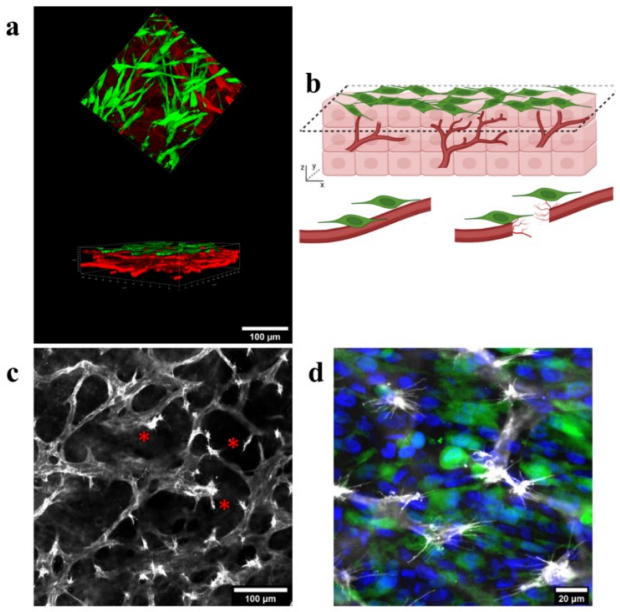

Figure 5.5 *a) Top view and side view of MDA-MB231(green) seeded on top of vascularized tissue (BVs= PECAM-1 stained red), scale=100 µm b) schematic illustration of the fate of vessels in direct contact with BCCs c) confocal images show broken vascular endpoints when in contact with MDA-MB231 cells, scale=100 µm d) magnified image shows the endpoints with sprouts (vessels= PECAM-1 stained, false colored gray, MDA-MB231=green), scale bar=20 µm*

In order to further deliberate the paracrine interaction between the VBCTs and OBs, we conducted Interleukin-6 (IL-6) and CC-motif chemokine family (CCL2) ELISA after day 7 of culture time **(Figure**

5.6a, b). CCL2, also known as MCP-1 (Monocyte Chemoattractant protein-1) is observed in prior studies to be overexpressed in tumor and the surrounding stroma.[249] CCL2 is known to have an influence in bone remodelling and angiogenesis.[250, 251] We observed that the CCL2 levels were not significantly different between NHM and NHMO **(Figure 5.6a)**. Furthermore, there was no significant difference between NH and NHM, or NHM and NHO. It is to be noted that the presence of BCCs in the tissue slightly increases (non-significant) the soluble CCL2 levels as compared to conditions without BCCs. We could however observe a significant difference between NHMO and NH, and NHMO and NHO indicating that the presence of both MDA-MB231 and OBs in the *in-vitro* system leads to elevated levels of CCL-2 **(Figure 5.6a)**.

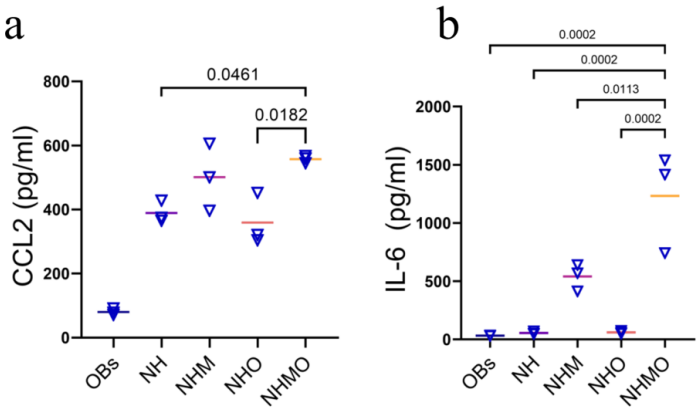

Figure 5.6 Analysis of CCL2 and IL-6 *a) CCL2 analysis shows a significant difference in CCL-2 levels between NH and NHMO, NHO and NHMO, (n=3) b) Analysis of IL-6 levels by ELISA show significant difference in IL-6 detection between only OBs and NHMO, NH and NHMO, NHM and NHMO, NHO and NHMO. Values in all the graphs are mean ± standard deviation; analysis was done using ordinary one-way Anova.*

In prior research, IL-6 has shown to have clinical significance in breast-to-bone metastasis, and anti-IL6 therapies has been investigated.[252] Furthermore, IL-6 also influences the vasculature by regulating VEGF and disrupting pericytes coverage of blood vessels in the tumor microenvironment.[253] We observed a significant increase in IL-6 levels in NHMO condition as compared to NH, NHO, and NHM. This observation indicates that the presence of both OBs and MDA-MB231 lead to enhanced levels of IL-6. Together, we show via VEGF, CCL2 and IL-6 level analysis, the paracrine interaction between different cell types in the constructed *in-vitro* model system.

OBs modulates gene expression in VBCTs

Our next focus was to elucidate the influence of OBs on the tumor tissue. VBCTs were cultured indirectly with OBs for 7 days and subsequently harvested. Gene microarray analysis was conducted to identify differentially expressed genes (DEGs) and crucial hub genes. We analysed the DEGs between NHM and NHMO samples to elucidate the influence of OBs on the VBCTs. Upregulated genes (Fold change, FC ≥2, p<0.05) and downregulated genes (FC≤-2, p<0.05) were selected as the significant DEGs.

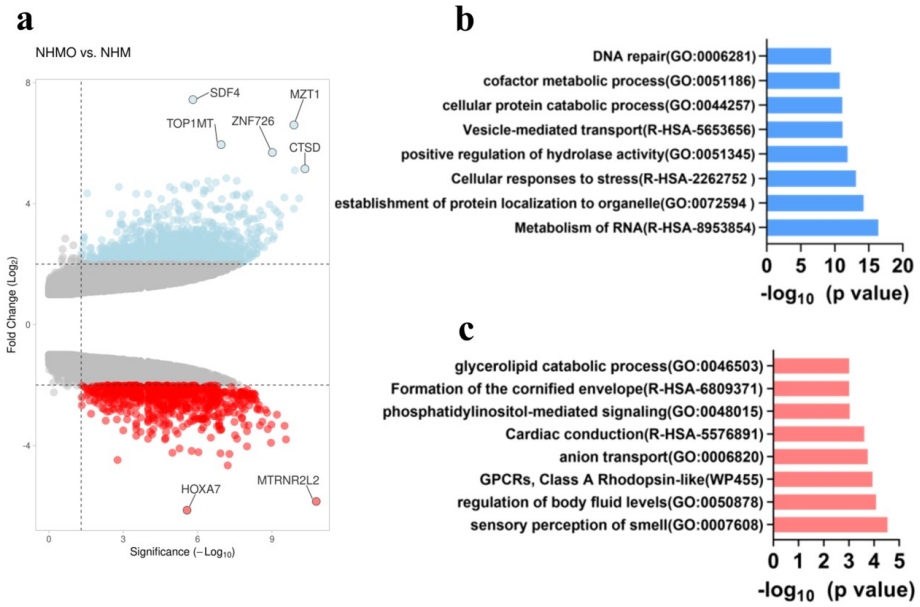

Figure 5.7a) *volcano plot depicts differentially expressed genes in NHMO vs NHM (red=downregulated, blue=upregulated) b) top upregulated gene ontology terms c) top downregulated gene ontology terms*

We observed 1476 significantly upregulated genes and 775 significantly downregulated genes in models that were co-cultured with OBs. The volcano plot depicts the upregulated and downregulated genes **(Figure 5.7a)**. The top five upregulated DEGs and the top five downregulated DEGs are shown in **Table 5.2.**

The functional enrichment analysis was conducted on the upregulated and downregulated DEGs separately **(Figure 5.7b, c)**. Five top upregulated pathways were RNA metabolism, the establishment of protein localization to organelle, cellular response to stress, positive regulation of hydrolase activity and vesicle mediated transport **(Figure 5.7b)**. Five top downregulated pathways were sensory perception of smell, regulation of body fluid levels, GPCRs- Class A Rhodopsin like anion transport and cardiac conduction **(Figure 5.7c).**

Table 5.2 Top five upregulated and downregulated genes (NHMO vs. NHM)

Gene symbol	Gene name	Expression	FC	P-value
SDF-4	stromal cell derived factor 4	up	7.44	1.55E-06
MZT1	mitotic spindle organizing protein 1	up	6.6	1.31E-10
TOP1MT	topoisomerase (DNA) I, mitochondrial	up	5.95	1.13E-07
ZNF726	zinc finger Protein 726	up	5.69	9.70E-10
CTSD	cathepsin D	up	5.15	4.70E-11
HOXA7	homeobox A7	down	-6.14	2.68E-06
MTRNR2L2	MT-RNR2-like 2	down	-5.85	1.65E-11
MAGEA2	MAGE family member A2	down	-4.66	6.13E-08
A2BP1	Ataxin-2 binding protein 1	down	-4.48	0.0017
PDZK1IP1	PDZK1 interacting protein 1	down	-4.28	5.23E-08

Next, the four highly interconnected hub genes from the upregulated PPI network were identified namely heat shock protein 90N (HSP90N), CYCS, EGFR, and RPS27A. The expression of the four hub genes was tested in tumor and normal tissue database (fed into GEPIA2 application) specific for TNBC patients **(Figure 5.8a-d)**. The fold change and p-values of the upregulated hub genes are provided in **Table 5.3**.

Table 5.3. Fold change and p-values of the upregulated hub genes

Gene symbol	Gene Name	Expression	FC	P-Value
CYCS	Cytochrome C, Somatic	**Up**	**2.03**	0.0001

EGFR	Epidermal Growth Factor Receptor	**Up**	**2.28**	3.12E-05
HSP90N	heat shock protein 90	**Up**	**2.17**	1.60E-03
RPS27A	ribosomal 40S-Protein S27a	**Up**	**2.09**	1.63E-06

The result from the TNBC database indicated that HSP90N and CYCS are significantly present in the tumor tissue as compared to normal breast tissue **(Figure 5.8a, c),** and EGFR is expressed significantly more in normal breast tissue as compared to breast cancer tissues **(Figure 5.8b)**. Disease-free survival plots of the hub genes specific for TNBC patients are shown **(Figure 5.8e-h).** Out of the four hub genes, the survival plots indicated that HSP90N had a significantly unfavourable impact on the survival of the patients **(Figure 5.8g)**.

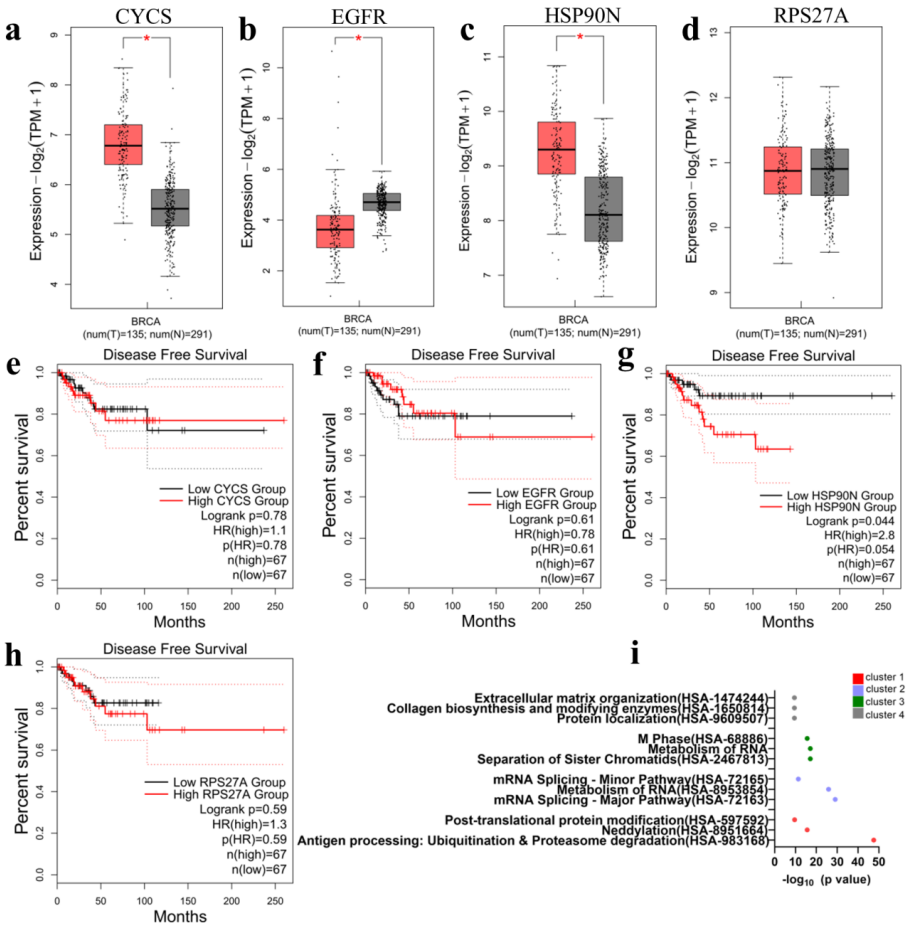

Figure 5.8. *Four upregulated hub genes CYCS, EGFR, HSP90N and RPSP27A were analyzed for their impact on patient outcome. a, b, c, d) Presence of CYCS, EGFR, HSP90N and RPS27A in tumor (red) vs normal (grey) tissue respectively (significance<0.05) e, f, g, h) Disease-free survival plots of CYCS,*

EGFR, HSP90N and RPS27A respectively i) Reactome enrichment of the clusters of upregulated genes shows four highest clusters recognized (cluster 1-4).

Endothelial cells modulate gene expression in breast cancer tissues

We sought to understand the importance of BVs in the breast cancer tissues (in the presence of OBs). Previous reports have suggested that BVs are not merely passive onlookers but active players in the metastasis process.[254] The comparison between cancerous tissues with vessels, and cancerous tissues without vessels could elucidate the influence of BVs in cancer progression. Therefore, we compared the gene expression between day 7 NHMO and NMO samples.

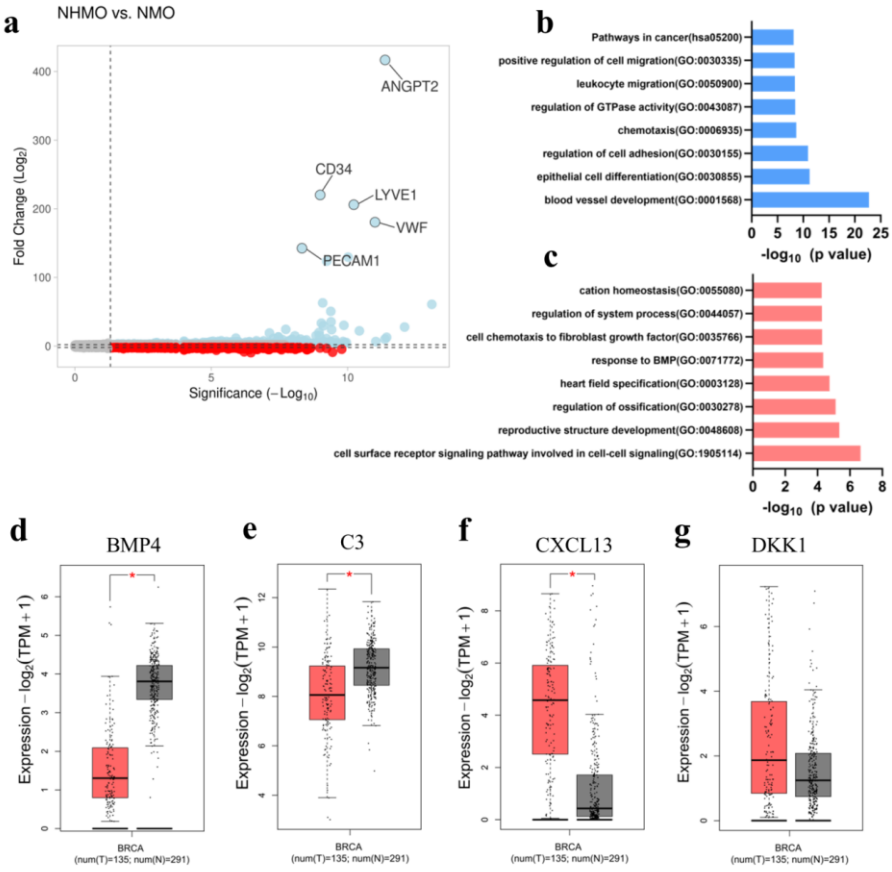

Figure 5.9 *a) volcano plot shows upregulated (blue) and downregulated (red) genes. The top five highly expressed genes are labeled b) Upregulated gene ontology terms c) Downregulated gene ontology terms d, e, f, g) Expression of downregulated hub genes BMP4, C3 protein, CXCL13, and DKK1 (red=tumor tissue, gray= normal tissue), significance <0.05.*

We observed 1278 upregulated genes and 566 downregulated genes in the presence of BVs. The volcano plot depicting the upregulated and downregulated genes is shown in **Figure 5.9a**. **Table 5.4** shows the list of the top five most highly upregulated and downregulated genes.

The upregulation of endothelial-related genes was expected as one tissue condition consisted of BVs and the other condition was non-vascularized. The ECs-related genes such as ANGPT2, CD34, LYVE1,

VWF and PECAM1 were highly upregulated in the vascularized tumor tissue as compared to non-vascularized tissue due to the presence of BVs **(Table 5.4)**.

Interestingly, several of the downregulated genes in NHMO vs NMO may have implications in OBs fate and breast cancer progression. The five highly downregulated genes were PCSK5, PTGDS, CXCL14, ADGRD1, and SMOC2 **(Table 5.4)**. SMOC2, a calcium-binding protein is known to inhibit osteogenesis and prevent mineralization in OBs.[255] ADGRD1 also known as GPR133 could also have implications in bone diseases.[256] CXCL14 has shown to be expressed in the stromal cells in malignant breast cancer[257] and has been shown to induce lung cancer metastasis to bone.[258]

Next, the top functional enrichment pathways of the upregulated genes were determined namely blood vessel development, epithelial cell differentiation, regulation of cell adhesion, chemotaxis, regulation of GTPase activity, leukocyte migration, positive regulation of cell migration and pathways in cancer **(Figure 5.9b)**.

The downregulated pathways were cell surface receptor signaling pathway, reproductive structure development, regulation of ossification, heart field specification and response to BMP **(Figure 5.9c)**. Four hub genes from the upregulated PPI network were identified namely KDR, ITGAM, CXCR4, and PECAM1. Since the upregulated hub genes were mostly associated with endothelial cells, we speculated that the downregulated hub genes would provide more information about the influence of vessels in the VBCTs. The four downregulated hub genes were determined namely BMP4, C3 protein, CXCL13, and DKK1. BMP4 and C3 were significantly expressed in normal tissue as compared to cancerous breast cancer tissues **(Figure 5.9d, e)** whereas CXCL13 and DKK1 is observed to be expressed in breast cancer tissue as compared to normal breast tissue **(Figure 5.9f, g).**

Table 5.4 Top five upregulated and downregulated genes due to the presence of BVs (NHMO vs. NMO)

Gene symbol	Gene name	Expression	FC	P-value
ANGPT2	angiopoietin 2	up	416.87	4.25E-12
CD34	CD34 molecule	up	220.18	1.02E-09
LYVE1	lymphatic vessel endothelial hyaluronan receptor 1	up	205.97	5.98E-11
VWF	von Willebrand factor	up	180.5	9.97E-12
PECAM1	platelet/endothelial cell adhesion molecule 1	up	142.58	4.75E-09

SMOC2	SPARC related modular calcium binding 2	down	-5.83	9.98E-05
ADGRD1	adhesion G protein-coupled receptor D1	down	-6.1	6.57E-06
CXCL14	chemokine (C-X-C motif) ligand 14	down	-8.35	6.24E-07
PTGDS	prostaglandin D2 synthase 21kDa (brain)	down	-8.95	3.58E-10
PCSK5	proprotein convertase subtilisin/kexin type 5	down	-9.67	3.55E-07

5.4. Discussion

The theory that there is already a prior interaction between primary tumor and secondary site before metastasis is not new.[259] For instance, previous reports have shown that lung tumors can remotely activate the OBs, and the OBs, in turn, supply the lung tumors with tumor-promoting neutrophils even before the inception of metastasis.[260] Another *in-vivo* study showed that OBs-derived hypoxia-inducible factor led to distant breast cancer growth and dissemination, partly due to the enhanced production of CXCL12.[227] The study also showed that osteoclasts did not possess a similar ability to regulate distant BCCs, which highlights the importance of OBs in influencing primary tumor site.[227] A recent article showed that colorectal cancers release extracellular vesicles that activate fibroblasts in distant organs.[261] The fibroblasts then produces inflammatory cytokines that promote primary tumor growth.[261] Therefore, it is evident that the pre-metastatic indirect interaction between secondary and primary sites could illuminate several hidden yet important pathways that initiate the metastasis process.

In human bone, OBs account for 4-6% of the total bone cells and deposit bone matrix.[262] OBs maintain a homeostatic bone environment together with osteoclasts, the bone-degrading cells and resident osteocytes.[262] Breast cancer metastasis to the bone disrupts this homeostasis and leads either to enhanced bone deposition (osteoblastic) or enhanced bone resorption (osteolytic). Several studies in the past have already elucidated the role of BCCs in the fate of OBs.[263, 264] These studies illuminate how the BCCs remotely prime the secondary bone sites before or after homing. However, the role of the secondary bone site on the primary tumor prior to metastasis hasn´t been studied in its entirety.

Cancer cells not only possess the intrinsic ability to proliferate and metastasize but also rely on their surrounding tumor-microenvironment for their progression. The TME is a crowded milieu comprising of multiple cell types such as fibroblasts, endothelial cells, and ECM moieties that constantly interact with one another to modulate tumor fate. The scaffold-free VBCTs that we fabricated are composed of

the cancer cells at an interface of vasculature and connective tissue and provide a realistic alternative to conventional 3D models. Our results indicate that the presence of MDA-MB231 in VBCT resulted in sectioned and abnormal vessels and this abnormality was accentuated in the presence of OBs.

Solid tumors require vessels for growth and metastasis and therefore enforce the production of more BVs. However, cancer cells not only rely on angiogenesis to initiate the metastatic process but can also hijack pre-existing vessels in the tumor microenvironment in a non-angiogenic process called vessel co-option.[265, 266] Cancer cells, during rapid proliferation in the tissue, also compress the surrounding vasculature in the microenvironment thereby leading to vessel collapse.[267] Recently, it was shown in an *in-vitro* 3D model that cancer cells' interaction with the vasculature led to compression and destruction of the vessel.[268] In another study, it was shown that pancreatic ductal carcinoma cell (PDAC) ablates endothelial cells both in *in-vitro* and *in-vivo* settings that lead to hypo-vascularization in the PDAC tumor tissue.[269]

In a confined tumor-microenvironment, cells compete for space and nutrients. Cancer cells are highly proliferative in comparison to endothelial cells, which could lead to the elimination of the 'weaker' cell population (endothelial cells) by the 'fitter' cell population (MDA-MB231).[269] The scaffold-free model fabricated in a confined cell-culture insert area includes three different cell types in large numbers, each competing for the available nutrients and space, which could explain the elimination of endothelial cells. Furthermore, it could be hypothesized that the presence of OBs and their secreted factors such as CXCL12 could lead to enhanced cellular proliferation and therefore further lead to reduced availability of the limited nutrient to individual cells. We observed via cell proliferation XTT assay that CXCL12 leads to a slight increase in MDA-MB231 and HUVECs proliferation, and a significant increase in proliferation of fibroblasts **(Figure 5.3h).**

Several other factors could affect angiogenesis and vascular fate. One such factor is the progression stage of the tumor. For instance, it has been shown previously in gliomas that the vessels undergo three stages of development: a) tumor-vessel interaction phase b) transition phase where vessel apoptosis takes place followed by c) angiogenic phase.[270] The increase in VEGF and the presence of thin vascular sprouts in VBCT suggest a transition phase preceding angiogenesis. For these phases to occur, tumor cells have to be in close proximity to the vessels since these phases require direct cell-cell interactions. The advantage of our model is the ability of cancer cells to directly interact with BVs **(Figure 5.10a, b)**.

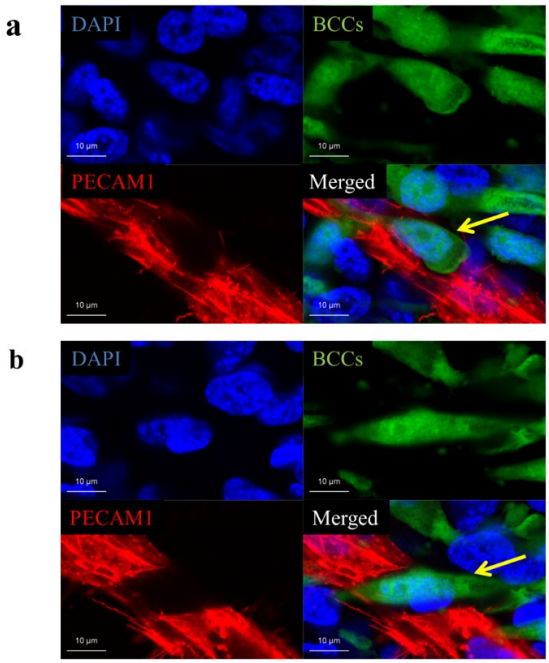

Figure 5.10 *a) Direct cell-cell contact between BCCs and vessels (DAPI=blue, BCCs=green, PECAM-1=red), scale bar=10µm b) BCCs penetrates and sections the vessels during direct contact, scale bar=10 µm*

Lastly, the influence of the highly proliferating TNBC on vasculogenesis (apart from angiogenesis) should also be taken into consideration since MDA-MB231 cells are mixed together with endothelial cells and not introduced to fully-formed vessels. Future experiments where MDA-MB231 cells are introduced after the formation of BVs in the model could elucidate different angiogenic mechanisms.

We show a number of interesting upregulated hub genes from the gene array data between NHMO and NHM samples where we studied the effect of OBs on VBCTs. We observed HSP90N as an upregulated hub gene that has been previously linked to aggressiveness in breast tumors.[271, 272] HSP90N inhibitors have been used in the past for cancer therapy and could also have an implication in bone metabolism.[273] Interestingly, HSP90N expression is also associated with enhanced bone metastasis from prostate and breast tumors.[274, 275] The other hub genes EGFR, RPS27A and CYCS have also been previously identified as hub genes in TNBC extracted from several gene expression datasets.[276] The overexpression of EGFR, another upregulated hub gene, leads to poor prognosis in breast cancer patients.[277, 278] EGFR results in cancer cell proliferation, aggressiveness and metastasis.[279] Interestingly, expression of EGFR has also be linked to increased metastasis of cancer cells to bone.[279] For instance, previous results have shown that EGFR signaling can lead to osteoclastogenesis by influencing Osteoprotegerin (OPG) and MCP1 signals in osteoblasts.[280]

The changes in gene expression between NHMO and NMO were studied to deliberate the impact of BVs. We hypothesized the presence or absence of BVs would lead to modified gene expression. DKK1,

an antagonist of the Wnt/β-catenin signaling pathway was detected as a downregulated hub gene. Previously, it has been shown that DKK1 functions as a tumor suppressor.[281] Interestingly, upregulation of DKK1 has shown to be involved in specific breast cancer metastasis to bone.[282, 283] Furthermore, tumor-derived DKK1 also dictates the OBs fate by inhibiting OBs differentiation and facilitates osteolysis.[284] It is intriguing that in the presence of BVs in the cancerous tissue, DKK1 was observed as a downregulated hub gene. In malignant gliomas, it was previously reported that hypoxia led to an upregulation of DKK1 as compared to normoxia.[285] It could be theorized that in the absence of BVs and their secreted growth factors in the non-vascularized tissue, DKK1 was upregulated which in turn could result in the enhanced preference of breast cancer metastasis to bone. A more thorough future investigation into the role of BVs in DKK1 expression could highlight many possible mechanisms in bone metastasis. Another downregulated hub gene BMP4 has previously shown to inhibit proliferation but accentuate cell migration in breast cancer.[286] BMP4 can act as both tumor suppressor and promoter.[287] One study showed that BMP4 upregulation is associated with reduced metastasis and the downregulation of BMP4 has been associated with more aggressive breast cancer.[288] Another study showed that mice treated with BMP4 showed a positive correlation with bone metastasis.[289] Finally, downregulated hub genes complement protein C3 and CXCL13 both could have implications in breast cancer progression and modulation in bone microenvironment.[290, 291]

Together, the developed *in-vitro* model could is suitable to study several pathways involved in the progression of metastasis and organotropism. In this study, we show that indirect culture with OBs leads to a change in the gene expression profile of VBCTs. This emphasizes the point that reciprocal OBs secreted factors could be an important parameter in early metastasis events in breast cancer. Future work would include a) validation of the protein expression b) screening of more soluble paracrine factors c) influence of breast cancer tissue on OBs d) addition of other main cellular players such as osteoclasts and functional immune cells to elucidate the role of different cell types in cancer progression or dormancy.

5.5. Conclusion

In summary, we present a 3D co-culture system utilized to understand the interaction between several cell types involved in breast cancer metastasis to the bone. The fabricated VBCTs provide a realistic microenvironment to the TNBC cells with the presence of fully formed vasculature, surrounding fibroblasts and cell-secreted ECM. The simplicity of the culturing and harvesting of the 3D model allowed a gene-level study of the influence of OBs and BVs on the engineered cancer tissue. These results provide a proof-of-concept for the utilization of such models for the understanding of time-dependent metastatic progression. Such models in the future can be used in predicting essential biomarkers for diagnosis and for pre-clinical testing of novel therapeutic agents.

Appendix

Development of vascularized scaffold-free Atopic dermatitis models

A.1. Introduction

The skin suffers from a wide range of pathologies, many of which are often not completely understood. Atopic dermatitis (AD) or Eczema, is one of the most commonly occurring skin inflammatory disease.[292] It was accepted that a hereditary genetic component was often responsible for AD but the increase in incidences revealed a more complex reality. Factors often include mutations affecting FLG (FLG) expression and the exacerbation of the disease by inflammation and scratching. However, not all defects in FLG expression result in AD. Therefore there are other factors that are at play, these may include other genetic factors or gene-gene interactions.[293] Recent findings about the different mechanisms and causative factors or etiology allows for more therapies to be developed and considered when dealing with AD.[294] Skin models present an excellent option in order to test the efficacy and toxicity of the different therapeutic alternatives. They provide an *in vitro* model that avoids the use of animal testing for preliminary results.[166] This chapter investigates the effect of corticosteroids in this full thickness vascularized three-dimensional (3D) skin model with the induced characteristics and environment of AD. The project involves the fabrication and optimization of scaffold-free vascularized healthy and diseased skin models using cell coating and accumulation technique. The vascularized AD skin model, in the near future, could aid in the screening of important drugs and cosmetics that could eventually be used for personalized therapy of patients suffering from skin ailments.

Corticosteroids

Corticosteroids are drugs which are often prescribed to treat significant inflammation or allergic reactions; they are one of the most commonly used drugs prescribed as a treatment to inflammatory and immune diseases.[295] Delivery methods include oral, topical application, and *via* injection. Corticosteroids are chemicals that can be either naturally occurring hormones or synthetic. There are two main classes: glucocorticoids and mineralocorticoids. Glucocorticoids are mostly used for the regulation of inflammation while mineralocorticoids play a role with the balance of salt and water. Different corticosteroid drugs can possess a combination of these two classes, or be solely anti-inflammatory or only affecting the electrolyte and fluid levels and thus blood pressure with its mineralocorticoid properties.[296] There are many anti-inflammatory drugs, but corticosteroids are capable of “inhibiting virtually all the components of inflammation”.[297] Corticosteroids can turn off some inflammatory pathways, its main target are different inflammatory genes that encodes for common inflammatory molecules such as cytokines, certain receptors, chemokines and other molecules. It is, however, important to note that despite being such an effective tool against inflammation they have a

complex systemic response that affects more than just the target.[295] Additionally, glucocorticoids also affect vasculature by affecting endothelial and vascular smooth muscle cells directly contributing to vasoconstriction by inhibiting the production of vasodilators like prostacyclin and nitric oxide.[298]

As some of the characteristic occurrences of AD are the activation of inflammatory pathways and changes to the vasculature which result in vasodilated and leaky and more permeable vessels, a corticosteroid is an appropriate choice of treatment as it is able to counteract several of the causes and effects of AD. Corticosteroids offer a promising therapy to wide range of ailments and their effects are well investigated. However, due to the prevalence of these drugs for a multitude of treatments their resulting side effects have also garnered attention.[299] There are a wide range of side effects that stem from the use of corticosteroids. Side effects vary depending on dosage of the drug, duration of use, location of use and its delivery method.[300, 301] In skin the most common side effect is atrophy to the skin which can occur in both the dermis and the epidermis. The earlier effect is a thinning of the epidermis due to a decrease of the size of epidermal cells.[301] An overview of other side effects that can occur is provided in **Table A.1.**

Table A.1 Overview of most common corticosteroid side-effects, table reproduced with permission from [299]

Complications	**Signs/Symptoms**
Morphologic changes	Cushingoid changes Truncal obesity Facial adipose tissue (moon facies) Dorsocervical adipose tissue (buffalo hump)
Hyperglycemia	Increased blood sugar levels
Infection	Bacterial, fungal, and viral infections
Wound healing	Decrease monocytes/macrophages Delayed wound healing
Bone metabolism	Decrease bone density Avascular necrosis
Ophthalmic	Cataracts Glaucoma
Skin changes	Dermal Thinning, skin fragility, end ecchymosis Striae
Gastrointestinal	Peptic ulceration
Adrenal suppression	

	Multiple systemic effects, blood pressure changes, water retention, lack of stress response
Myopathy	Type IIb muscle fiber atrophy
Cardiovascular	Increase blood pressure Myocardial infarction and cerebrovascular disease
Psychiatric	Mild effects: agitation, anxiety, distractibility, fear, hypomania, indifference, insomnia, irritability, lethargy, pressured speech, restlessness, and tearfulness Severe reactions: mania, depression (suicidal ideations), aggressiveness

A.2. Materials and Methods

Materials

Cells

Normal human dermal fibroblasts (NHDFs) – provided by the Department of Dermatology and Allergology, RWTH Aachen University Hospital isolated from obtained biopsies via the protocol detailed in [111]. Human umbilical vein endothelial cells (HUVECs) were purchased from Sigma Aldrich.

Methods

Cell culture

All cells were cultured with standard cell culture techniques. NHDFs were cultured in high glucose DMEM with 10% FBS and 1% P/S in T175 flasks and used only up to passage 9. To collect the cells media was aspirated and then washed with PBS; 3 ml of TrypLE™ Express was added for 5 minutes and cells were checked to be detached before adding media to neutralize the trypsin. HUVECs were cultured in EGM-2 and used up to passage 5, trypsinization was only done for 3 minutes and the prepared DMEM was used to neutralize the trypsin. KCs were cultured in keratinocyte growth medium (KGM) and used for experiments only up to passage 4. KCs were provided in petri dishes directly the day before the experiment by the Department of Dermatology and Allergology in the RWTH University Hospital in Aachen. For the collection of the KCs 0.05% Trypsin/0.02% EDTA was used for trypsinization for 10-15 minutes or until cells were detached (checking every 5 minutes) and high glucose DMEM with 10% FBS and 1%P/S used to stop reaction and collect cells in a falcon tube.

Construction of vascularized skin model

NHDFs were collected in a 50 ml falcon tube and centrifuged at 1200 rpm for 5 min. The supernatant was discarded, and cells were washed in PBS. After suspension in PBS the cells were then incubated and mixed for one minute in 0.04 mg/mL of FN and then in 0.04 mg/mL of G, with PBS washes in

between to create a layer-by-layer coating of the fibroblasts. In between each step the suspension was centrifuged for one minute at 2000 RPM and the supernatant was subsequently discarded, and the pellet was re-suspended in appropriate solution. Meanwhile the inserts were washed with PBS and coated with FN and left to incubate for the duration of the coating procedure. After coating, the cells are then collected in DMEM and counted and incubated, while the HUVECs are also harvested and counted. FN was aspirated from the inserts prior to adding cells. The tissue is composed of 15 layers of NHDFs and 3 layers of HUVECs per insert, each layer contains $1x10^5$ cells. Required amount of both cells is collected together and seeded on the membrane of each insert in 300 µL of DMEM. 1 mL of DMEM containing 10% FBS and 1% P/S was added to the plate and put into the incubator with 37 °C and 5% CO_2 for 2 hours. Media was then aspirated and then replaced with 2 mL of media which is half EGM-2 and half DMEM and left in incubator overnight. This creates a vascularized dermis. In order to create the epidermal layer KCs are added on top the following day. Media is partly aspirated and 90 µL of Col IV is added on top of the dermal tissue and incubated during the collection of the KCs, which are then added in 300µL of Derma-Life media after aspiration of the Col IV. Additional media is then added (media consists of a mixture of DMEM, EGM-2, Derma-Life and a supplement of 50 µg/mL of ascorbic acid). Epidermal layer was exposed to air on the following day to provide and air-liquid interface of the skin tissue.

Immunohistochemistry

Samples were embedded in Tissue-Tek OCT compound and frozen. Sections were then cut using a cryostat and stained using H&E for evaluation.

Induction of AD and treatment (Experimental overview)

The disease model was created by the addition of IL-4 and IL-13 at a concentration of 50 ng/mL (different conditions described in Error! Reference source not found.). In addition, the samples were a lso treated with the corticosteroid Solu-Decortin H at two different concentrations of 0.7 µM and 7.0 µM.

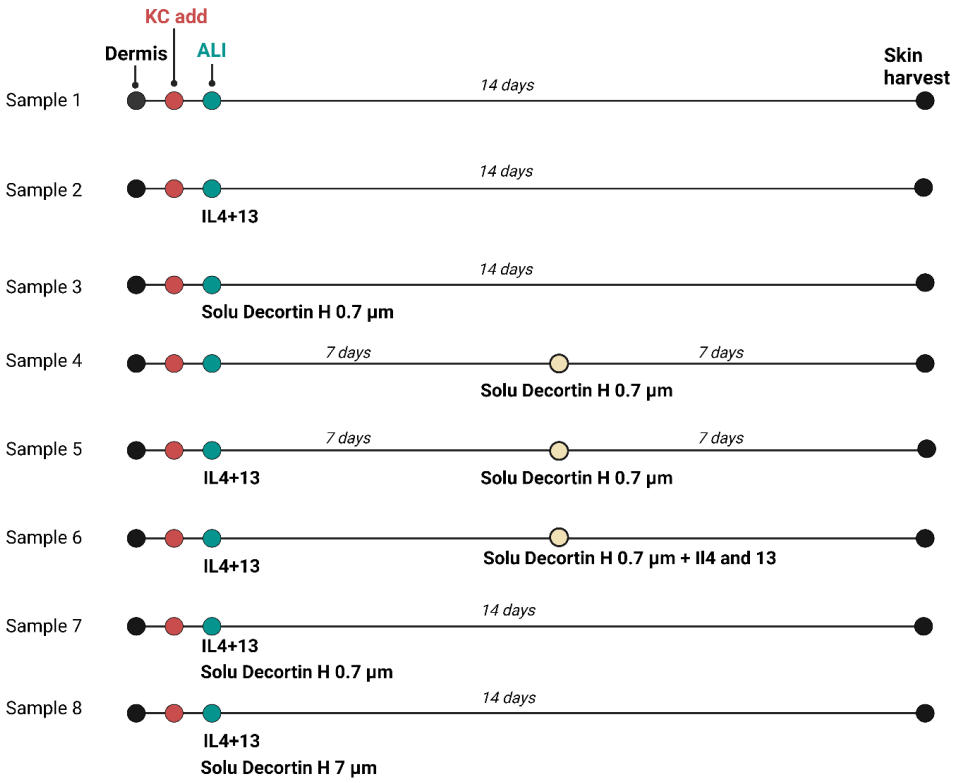

Schematic A.1: *Overview of the different testing conditions for steroids on an AD model*

A.3. Results

Immuno-histochemical evaluation of model, induction of disease and steroidal treatment

Different conditions were made to test the efficacy of the treatment with Solu-Decortin H, including when the steroid was applied and its concentration as was previously demonstrated. **Figure A.1** to **Figure A.4** show the observations for the various treated samples.

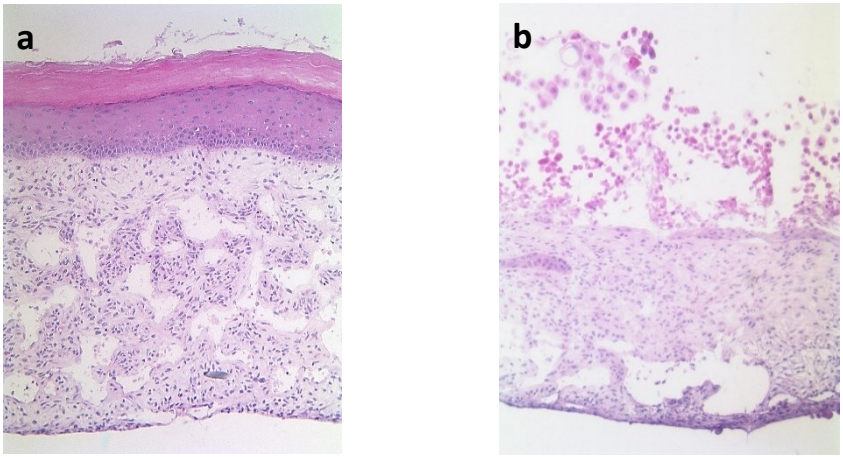

Figure A.1*: a) healthy Control: medium 14 days. b) Atopic dermatitis phenotype induced by IL4+IL13 (50ng/ml) treatment for 14 days. Images taken at 10X magnification.*

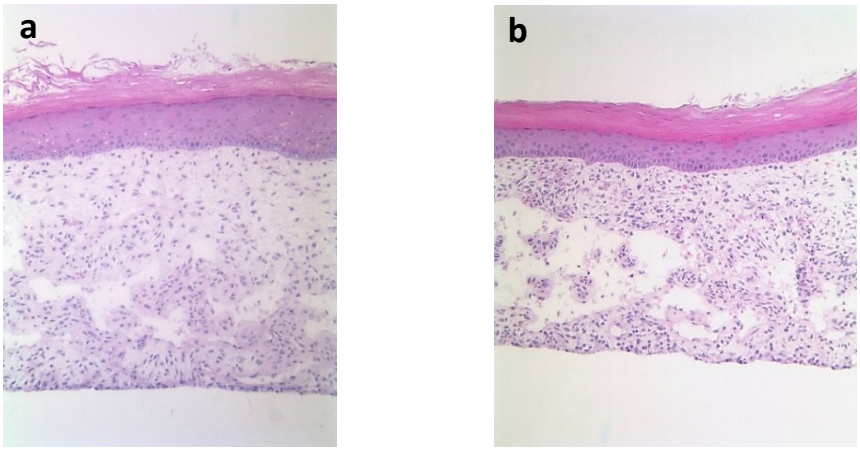

Figure A.2. *a) Solu-Decortin H 0.7 µM for 14 days b)– normal media for 7 days, followed by Solu-Decortin H0.7 µM for 7 days, 10X magnification*

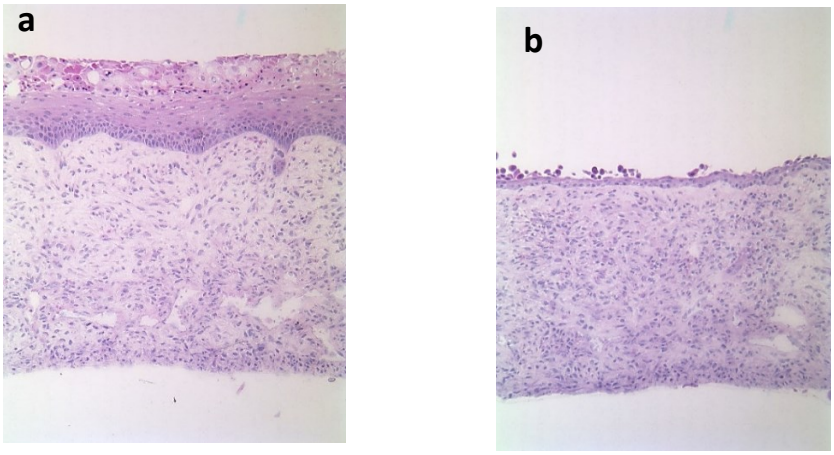

Figure A.3. *a) Sample 5– IL4+IL13 (50 ng/ml) for 7 days followed by Solu-Decortin H 0.7 µM for 7 days b) IL4+IL13 (50 ng/ml) for 7 days followed by Solu-Decortin H 0.7 µM for 7 days and continued IL4+ IL13 (50 ng/ml), 10X magnification*

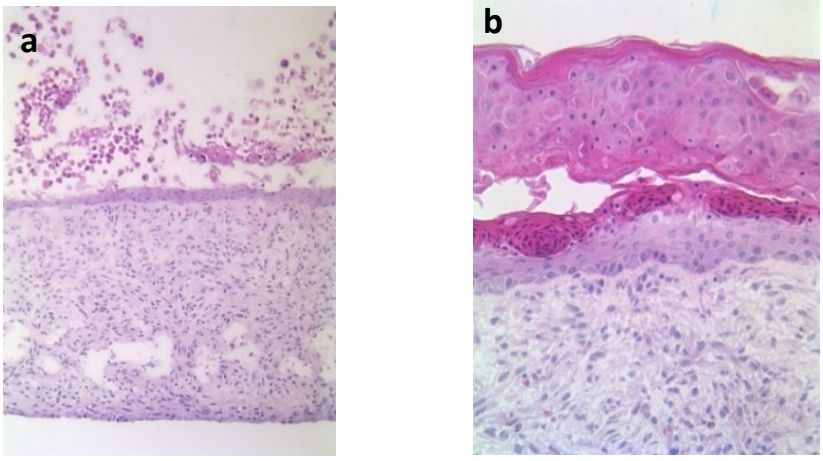

Figure A.4. *a) Sample 7– IL4+IL13 (50ng/ml) + Solu-Decortin H 0.7 µM for 14 days b) IL4+IL13 (50ng/ml) +Solu-Decortin H 7.0 µM for 14 days,10X Magnification*

Figure A.1a represents the healthy skin tissue. A well demarcated epidermal and dermal layers are visible. The epidermis is observed to be composed of several layers, with the top layer comprising cornified Keratinocytes. The effect of a combinatory treatment of IL-4 and IL-13 (50 ng/ml respectively) cytokines is clearly shown in Error! Reference source not found.**1b**, where the epidermal l ayer shows abnormality similar to the condition in AD. **Figure A.2a** shows the H&E staining of healthy skin tissue treated with 0.7 µM Solu-Decortin for 14 days and **Figure A.2b** shows the skin models treated with the steroid for 7 days. These samples were used as controls for the therapy. **Figure A.3a** is the sample which is treated with the steroids on the diseased tissue. A low Solu-Decortin H concentration (0.7µM) was applied after induction of diseased state in the tissue with IL-4/IL-13 combination. Complete preservation of epidermal erosion due to the addition of Solu-Decortin H can be observed. The epidermal thickness, however, appears to be thinner in comparison to the healthy skin models which is a well-known side effect of steroid application.[301]

Next, models were treated with both a low Solu-Decortin H concentration (0.7µM) and the two cytokines (IL-4 and IL-13) after the 7 days of treatment with only cytokines to simulate AD **(Figure A.3b)**. This model represents the ``rescue´´ condition and more accurately mimics the diseased state where immune cells continually produce cytokines despite the steroid application. Erosion of the epidermal layer as a result of cytokine treatment can still be observed in **Figure A.3b** even with treatment of Solu-Decortin H. The low concentration of the steroidal dug is not sufficient to prevent epidermal erosion and preserve healthy epidermal morphology when the model is treated with the cytokines for the 14 days. Similar results were observed when both Solu-Decortin H was added along with the IL-4/IL-13 combination from the initial time point for a total time duration of 14 days **(Figure A.4a)**.

Finally, Solu-Decortin H concentration was increased to 7 µM and applied with the cytokine combination from Day 0 until Day 14, as done in sample 7. **Figure A.4b** shows a repaired epidermal layer and thus preservation of epidermal integrity can be observed.

In this study, it was shown that the characteristic barrier dysfunction which is found in AD can be replicated in this skin model by the addition of IL-4 and IL-13. This was observed with the loss of epidermal integrity in the model treated with these cytokines. Additionally, as was expected treatment with steroid had some underlying effects on the models as it would when applied to the body and it showed it is capable of reversing the effects of AD by restoring epidermal integrity to the skin equivalents. It is important to note that Solu-Decortin H must be applied in the high concentrations to yield the desired restorative and protective effect. Treatment with the corticosteroid, Solu-Decortin H, is shown to have the ability to repair the barrier or to help preserve the integrity of the epidermal layer. This is however only true when sufficient amounts of the steroidal drug are applied to the tissue. Due

to side effects that can stem from increased and repeated steroid usage an optimal amount for treatment should be discerned.

Further understanding of the effect of steroids on vasculature and the impact of steroids on AD treatment will be clarified in future experiments. Future experiments will determine the optimal concentration of Solu-Decortin H required to halt disease progression in these scaffold-free *in-vitro* models.

6. References

[1] R. Rimal, Y. Marquardt, T. Nevolianis, S. Djeljadini, A. B. Marquez, S. Huth, D. N. Chigrin, M. Wessling, J. M. Baron, M. Möller, *Applied Materials Today* **2021**, 25, 101213.

[2] R. L. Giesey, S. Mehrmal, P. Uppal, G. Delost, *SKIN The Journal of Cutaneous Medicine* **2021**, 5, 125.

[3] L. M. Hollestein, T. Nijsten, *Journal of Investigative Dermatology* **2014**, 134, 1499.

[4] H. W. Lim, S. A. Collins, J. S. Resneck Jr, J. L. Bolognia, J. A. Hodge, T. A. Rohrer, M. J. Van Beek, D. J. Margolis, A. J. Sober, M. A. Weinstock, *Journal of the American Academy of Dermatology* **2017**, 76, 958.

[5] A. M. Wojtowicz, S. Oliveira, M. W. Carlson, A. Zawadzka, C. F. Rousseau, D. Baksh, *Wound repair and regeneration* **2014**, 22, 246.

[6] M. Jevtić, A. Loewa, A. Nováčková, A. Kováčik, S. Kaessmeyer, G. Erdmann, K. Vávrová, S. Hedtrich, *Biochimica et Biophysica Acta (BBA)-Molecular Cell Research* **2020**, 1867, 118722.

[7] R. K. Jain, P. Au, J. Tam, D. G. Duda, D. Fukumura, *Nature biotechnology* **2005**, 23, 821.

[8] T. Gura, *Science* **1997**, 278, 1041.

[9] S. Gallagher, U. Kruger, K. Josyula, A. Gong, A. Song, R. Sweet, B. Makled, C. Parsey, J. Norfleet, S. De, *Scientific Reports* **2022**, 12, 4565.

[10] C. Choe, J. Schleusener, J. Lademann, M. E. Darvin, *Journal of biophotonics* **2018**, 11, e201700355.

[11] P. A. Gerber, B. A. Buhren, H. Schrumpf, B. Homey, A. Zlotnik, P. Hevezi, *Biological chemistry* **2014**, 395, 577.

[12] H. D. Zomer, A. G. Trentin, *Journal of dermatological science* **2018**, 90, 3.

[13] D. A. Ewald, S. Noda, M. Oliva, T. Litman, S. Nakajima, X. Li, H. Xu, C. T. Workman, P. Scheipers, N. Svitacheva, *Journal of Allergy and Clinical Immunology* **2017**, 139, 562.

[14] W. R. Swindell, A. Johnston, S. Carbajal, G. Han, C. Wohn, J. Lu, X. Xing, R. P. Nair, J. J. Voorhees, J. T. Elder, *PloS one* **2011**, 6, e18266.

[15] J. R. Yu, J. Navarro, J. C. Coburn, B. Mahadik, J. Molnar, J. H. Holmes IV, A. J. Nam, J. P. Fisher, *Advanced healthcare materials* **2019**, 8, 1801471.

[16] E. Fuchs, S. Raghavan, *Nature Reviews Genetics* **2002**, 3, 199.

[17] E. Proksch, J. M. Brandner, J. M. Jensen, *Experimental dermatology* **2008**, 17, 1063.

[18] V. T. Natarajan, P. Ganju, A. Ramkumar, R. Grover, R. S. Gokhale, *Nature chemical biology* **2014**, 10, 542.

[19] C. L. Simpson, D. M. Patel, K. J. Green, *Nature reviews Molecular cell biology* **2011**, 12, 565.

[20] R. Wong, S. Geyer, W. Weninger, J. C. Guimberteau, J. K. Wong, *Experimental dermatology* **2016**, 25, 92.

[21] K. Vig, A. Chaudhari, S. Tripathi, S. Dixit, R. Sahu, S. Pillai, V. A. Dennis, S. R. Singh, *International journal of molecular sciences* **2017**, 18, 789.

[22] Y. E. Yun, Y. J. Jung, Y. J. Choi, J. S. Choi, Y. W. Cho, *Journal of Pharmaceutical Investigation* **2018**, 48, 215.

[23] A. N. Dehkordi, F. M. Babaheydari, M. Chehelgerdi, S. R. Dehkordi, *Stem cell research & therapy* **2019**, 10, 111.

[24] M. J. Randall, A. Jüngel, M. Rimann, K. Wuertz-Kozak, *Frontiers in bioengineering and biotechnology* **2018**, 6, 154.

[25] E. Berardesca, P. Elsner, H. I. Maibach, *Bioengineering of the skin: cutaneous blood flow and erythema*, Vol. 2, CRC Press, **1994**.

[26] I. M. Braverman, presented at *Journal of Investigative Dermatology Symposium Proceedings*, **2000**.

[27] I. M. Braverman, A. Yen, *Journal of investigative Dermatology* **1977**, 68, 44.

[28] E. M. Landis, *Journal of Investigative Dermatology* **1938**, 1, 295.

[29] R. A. Swerlick, *The Journal of dermatology* **1997**, 24, 734.

[30] J. G. Rheinwald, in *International Review of Cytology*, Vol. 10, Elsevier, 1979.

[31] J. G. Rheinwald, H. Green, *Cell* **1975**, 6, 317.

[32] G. J. Todaro, H. Green, *The Journal of cell biology* **1963**, 17, 299.
[33] J. G. Rheinwatd, H. Green, *Cell* **1975**, 6, 331.
[34] H. Green, *Cell* **1977**, 11, 405.
[35] H. Green, O. Kehinde, J. Thomas, *Proceedings of the National Academy of Sciences* **1979**, 76, 5665.
[36] T. J. Phillips, O. Kehinde, H. Green, B. A. Gilchrest, *Journal of the American Academy of Dermatology* **1989**, 21, 191.
[37] M. Koga, *Archives of dermatology* **1988**, 124, 1656.
[38] H. Mizutani, Y. Shirakata, A. Adachi, K. Hashimoto, M. Shimizu, *The Lancet* **1998**, 352, 709.
[39] C. Cuono, R. Langdon, J. McGuire, *The Lancet* **1986**, 327, 1123.
[40] E. Bell, H. P. Ehrlich, D. J. Buttle, T. Nakatsuji, *Science* **1981**, 211, 1052.
[41] E. Bell, N. Parenteau, R. Gay, C. Nolte, P. Kemp, P. Bilbo, B. Ekstein, E. Johnson, *Toxicology in vitro* **1991**, 5, 591.
[42] C. K. Griffith, C. Miller, R. C. Sainson, J. W. Calvert, N. L. Jeon, C. C. Hughes, S. C. George, *Tissue engineering* **2005**, 11, 257.
[43] D. M. Young, K. M. Greulich, H. G. Weier, *J Burn Care Rehabil* **1996**, 17, 305.
[44] L. Chen, H. Deng, H. Cui, J. Fang, Z. Zuo, J. Deng, Y. Li, X. Wang, L. Zhao, *Oncotarget* **2018**, 9, 7204.
[45] P. Libby, *Nutrition reviews* **2007**, 65, S140.
[46] W.-H. Boehncke, M. P. Schön, *The Lancet* **2015**, 386, 983.
[47] R. Heidenreich, M. Röcken, K. Ghoreschi, *International journal of experimental pathology* **2009**, 90, 232.
[48] P. Telner, Z. Fekete, *Journal of Investigative Dermatology* **1961**, 36, 225.
[49] R. Huggenberger, M. Detmar, presented at *Journal of Investigative Dermatology Symposium Proceedings*, **2011**.
[50] B. J. Nickoloff, R. S. Mitra, J. Varani, V. M. Dixit, P. J. Polverini, *The American journal of pathology* **1994**, 144, 820.
[51] M. Bhushan, B. McLaughlin, J. Weiss, C. Griffiths, *British Journal of Dermatology* **1999**, 141, 1054.
[52] J. Creamer, J. Barker, *Clinical and experimental dermatology* **1995**, 20, 6.
[53] T. Markham, R. Mullan, L. Golden-Mason, S. Rogers, B. Bresnihan, O. FitzGerald, U. Fearon, D. J. Veale, *Journal of the American Academy of Dermatology* **2006**, 54, 1003.
[54] D. N. Sauder, J. DeKoven, P. Champagne, D. Croteau, É. Dupontb, *Journal of the American Academy of Dermatology* **2002**, 47, 535.
[55] P. H. Prose, E. Sedlis, *Journal of Investigative Dermatology* **1960**, 34, 149.
[56] Y. Zhang, H. Matsuo, E. Morita, *Arch Dermatol Res* **2006**, 297, 425.
[57] L. Sankar, D. Arumugam, S. Boj, P. Pradeep, *J Clin Diagn Res* **2017**, 11, EC23.
[58] A. L. Bressan, B. L. Picciani, L. Azulay-Abulafia, A. K. Fausto-Silva, P. N. Almeida, K. S. Cunha, E. P. Dias, S. Carneiro, *International journal of dermatology* **2018**, 57, 209.
[59] S.-C. Liew, E. Das-Gupta, S. Chakravarthi, S.-F. Wong, N. Lee, N. Safdar, A. Jamil, *BMC research notes* **2012**, 5, 1.
[60] S. Hanssen, C. van der Vleuten, P. van Erp, M. Seyger, P. van de Kerkhof, *Journal of Dermatological Treatment* **2019**, 30, 221.
[61] H. J. Lee, Y. J. Hong, M. Kim, *Int J Mol Sci* **2021**, 22.
[62] A. Genovese, A. Detoraki, F. Granata, M. Galdiero, G. Spadaro, G. Marone, in *New Trends in Allergy and Atopic Eczema*, Vol. 96, Karger Publishers, 2012.
[63] R. Agha-Majzoub, R. P. Becker, D. E. Schraufnagel, L. S. Chan, *Microcirculation* **2005**, 12, 455.
[64] Q. Peng, K. Sha, Y. Liu, M. Chen, S. Xu, H. Xie, Z. Deng, J. Li, *Frontiers in cell and developmental biology* **2021**, 9.
[65] K. Yamasaki, R. L. Gallo, *Journal of dermatological science* **2009**, 55, 77.
[66] A. H. Gomaa, M. Yaar, M. M. Eyada, J. Bhawan, *Journal of cutaneous pathology* **2007**, 34, 748.
[67] K. Aroni, E. Tsagroni, N. Kavantzas, E. Patsouris, E. Ioannidis, *Archives of dermatological research* **2008**, 300, 125.

[68] L. F. Brown, T. J. Harrist, K.-T. Yeo, M. Ståhle-Bäckdahl, R. W. Jackman, B. Berse, K. Tognazzi, H. F. Dvorak, M. Detmar, *Journal of Investigative Dermatology* **1995**, 104, 744.
[69] V. Martins, M. Caley, K. Moore, Z. Szentpetery, S. Marsh, D. Murrell, M. Kim, M. Avari, J. McGrath, R. Cerio, *JNCI: Journal of the National Cancer Institute* **2016**, 108.
[70] P. Mabeta, *Biomedicine & Pharmacotherapy* **2020**, 127, 110135.
[71] M. Carleton, M. Zhou, O. De Henau, P. Phillips, T. Chen, Y. Feng, S.-P. Huang, A. Walsh, T. P. Reilly, I. Melero Bermejo, American Society of Clinical Oncology, 2018.
[72] M. Kashani-Sabet, R. W. Sagebiel, C. M. Ferreira, M. Nosrati, J. R. Miller III, *Archives of dermatology* **2001**, 137, 1169.
[73] R. H. Farnsworth, M. Lackmann, M. G. Achen, S. A. Stacker, *Oncogene* **2014**, 33, 3496.
[74] I. Helfrich, D. Schadendorf, *Molecular oncology* **2011**, 5, 137.
[75] H. Erhard, F. Rietveld, E. Bröcker, D. Ruiter, *Melanoma research* **1997**, 7, S19.
[76] T. Kaully, K. Kaufman-Francis, A. Lesman, S. Levenberg, *Tissue Eng Part B Rev* **2009**, 15, 159.
[77] A. F. Black, F. Berthod, N. L'Heureux, L. Germain, F. A. Auger, *Faseb j* **1998**, 12, 1331.
[78] V. Hudon, F. Berthod, A. F. Black, O. Damour, L. Germain, F. A. Auger, *Br J Dermatol* **2003**, 148, 1094.
[79] D. M. Supp, A. P. Supp, S. T. Boyce, S. M. Bell, *Journal of investigative dermatology* **2000**, 114, 5.
[80] D. M. Supp, K. Wilson-Landy, S. T. Boyce, *The FASEB Journal* **2002**, 16, 797.
[81] P. L. Tremblay, V. Hudon, F. Berthod, L. Germain, F. A. Auger, *Am J Transplant* **2005**, 5, 1002.
[82] C. Auxenfans, C. Lequeux, E. Perrusel, A. Mojallal, B. Kinikoglu, O. Damour, *J Tissue Eng Regen Med* **2012**, 6, 512.
[83] J. F. Hansbrough, S. T. Boyce, M. L. Cooper, T. J. Foreman, *Jama* **1989**, 262, 2125.
[84] M. Ponec, A. El Ghalbzouri, R. Dijkman, J. Kempenaar, G. van der Pluijm, P. Koolwijk, *Angiogenesis* **2004**, 7, 295.
[85] L. J. Meyer, R. Stern, *Journal of Investigative Dermatology* **1994**, 102, 385.
[86] C. Tonello, B. Zavan, R. Cortivo, P. Brun, S. Panfilo, G. Abatangelo, *Biomaterials* **2003**, 24, 1205.
[87] M. T. Cerqueira, L. P. da Silva, T. C. Santos, R. r. P. Pirraco, V. M. Correlo, R. L. Reis, A. P. Marques, *ACS applied materials & interfaces* **2014**, 6, 19668.
[88] C. Tonello, V. Vindigni, B. Zavan, S. Abatangelo, G. Abatangelo, P. Brun, R. Cortivo, *The FASEB journal* **2005**, 19, 1546.
[89] S. Bencherif, O. Gsib, C. Egles, *J. Mol. Biol. Biotech* **2017**, 2, 1.
[90] F. M. Shaikh, A. Callanan, E. G. Kavanagh, P. E. Burke, P. A. Grace, T. M. McGloughlin, *Cells Tissues Organs* **2008**, 188, 333.
[91] X. Chen, A. S. Aledia, C. M. Ghajar, C. K. Griffith, A. J. Putnam, C. C. Hughes, S. C. George, *Tissue Eng Part A* **2009**, 15, 1363.
[92] R. K. Chan, D. O. Zamora, N. L. Wrice, D. G. Baer, E. M. Renz, R. J. Christy, S. Natesan, *Stem Cells Int* **2012**, 2012, 841203.
[93] X. Liu, S. Michael, K. Bharti, M. Ferrer, M. J. Song, *Biofabrication* **2020**.
[94] A. Nishiguchi, H. Yoshida, M. Matsusaki, M. Akashi, *Adv Mater* **2011**, 23, 3506.
[95] M. Matsusaki, K. Fujimoto, Y. Shirakata, S. Hirakawa, K. Hashimoto, M. Akashi, *J Biomed Mater Res A* **2015**, 103, 3386.
[96] J. Bourland, J. Fradette, F. A. Auger, *Scientific reports* **2018**, 8, 1.
[97] H. Miyazaki, Y. Tsunoi, T. Akagi, S. Sato, M. Akashi, D. Saitoh, *Scientific reports* **2019**, 9, 1.
[98] J. S. Schechner, S. K. Crane, F. Wang, A. M. Szeglin, G. Tellides, M. I. Lorber, A. L. M. Bothwell, J. S. Pober, *The FASEB Journal* **2003**, 17, 2250.
[99] P. S. Sahota, J. L. Burn, M. Heaton, E. Freedlander, S. K. Suvarna, N. J. Brown, S. Mac Neil, *Wound Repair and Regeneration* **2003**, 11, 275.
[100] B. R. Shepherd, D. R. Enis, F. Wang, Y. Suarez, J. S. Pober, J. S. Schechner, *Faseb j* **2006**, 20, 1739.
[101] D. B. Kolesky, K. A. Homan, M. A. Skylar-Scott, J. A. Lewis, *Proceedings of the national academy of sciences* **2016**, 113, 3179.

[102] N. Mori, Y. Morimoto, S. Takeuchi, *Biomaterials* **2017**, 116, 48.
[103] H. E. Abaci, Z. Guo, A. Coffman, B. Gillette, W. H. Lee, S. K. Sia, A. M. Christiano, *Adv Healthc Mater* **2016**, 5, 1800.
[104] S. Kim, H. Lee, M. Chung, N. L. Jeon, *Lab on a Chip* **2013**, 13, 1489.
[105] M. J. Helmedag, S. Weinandy, Y. Marquardt, J. M. Baron, N. Pallua, C. V. Suschek, S. Jockenhoevel, *Tissue Engineering Part A* **2015**, 21, 343.
[106] N. Jusoh, J. Ko, N. L. Jeon, *APL bioengineering* **2019**, 3, 036101.
[107] F. Groeber, L. Engelhardt, J. Lange, S. Kurdyn, F. F. Schmid, C. Rucker, S. Mielke, H. Walles, J. Hansmann, *ALTEX - Alternatives to animal experimentation* **2016**, 33, 415.
[108] A.-E. Matei, C.-W. Chen, L. Kiesewetter, A.-H. Györfi, Y.-N. Li, T. Trinh-Minh, X. Xu, C. T. Manh, T. van Kuppevelt, J. Hansmann, *Annals of the rheumatic diseases* **2019**, 78, 1686.
[109] T. Baltazar, J. Merola, C. Catarino, C. B. Xie, N. C. Kirkiles-Smith, V. Lee, S. Hotta, G. Dai, X. Xu, F. C. Ferreira, *Tissue Engineering Part A* **2020**, 26, 227.
[110] D. Marino, J. Luginbühl, S. Scola, M. Meuli, E. Reichmann, *Science translational medicine* **2014**, 6, 221ra14.
[111] F. Kreimendahl, Y. Marquardt, C. Apel, M. Bartneck, G. Zwadlo-Klarwasser, J. Hepp, S. Jockenhoevel, J. M. Baron, *Journal of Biomedical Materials Research Part A* **2019**, 107, 1340.
[112] B. Kwak, S. Jin, S. Kim, E. Kim, J. Chung, J. Sung, *Biotechnology and Bioengineering* **2020**.
[113] Z. Guo, C. A. Higgins, B. M. Gillette, M. Itoh, N. Umegaki, K. Gledhill, S. K. Sia, A. M. Christiano, *Stem cell research & therapy* **2013**, 4, S2.
[114] S. Girardeau-Hubert, C. Deneuville, H. Pageon, K. Abed, C. Tacheau, N. Cavusoglu, M. Donovan, D. Bernard, D. Asselineau, *Scientific reports* **2019**, 9, 1.
[115] I. Wagner, E.-M. Materne, S. Brincker, U. Süßbier, C. Frädrich, M. Busek, F. Sonntag, D. A. Sakharov, E. V. Trushkin, A. G. Tonevitsky, *Lab on a Chip* **2013**, 13, 3538.
[116] I. Maschmeyer, T. Hasenberg, A. Jaenicke, M. Lindner, A. K. Lorenz, J. Zech, L.-A. Garbe, F. Sonntag, P. Hayden, S. Ayehunie, *European journal of pharmaceutics and biopharmaceutics* **2015**, 95, 77.
[117] M. R. Pittelkow, *Nat Med* **2005**, 11, 17.
[118] J. E. Greb, A. M. Goldminz, J. T. Elder, M. G. Lebwohl, D. D. Gladman, J. J. Wu, N. N. Mehta, A. Y. Finlay, A. B. Gottlieb, *Nat Rev Dis Primers* **2016**, 2, 16082.
[119] M. A. Lowes, M. Suarez-Farinas, J. G. Krueger, *Annu Rev Immunol* **2014**, 32, 227.
[120] C. M. Pfaff, Y. Marquardt, K. Fietkau, J. M. Baron, B. Luscher, *Sci Rep* **2017**, 7, 15631.
[121] W.-Y. Ma, K. Jia, Y. Zhang, *Experimental and therapeutic medicine* **2016**, 11, 631.
[122] F. C. Eberle, J. Bruck, J. Holstein, K. Hirahara, K. Ghoreschi, *F1000Res* **2016**, 5, 770.
[123] M. A. Lowes, T. Kikuchi, J. Fuentes-Duculan, I. Cardinale, L. C. Zaba, A. S. Haider, E. P. Bowman, J. G. Krueger, *Journal of Investigative Dermatology* **2008**, 128, 1207.
[124] J.-M. Ramirez, N. C. Brembilla, O. Sorg, R. Chicheportiche, T. Matthes, J.-M. Dayer, J.-H. Saurat, E. Roosnek, C. Chizzolini, *European Journal of Immunology* **2010**, 40, 2450.
[125] A. L. Neimann, D. B. Shin, X. Wang, D. J. Margolis, A. B. Troxel, J. M. Gelfand, *Journal of the American Academy of Dermatology* **2006**, 55, 829.
[126] K. Abuabara, R. S. Azfar, D. B. Shin, A. L. Neimann, A. B. Troxel, J. M. Gelfand, *Br J Dermatol* **2010**, 163, 586.
[127] N. J. Korman, Y. Zhao, J. Pike, J. Roberts, *Clinical and Experimental Dermatology* **2016**, 41, 514.
[128] E. Desmet, A. Ramadhas, J. Lambert, M. Van Gele, *Experimental Biology and Medicine* **2017**, 242, 1158.
[129] B. Roy, M. Simard, I. Lorthois, A. Bélanger, M. Maheux, A. Duque-Fernandez, G. Rioux, P. Simard, M. Deslauriers, L.-C. Masson, A. Morin, R. Pouliot, in *Skin Tissue Models*, (Eds: A. P. Marques, R. P. Pirraco, M. T. Cerqueira, R. L. Reis), Academic Press, Boston 2018.
[130] H. Niehues, E. H. van den Bogaard, *Experimental Dermatology* **2018**, 27, 512.
[131] J. P. H. Smits, H. Niehues, G. Rikken, I. M. J. J. van Vlijmen-Willems, G. W. H. J. F. van de Zande, P. L. J. M. Zeeuwen, J. Schalkwijk, E. H. van den Bogaard, *Scientific Reports* **2017**, 7, 11838.
[132] C. M. Pfaff, Y. Marquardt, K. Czaja, B. Lüscher, J. M. Baron, *Journal of Investigative Dermatology* **2016**, 136, S55.

[133] Z. Feng, M. Yamato, T. Akutsu, T. Nakamura, T. Okano, M. Umezu, *Artificial organs* **2003**, 27, 84.
[134] A. A. Tandara, T. A. Mustoe, *Journal of Plastic, Reconstructive & Aesthetic Surgery* **2011**, 64, 108.
[135] K. Clarysse, C. M. Pfaff, Y. Marquardt, L. Huth, I. Kortekaas Krohn, D. Kluwig, B. Luscher, J. Gutermuth, J. Baron, *J Eur Acad Dermatol Venereol* **2019**, 33, 367.
[136] L. Schmitt, Y. Marquardt, R. Heise, V. von Felbert, P. M. Amann, L. Huth, T. Steiner, F. Hölzle, S. Huth, J. M. Baron, *Skin Pharmacology and Physiology* **2019**, 32, 265.
[137] Y. Marquardt, P. M. Amann, R. Heise, K. Czaja, T. Steiner, H. F. Merk, C. Skazik-Voogt, J. M. Baron, *Lasers in surgery and medicine* **2015**, 47, 257.
[138] V. Moulin, G. Castilloux, A. Jean, D. R. Garrel, F. A. Auger, L. Germain, *Burns : journal of the International Society for Burn Injuries* **1996**, 22, 359.
[139] M. A. Karsdal, S. H. Nielsen, D. J. Leeming, L. L. Langholm, M. J. Nielsen, T. Manon-Jensen, A. Siebuhr, N. S. Gudmann, S. Ronnow, J. M. Sand, S. J. Daniels, J. H. Mortensen, D. Schuppan, *Advanced drug delivery reviews* **2017**, 121, 43.
[140] B. A. DALE, K. A. RESING, J. D. LONSDALE-ECCLES, *Annals of the New York Academy of Sciences* **1985**, 455, 330.
[141] S. J. Brown, W. H. Irwin McLean, *Journal of Investigative Dermatology* **2012**, 132, 751.
[142] V. Pendaries, J. Malaisse, L. Pellerin, M. Le Lamer, R. Nachat, S. Kezic, A.-M. Schmitt, C. Paul, Y. Poumay, G. Serre, M. Simon, *Journal of Investigative Dermatology* **2014**, 134, 2938.
[143] K. Yoneda, T. Nakagawa, O. T. Lawrence, J. Huard, T. Demitsu, Y. Kubota, R. B. Presland, *Journal of Investigative Dermatology* **2012**, 132, 1206.
[144] A. M. Lin, C. J. Rubin, R. Khandpur, J. Y. Wang, M. Riblett, S. Yalavarthi, E. C. Villanueva, P. Shah, M. J. Kaplan, A. T. Bruce, *The Journal of Immunology* **2011**, 187, 490.
[145] P. Emtage, P. Vatta, M. Arterburn, M. W. Muller, E. Park, B. Boyle, S. Hazell, R. Polizotto, W. D. Funk, Y. T. Tang, *Genomics* **2006**, 88, 513.
[146] A. A. Lobito, S. R. Ramani, I. Tom, J. F. Bazan, E. Luis, W. J. Fairbrother, W. Ouyang, L. C. Gonzalez, *The Journal of biological chemistry* **2011**, 286, 18969.
[147] S. R. Edmondson, S. P. Thumiger, G. A. Werther, C. J. Wraight, *Endocrine reviews* **2003**, 24, 737.
[148] J. H. Lee, D. H. Cho, H. J. Park, *Int J Mol Sci* **2015**, 16, 29357.
[149] J. Rouwkema, A. Khademhosseini, *Trends in biotechnology* **2016**, 34, 733.
[150] R. Heidenreich, M. Röcken, K. Ghoreschi, *Drug news & perspectives* **2008**, 21, 97.
[151] F. Grinnell, *Trends in cell biology* **2003**, 13, 264.
[152] C. Lotz, F. F. Schmid, E. Oechsle, M. G. Monaghan, H. Walles, F. Groeber-Becker, *ACS applied materials & interfaces* **2017**, 9, 20417.
[153] K. A. Scott, E. J. Wood, E. H. Karran, *FEBS letters* **1998**, 441, 137.
[154] E. Gentleman, E. Nauman, K. Dee, G. Livesay, *Tissue engineering* **2004**, 10, 421.
[155] A. L. Bauer, T. L. Jackson, Y. Jiang, *PLoS Comput Biol* **2009**, 5, e1000445.
[156] S. M. Bauer, R. J. Bauer, Z.-J. Liu, H. Chen, L. Goldstein, O. C. Velazquez, *Journal of vascular surgery* **2005**, 41, 699.
[157] B. Russo, N. C. Brembilla, C. Chizzolini, *Frontiers in Immunology* **2020**, 11.
[158] C. Korn, H. G. Augustin, *Developmental cell* **2015**, 34, 5.
[159] H. Bae, A. S. Puranik, R. Gauvin, F. Edalat, B. Carrillo-Conde, N. A. Peppas, A. Khademhosseini, *Science translational medicine* **2012**, 4, 160ps23.
[160] D. A. Chistiakov, A. N. Orekhov, Y. V. Bobryshev, *Acta physiologica* **2017**, 219, 382.
[161] G. Sriram, M. Alberti, Y. Dancik, B. Wu, R. Wu, Z. Feng, S. Ramasamy, P. L. Bigliardi, M. Bigliardi-Qi, Z. Wang, *Materials Today* **2018**, 21, 326.
[162] Q. Ramadan, F. C. W. Ting, *Lab on a Chip* **2016**, 16, 1899.
[163] B. Zohar, Y. Blinder, D. J. Mooney, S. Levenberg, *ACS Biomaterials Science & Engineering* **2018**, 4, 1265.
[164] N. Mori, Y. Morimoto, S. Takeuchi, *Biofabrication* **2018**, 11, 011001.
[165] M. Wufuer, G. Lee, W. Hur, B. Jeon, B. J. Kim, T. H. Choi, S. Lee, *Scientific reports* **2016**, 6, 37471.

[166] T. Akagi, M. Nagura, A. Hiura, H. Kojima, M. Akashi, *Tissue Engineering Part A* **2017**, 23, 481.
[167] H. G. Weller, G. Tabor, H. Jasak, C. Fureby, *Computers in physics* **1998**, 12, 620.
[168] S. S. Deshpande, L. Anumolu, M. F. Trujillo, *Computational science & discovery* **2012**, 5, 014016.
[169] E. Berberović, N. P. van Hinsberg, S. Jakirlić, I. V. Roisman, C. Tropea, *Physical Review E* **2009**, 79, 036306.
[170] Z. Zheng, S. Shin, H. A. Stone, *Journal of Fluid Mechanics* **2015**, 778, 669.
[171] E. Zudaire, L. Gambardella, C. Kurcz, S. Vermeren, *PloS one* **2011**, 6, e27385.
[172] J. Schindelin, I. Arganda-Carreras, E. Frise, V. Kaynig, M. Longair, T. Pietzsch, S. Preibisch, C. Rueden, S. Saalfeld, B. Schmid, *Nature methods* **2012**, 9, 676.
[173] E. Eden, R. Navon, I. Steinfeld, D. Lipson, Z. Yakhini, *BMC bioinformatics* **2009**, 10, 1.
[174] P. Shannon, A. Markiel, O. Ozier, N. S. Baliga, J. T. Wang, D. Ramage, N. Amin, B. Schwikowski, T. Ideker, *Genome research* **2003**, 13, 2498.
[175] G. D. Bader, C. W. Hogue, *BMC bioinformatics* **2003**, 4, 1.
[176] S. Singh, Y. Marquardt, R. Rimal, A. Nishiguchi, S. Huth, M. Akashi, M. Moeller, J. M. Baron, *ACS Applied Bio Materials* **2020**, 3, 6639.
[177] Y. Liu, H. Luo, X. Wang, A. Takemura, Y. R. Fang, Y. Jin, F. Suwa, *BioMed research international* **2013**, 2013.
[178] R. H. Adams, K. Alitalo, *Nature reviews Molecular cell biology* **2007**, 8, 464.
[179] P. Lu, K. Takai, V. M. Weaver, Z. Werb, *Cold Spring Harbor perspectives in biology* **2011**, 3, a005058.
[180] U. K. Saarialho-Kere, A. P. Pentland, H. Birkedal-Hansen, W. C. Parks, H. G. Welgus, *The Journal of clinical investigation* **1994**, 94, 79.
[181] J. E. Rundhaug, *Journal of cellular and molecular medicine* **2005**, 9, 267.
[182] G. Sawicki, Y. Marcoux, K. Sarkhosh, E. E. Tredget, A. Ghahary, *Molecular and cellular biochemistry* **2005**, 269, 209.
[183] B. Anand-Apte, M. S. Pepper, E. Voest, R. Montesano, B. Olsen, G. Murphy, S. S. Apte, B. Zetter, *Investigative ophthalmology & visual science* **1997**, 38, 817.
[184] A. Koskela, K. Engström, M. Hakelius, D. Nowinski, M. Ivarsson, *Wound repair and regeneration* **2010**, 18, 452.
[185] J. H. Qi, Q. Ebrahem, N. Moore, G. Murphy, L. Claesson-Welsh, M. Bond, A. Baker, B. Anand-Apte, *Nat Med* **2003**, 9, 407.
[186] M. Vaalamo, T. Leivo, U. Saarialho-Kere, *Human pathology* **1999**, 30, 795.
[187] C. A. Fernández, M. A. Moses, *Biochemical and biophysical research communications* **2006**, 345, 523.
[188] T. Sun, D. Norton, J. W. Haycock, A. J. Ryan, S. MacNeil, *Tissue Engineering* **2005**, 11, 1824.
[189] B. Kalyanaraman, D. M. Supp, S. T. Boyce, *Tissue Engineering Part A* **2008**, 14, 583.
[190] I. Koskivirta, O. Rahkonen, M. Mäyränpää, S. Pakkanen, M. Husheem, A. Sainio, H. Hakovirta, J. Laine, E. Jokinen, E. Vuorio, *Histochemistry and cell biology* **2006**, 126, 335.
[191] J. A. Forsythe, B.-H. Jiang, N. V. Iyer, F. Agani, S. W. Leung, R. D. Koos, G. L. Semenza, *Molecular and cellular biology* **1996**, 16, 4604.
[192] M. J. Barron, J. Goldman, C.-J. Tsai, S. W. Donahue, *International journal of biomaterials* **2012**, 2012.
[193] B. Ataç, I. Wagner, R. Horland, R. Lauster, U. Marx, A. G. Tonevitsky, R. P. Azar, G. Lindner, *Lab on a chip* **2013**, 13, 3555.
[194] A. Sandilands, C. Sutherland, A. D. Irvine, W. I. McLean, *Journal of cell science* **2009**, 122, 1285.
[195] W. McLean, *British Journal of Dermatology* **2016**, 175, 4.
[196] A. Neve, F. P. Cantatore, N. Maruotti, A. Corrado, D. Ribatti, *BioMed research international* **2014**, 2014.
[197] R. L. Steward, C.-M. Cheng, D. Y. Jonathan, R. M. Bellin, P. R. LeDuc, *Scientific reports* **2011**, 1, 147.
[198] G. Hagedorn, A. Blank, R. Mai, B. Weiland, A. Spassov, G. Lauer, *J Physiol Pharmacol* **2009**, 60, 25.

[199] E. Duperret, T. W. Ridky, *Cell cycle* **2013**, 12, 3272.
[200] T. Agarwal, G. H. Narayana, I. Banerjee, *Cytoskeleton* **2019**, 76, 209.
[201] K. A. Homan, N. Gupta, K. T. Kroll, D. B. Kolesky, M. Skylar-Scott, T. Miyoshi, D. Mau, M. T. Valerius, T. Ferrante, J. V. Bonventre, J. A. Lewis, R. Morizane, *Nature Methods* **2019**, 16, 255.
[202] C. P. Ng, C.-L. E. Helm, M. A. Swartz, *Microvascular research* **2004**, 68, 258.
[203] L. Schmitt, S. Huth, P. Amann, Y. Marquardt, R. Heise, K. Fietkau, L. Huth, T. Steiner, F. Hölzle, J. Baron, *Lasers in medical science* **2018**, 33, 765.
[204] M. Piipponen, D. Li, N. X. Landén, *International Journal of Molecular Sciences* **2020**, 21, 8790.
[205] E. Sutterby, P. Thurgood, S. Baratchi, K. Khoshmanesh, E. Pirogova, *Small* **2020**, 16, 2002515.
[206] J. Ponmozhi, S. Dhinakaran, Z. Varga-Medveczky, K. Fónagy, L. A. Bors, K. Iván, F. Erdő, *Micromachines* **2021**, 12, 294.
[207] A. Amirsadeghi, A. Jafari, L. J. Eggermont, S.-S. Hashemi, S. A. Bencherif, M. Khorram, *Biomaterials Science* **2020**, 8, 4073.
[208] S. Tavakoli, A. S. Klar, *Applied Sciences* **2021**, 11, 1493.
[209] F. Bray, J. Ferlay, I. Soerjomataram, R. L. Siegel, L. A. Torre, A. Jemal, *CA: a cancer journal for clinicians* **2018**, 68, 394.
[210] C. M. Perou, T. Sorlie, M. B. Eisen, M. van de Rijn, S. S. Jeffrey, C. A. Rees, J. R. Pollack, D. T. Ross, H. Johnsen, L. A. Akslen, O. Fluge, A. Pergamenschikov, C. Williams, S. X. Zhu, P. E. Lonning, A. L. Borresen-Dale, P. O. Brown, D. Botstein, *Nature* **2000**, 406, 747.
[211] V. Patanaphan, O. M. Salazar, R. Risco, *Southern medical journal* **1988**, 81, 1109.
[212] D. X. Nguyen, P. D. Bos, J. Massague, *Nature reviews. Cancer* **2009**, 9, 274.
[213] J. Massague, A. C. Obenauf, *Nature* **2016**, 529, 298.
[214] Z. S. Templeton, W. R. Lie, W. Wang, Y. Rosenberg-Hasson, R. V. Alluri, J. S. Tamaresis, M. H. Bachmann, K. Lee, W. J. Maloney, C. H. Contag, B. L. King, *Neoplasia* **2015**, 17, 849.
[215] R. E. Coleman, E. Rathbone, J. E. Brown, *Nature reviews. Rheumatology* **2013**, 9, 365.
[216] F. Salamanna, D. Contartese, M. Maglio, M. Fini, *Oncotarget* **2016**, 7, 44803.
[217] E. P. Carter, J. A. Gopsill, J. J. Gomm, J. L. Jones, R. P. Grose, *Breast cancer research : BCR* **2017**, 19, 50.
[218] S. J. Bidarra, P. Oliveira, S. Rocha, D. P. Saraiva, C. Oliveira, C. C. Barrias, *Sci Rep* **2016**, 6, 27072.
[219] H. H. Song, K. M. Park, S. Gerecht, *Advanced drug delivery reviews* **2014**, 79-80, 19.
[220] L. Gu, D. J. Mooney, *Nature reviews. Cancer* **2016**, 16, 56.
[221] A. J. Walsh, R. S. Cook, M. E. Sanders, C. L. Arteaga, M. C. Skala, *Sci Rep* **2016**, 6, 18889.
[222] Y. S. DeRose, K. M. Gligorich, G. Wang, A. Georgelas, P. Bowman, S. J. Courdy, A. L. Welm, B. E. Welm, *Current protocols in pharmacology* **2013**, Chapter 14, Unit14 23.
[223] S. Bersini, J. S. Jeon, G. Dubini, C. Arrigoni, S. Chung, J. L. Charest, M. Moretti, R. D. Kamm, *Biomaterials* **2014**, 35, 2454.
[224] J. S. Jeon, S. Bersini, M. Gilardi, G. Dubini, J. L. Charest, M. Moretti, R. D. Kamm, *Proceedings of the National Academy of Sciences* **2015**, 112, 214.
[225] A. M. Mastro, E. A. Vogler, *Cancer research* **2009**, 69, 4097.
[226] R. J. Thomas, T. A. Guise, J. J. Yin, J. Elliott, N. J. Horwood, T. J. Martin, M. T. Gillespie, *Endocrinology* **1999**, 140, 4451.
[227] C.-S. Devignes, Y. Aslan, A. Brenot, A. Devillers, K. Schepers, S. Fabre, J. Chou, A.-J. Casbon, Z. Werb, S. Provot, *Proceedings of the National Academy of Sciences* **2018**, 115, E992.
[228] A. E. Chiou, C. Liu, I. Moreno-Jiménez, T. Tang, W. Wagermaier, M. N. Dean, C. Fischbach, P. Fratzl, *Science Advances* **2021**, 7, eabf2283.
[229] Y. Liu, X. Cao, *Cancer cell* **2016**, 30, 668.
[230] G. Nagel, R. Peter, E. Klotz, W. Brozek, H. Concin, *Bone reports* **2017**, 7, 83.
[231] M. van der Klift, C. E. de Laet, J. W. W. Coebergh, A. Hofman, H. A. Pols, *Bone* **2003**, 32, 211.
[232] C. L. Bager, F. Bay, C. Christiansen, M. Karsdal, *Bone* **2019**, 127, 75.
[233] B. Kinikoglu, *Alternatives to Laboratory Animals* **2017**, 45, 309.

[234] A. Nishiguchi, M. Matsusaki, M. R. Kano, H. Nishihara, D. Okano, Y. Asano, H. Shimoda, S. Kishimoto, S. Iwai, M. Akashi, *Biomaterials* **2018**, 179, 144.
[235] Y. Zhou, B. Zhou, L. Pache, M. Chang, A. H. Khodabakhshi, O. Tanaseichuk, C. Benner, S. K. Chanda, *Nature communications* **2019**, 10, 1.
[236] J. Goedhart, M. S. Luijsterburg, *Scientific reports* **2020**, 10, 1.
[237] D. Szklarczyk, A. Franceschini, S. Wyder, K. Forslund, D. Heller, J. Huerta-Cepas, M. Simonovic, A. Roth, A. Santos, K. P. Tsafou, *Nucleic acids research* **2015**, 43, D447.
[238] C.-H. Chin, S.-H. Chen, H.-H. Wu, C.-W. Ho, M.-T. Ko, C.-Y. Lin, *BMC systems biology* **2014**, 8, 1.
[239] Z. Tang, B. Kang, C. Li, T. Chen, Z. Zhang, *Nucleic acids research* **2019**, 47, W556.
[240] M. Franchi, Z. Piperigkou, E. Riti, V. Masola, M. Onisto, N. K. Karamanos, *Matrix Biology Plus* **2020**, 6, 100026.
[241] M. Franchi, Z. Piperigkou, K.-A. Karamanos, L. Franchi, V. Masola, *Cells* **2020**, 9, 2031.
[242] P. A. Kenny, G. Y. Lee, C. A. Myers, R. M. Neve, J. R. Semeiks, P. T. Spellman, K. Lorenz, E. H. Lee, M. H. Barcellos-Hoff, O. W. Petersen, *Molecular oncology* **2007**, 1, 84.
[243] J. J. Campbell, A. Husmann, R. D. Hume, C. J. Watson, R. E. Cameron, *Biomaterials* **2017**, 114, 34.
[244] A. Z. Fernandis, A. Prasad, H. Band, R. Klösel, R. K. Ganju, *Oncogene* **2004**, 23, 157.
[245] J. D. Holland, M. Kochetkova, C. Akekawatchai, M. Dottore, A. Lopez, S. R. McColl, *Cancer research* **2006**, 66, 4117.
[246] B. Linderholm, H. Hellborg, U. Johansson, G. Elmberger, L. Skoog, J. Lehtiö, R. Lewensohn, *Annals of oncology* **2009**, 20, 1639.
[247] J. A. Foekens, H. A. Peters, N. Grebenchtchikov, M. P. Look, M. E. Meijer-van Gelder, A. Geurts-Moespot, T. H. van der Kwast, C. F. Sweep, J. G. Klijn, *Cancer research* **2001**, 61, 5407.
[248] K. Hu, B. R. Olsen, *The Journal of clinical investigation* **2016**, 126, 509.
[249] P. Dutta, M. Sarkissyan, K. Paico, Y. Wu, J. V. Vadgama, *Breast cancer research and treatment* **2018**, 170, 477.
[250] T. Ueno, M. Toi, H. Saji, M. Muta, H. Bando, K. Kuroi, M. Koike, H. Inadera, K. Matsushima, *Clinical cancer research* **2000**, 6, 3282.
[251] B. S. Mulholland, M. R. Forwood, N. A. Morrison, *Current osteoporosis reports* **2019**, 17, 538.
[252] K. Tawara, J. T. Oxford, C. L. Jorcyk, *Cancer management and research* **2011**, 3, 177.
[253] G. Gopinathan, C. Milagre, O. M. Pearce, L. E. Reynolds, K. Hodivala-Dilke, D. A. Leinster, H. Zhong, R. E. Hollingsworth, R. Thompson, J. R. Whiteford, *Cancer research* **2015**, 75, 3098.
[254] K. Hida, N. Maishi, D. A. Annan, Y. Hida, *International journal of molecular sciences* **2018**, 19, 1272.
[255] T. Peeters, F. Cailotto, R. Lories, *Osteoarthritis and Cartilage* **2016**, 24, S141.
[256] J. Luo, P. Sun, S. Siwko, M. Liu, J. Xiao, *Bone research* **2019**, 7, 1.
[257] E. Sjöberg, M. Augsten, J. Bergh, K. Jirström, A. Östman, *British journal of cancer* **2016**, 114, 1117.
[258] S. Takiguchi, N. Korenaga, K. Inoue, E. Sugi, Y. Kataoka, K. Matsusue, K. Futagami, Y.-J. Li, T. Kukita, N. Teramoto, *International journal of oncology* **2014**, 44, 1316.
[259] W. Chen, A. D. Hoffmann, H. Liu, X. Liu, *NPJ precision oncology* **2018**, 2, 1.
[260] C. Engblom, C. Pfirschke, R. Zilionis, J. D. S. Martins, S. A. Bos, G. Courties, S. Rickelt, N. Severe, N. Baryawno, J. Faget, *Science* **2017**, 358.
[261] Q. Ji, L. Zhou, H. Sui, L. Yang, X. Wu, Q. Song, R. Jia, R. Li, J. Sun, Z. Wang, *Nature communications* **2020**, 11, 1.
[262] A. B. Shupp, A. D. Kolb, D. Mukhopadhyay, K. M. Bussard, *Cancers* **2018**, 10, 182.
[263] R. R. Mercer, C. Miyasaka, A. M. Mastro, *Clinical & experimental metastasis* **2004**, 21, 427.
[264] M. Kinder, E. Chislock, K. M. Bussard, L. Shuman, A. M. Mastro, *Experimental cell research* **2008**, 314, 173.
[265] C. Voutouri, N. D. Kirkpatrick, E. Chung, F. Mpekris, J. W. Baish, L. L. Munn, D. Fukumura, T. Stylianopoulos, R. K. Jain, *Proceedings of the National Academy of Sciences* **2019**, 116, 2662.

[266] E. A. Kuczynski, P. B. Vermeulen, F. Pezzella, R. S. Kerbel, A. R. Reynolds, *Nature reviews Clinical oncology* **2019**, 16, 469.
[267] T. P. Padera, B. R. Stoll, J. B. Tooredman, D. Capen, E. di Tomaso, R. K. Jain, *Nature* **2004**, 427, 695.
[268] V. L. Silvestri, E. Henriet, R. M. Linville, A. D. Wong, P. C. Searson, A. J. Ewald, *Cancer Research* **2020**, 80, 4288.
[269] D.-H. T. Nguyen, E. Lee, S. Alimperti, R. J. Norgard, A. Wong, J. J.-K. Lee, J. Eyckmans, B. Z. Stanger, C. S. Chen, *Science advances* **2019**, 5, eaav6789.
[270] D. Zagzag, R. Amirnovin, M. A. Greco, H. Yee, J. Holash, S. J. Wiegand, S. Zabski, G. D. Yancopoulos, M. Grumet, *Laboratory investigation* **2000**, 80, 837.
[271] E. Pick, Y. Kluger, J. M. Giltnane, C. Moeder, R. L. Camp, D. L. Rimm, H. M. Kluger, *Cancer research* **2007**, 67, 2932.
[272] Q. Cheng, J. T. Chang, J. Geradts, L. M. Neckers, T. Haystead, N. L. Spector, H. K. Lyerly, *Breast cancer research* **2012**, 14, 1.
[273] K. Hang, C. Ye, E. Chen, W. Zhang, D. Xue, Z. Pan, *Cell Stress and Chaperones* **2018**, 23, 1153.
[274] J. T. Price, J. M. Quinn, N. A. Sims, J. Vieusseux, K. Waldeck, S. E. Docherty, D. Myers, A. Nakamura, M. C. Waltham, M. T. Gillespie, *Cancer research* **2005**, 65, 4929.
[275] A. Yano, S. Tsutsumi, S. Soga, M.-J. Lee, J. Trepel, H. Osada, L. Neckers, *Proceedings of the National Academy of Sciences* **2008**, 105, 15541.
[276] M. Li, Y. Guo, Y.-M. Feng, N. Zhang, *Frontiers in genetics* **2019**, 10, 180.
[277] H. S. Park, M. H. Jang, E. J. Kim, H. J. Kim, H. J. Lee, Y. J. Kim, J. H. Kim, E. Kang, S.-W. Kim, I. A. Kim, *Modern pathology* **2014**, 27, 1212.
[278] D. Liu, J. He, Z. Yuan, S. Wang, R. Peng, Y. Shi, X. Teng, T. Qin, *Medical oncology* **2012**, 29, 401.
[279] K. C. Day, G. L. Hiles, M. Kozminsky, S. J. Dawsey, A. Paul, L. J. Broses, R. Shah, L. P. Kunja, C. Hall, N. Palanisamy, *Cancer research* **2017**, 77, 74.
[280] J. Zhu, X. Jia, G. Xiao, Y. Kang, N. C. Partridge, L. Qin, *Journal of Biological Chemistry* **2007**, 282, 26656.
[281] J. Niu, X.-M. Li, X. Wang, C. Liang, Y.-D. Zhang, H.-Y. Li, F.-Y. Liu, H. Sun, S.-Q. Xie, D. Fang, *Cancer cell international* **2019**, 19, 1.
[282] K. Mariz, J.-B. Ingolf, H. Daniel, N. J. Teresa, S. Erich-Franz, *Clinical & experimental metastasis* **2015**, 32, 857.
[283] X. Zhuang, H. Zhang, X. Li, X. Li, M. Cong, F. Peng, J. Yu, X. Zhang, Q. Yang, G. Hu, *Nature cell biology* **2017**, 19, 1274.
[284] K. L. Clines, G. A. Clines, *Translational oncology* **2018**, 11, 873.
[285] K.-T. Guo, P. Fu, K. Juerchott, H. Motaln, J. Selbig, T. Lah, J.-C. Tonn, C. Schichor, *Journal of cancer research and clinical oncology* **2014**, 140, 1261.
[286] M. Ampuja, R. Jokimäki, K. Juuti-Uusitalo, A. Rodriguez-Martinez, E.-L. Alarmo, A. Kallioniemi, *BMC cancer* **2013**, 13, 1.
[287] D.-H. Bach, H. J. Park, S. K. Lee, *Molecular Therapy-Oncolytics* **2018**, 8, 1.
[288] B. L. Eckhardt, Y. Cao, A. D. Redfern, L. H. Chi, A. D. Burrows, S. Roslan, E. K. Sloan, B. S. Parker, S. Loi, N. T. Ueno, *Cancer research* **2020**, 80, 1304.
[289] M. Ampuja, E. Alarmo, P. Owens, R. Havunen, A. Gorska, H. Moses, A. Kallioniemi, *Cancer letters* **2016**, 375, 238.
[290] A. Ignatius, P. Schoengraf, L. Kreja, A. Liedert, S. Recknagel, S. Kandert, R. E. Brenner, M. Schneider, J. D. Lambris, M. Huber-Lang, *Journal of cellular biochemistry* **2011**, 112, 2594.
[291] M. G. Kazanietz, M. Durando, M. Cooke, *Frontiers in endocrinology* **2019**, 10, 471.
[292] E. De Vuyst, M. Salmon, C. Evrard, C. Lambert de Rouvroit, Y. Poumay, *Frontiers in Medicine* **2017**, 4, 119.
[293] T. McPherson, *Indian journal of dermatology* **2016**, 61, 649.
[294] E. D'Auria, G. Banderali, S. Barberi, L. Gualandri, B. Pietra, E. Riva, A. Cerri, *Asian Pac J Allergy Immunol* **2016**, 34, 98.
[295] P. J. Barnes, *Br J Pharmacol* **2006**, 148, 245.
[296] W. Ericson-Neilsen, A. D. Kaye, *Ochsner J* **2014**, 14, 203.

[297] M. Greaves, *Postgraduate Medical Journal* **1976**, 52, 631.
[298] S. Yang, L. Zhang, *Current Vascular Pharmacology* **2004**, 2, 1.
[299] D. M. Poetker, D. D. Reh, *Otolaryngologic Clinics of North America* **2010**, 43, 753.
[300] U. R. Hengge, T. Ruzicka, R. A. Schwartz, M. J. Cork, *Journal of the American Academy of Dermatology* **2006**, 54, 1.
[301] A. Coondoo, M. Phiske, S. Verma, K. Lahiri, *Indian Dermatology Online Journal* **2014**, 5, 416.

Acknowledgments

Firstly, I would like to acknowledge the entire scientific community of **DWI Liebniz Institute for Interactive Materials** for funding and encouraging projects pertaining to alternate to animal research. The institute supports many *in-vitro* based projects and is taking a step forward in reducing animal-based conventional methods. I want to express my sincere gratitude to **Prof. Dr. Martin Möller** for providing an excellent research topic in the field of tissue engineering. His out of the box approach in dealing with scientific questions has always been a motivating factor to not only me but the entire DWI PhD community.

The projects I worked on was led by **Dr. Smriti Singh** who was a constant support in the development and conclusion of several ideas. Dr Singh was more than just a supervisor. She dealt not only in generating and listening to potential project ideas but also was there in personal level, encouraging mental health. I am sincerely grateful for her as she devoted 100% of her time in problem-solving and uplifiting me and others, thereby motivating us to manifest more scientific ideas. Thank you in believing in the project and the value it would bring with it.

My sincere thank you to the researchers in University Hospital Aachen, Dermatology group**. Dr. Jens Baron** has immense knowledge in skin physiology and I definitely was blessed to have him as a part of several projects. I have a great opportunity to work with **Mrs. Yvonne Marquardt** who constantly assisted me in experiments. She has an in-depth knowledge in the trouble-shooting issues generated during the fabrication of tissue models and cell-based assays. I am extremely lucky that she was there specially in my initial days as a PhD student and I could learn many techniques from her. I would like to also thank Dr. Sebastian Huth who supported me in times of experimental need.

I thank the research training group (RTG) 2375 Tumor-Targeted Drug Delivery coordinated by Prof. Dr. Twan Lammers and Prof. Dr. Fabian Kiessling for giving me the opportunity to be an associated PhD student in the consortium. I learned a lot from the multidisciplinary projects led by diverse research groups. This helped me in developing a sound scientific interested in tumor drug delivery.

I would like to thank all the PhD students in the group for constantly helping. I would speically thank Thorsten, Prachi, and Aisa in being very accomodating during my PhD. I would like to thank everyone from the cell lab. That was my second home. I thank Fred for keeping the cell lab super organised and small talks we had. I would like to thank Sitara for being an amazing colleague and friend, inviting me to her house and consoling me during bad times. During the writing phase of this thesis, I made a lot of friends at the Max Planck Institute for Medical Reasearch. I would like to thank them for constantly motivating me to complete the thesis and help me overcome my writer´s block. Harish, Amelie, and Manu- thank you all for being there emotionally. Manu, thank you for translating the abstract to Deutsch. I would never pull that off with my german skills.

I thank my friend Anshuman for all the time we spent and all the support when I first landed in Aachen. I still remember all the scientfic problems we talked about and how I got interested in tumor biology and drug delivery because of his enthusiasm to the subject.

A special thank to Omid who was my PhD supervisor during my master thesis. I learnt how to think out of the box from him and now try to imitate his confidence and analytical skills. A sincere thank you for believing in me when I was just an amateur in biological science and giving me the opportunity to be part of your publications. That has helped me immensely in pursuing my career further. I thank Prof. Dr. Laura De Laporte for giving me that initial opportunity to conduct Master´s thesis in her lab that spear-headed my research career.

I thank Thomas Nevolianis and Dr Dmitri Chigrin who help conduct the simulation experiments that helped in understanding the flow patterns. I would like to thank Dr. Suzana Djeljadini in helping with the printing of the 3D bioreactors. Some words for my Master´s students- Andrea, Tina and Karina who were very enthusiastic and achieved really good grades in their masters thesis. They were super motivated which in-turn motivated me. They helped me optimise many of the experiments and we had a wonderful time outside experiments and I thank you all for that.

Thank you to my fiancé, Prachi, for being there during the good and bad phases in my life. This thesis would not have been complete without your scientific, emotional, and mental support. I am lucky to have you for life. My love and gratitude to my family, my parents who kept my education as the priority and constantly motivating me. My sister, Riki for supporting me throughout the years and being there everytime I need her. Thommy, I thank you for always being kind and making me feel a part of the family and my nephew/niece Vidar/Sigrid for being cute and cuddly.

All in all, I would say that even if it was a long journey, I am glad to have found friends and mentors besides me continually believing in me.